

© 2008

Navin Venugopal

ALL RIGHTS RESERVED

AGGREGATE BREAKDOWN OF NANOPARTICULATE TITANIA

by

NAVIN VENUGOPAL

A dissertation submitted to the

Graduate School – New Brunswick

Rutgers, The State University of New Jersey

in partial fulfillment of the requirements

for the degree of

Doctor of Philosophy

Graduate Program in Ceramic and Materials Engineering

written under the direction of

Professor Richard A. Haber

and approved by

New Brunswick, New Jersey

January, 2008

ABSTRACT OF DISSERTATION

Aggregate Breakdown of Nanoparticulate Titania

By Navin Venugopal

Dissertation Director: Dr. Richard A. Haber

Six nanosized titanium dioxide powders synthesized from a sulfate process were investigated. The targeted end-use of this powder was for a de-NO_x catalyst honeycomb monolith. Alteration of synthesis parameters had resulted principally in differences in soluble ion level and specific surface area of the powders. The goal of this investigation was to understand the role of synthesis parameters in the aggregation behavior of these powders. Investigation via scanning electron microscopy of the powders revealed three different aggregation iterations at specific length scales.

Secondary and higher order aggregate strength was investigated via oscillatory stress rheometry as a means of simulating shear conditions encountered during extrusion. G' and G'' were measured as a function of the applied oscillatory stress. Oscillatory rheometry indicated a strong variation as a function of the sulfate level of the particles in the viscoelastic yield strengths. Powder yield stresses ranged from 3.0 Pa to 24.0 Pa of oscillatory stress. Compaction curves to 750 MPa found strong similarities in extrapolated yield point of stage I and II compaction for each of the powders (at approximately 500 MPa) suggesting that the variation in sulfate was greatest above the primary aggregate level. Scanning electron microscopy of samples at different states of shear in oscillatory rheometry confirmed the variation in the linear elastic region and the viscous flow regime.

A technique of this investigation was to approach aggregation via a novel perspective: aggregates are distinguished as being loose open structures that are highly disordered and stochastic in nature. The methodology used was to investigate the shear stresses required to rupture the various aggregation stages encountered and investigate the attempt to realign the now free-flowing constituents comprising the aggregate into a denser configuration. Mercury porosimetry was utilized to measure the pore size of the compact resulting from compaction via dry pressing and tape casting secondary scale aggregates. Mercury porosimetry of tapes cast at 0.85 and 9.09 cm/sec exhibited pore sizes ranging from 200-500 nm suggesting packing of intact micron-sized primary aggregates. Porosimetry further showed that this peak was absent in pressed pellets corroborating arguments of ruptured primary aggregates during compaction to 750 MPa.

Acknowledgements

I would like to begin by thanking my thesis advisor Dr. Richard A. Haber. You've always been there to give me a second chance to prove myself time and time again. More than that, you've helped me grow as a student, a researcher and as a person in general and for that I am greatly indebted to you.

Thanks to my thesis committee, Dr. Manish Chhowalla, Dr. Dale Niesz and Dr. Robert E. Johnson for their guidance in crafting this work.

Thank you to Steve Augustine, the Millennium Chemicals Corporation and the Center for Ceramic and Composite Materials Research for funding this research and having faith in its outcome.

Many thanks to the professors of this department that have encouraged me to pursue a doctorate throughout my time with the university, specifically Dr. Danforth, Dr. Matthewson, Dr. Riman, Dr. Lehman, Dr. Greenhut, Dr. Wenzel, Dr. Siegel and Dr. Xu.

I'd like to thank the staff of this department, particularly John, Phyllis, Betty, and Claudia for making life smoother on the rougher days. Thanks especially to Laura and Jessica for their (many) hours of perpetual counsel and support.

Thank you to Shawn N., Mike B, and Ryan M. for being my mentors, scolders and supporters throughout good and bad times of graduate school. I cannot thank you enough for reminding me to look at the big picture and for your leadership in troubled times.

I would like to thank my officemates past and present, Cari A., Nestor G. and Andrew P., who've had to put up with my eccentricities, cackling laughter and loud voice

over the years. Thanks particularly to Ray B. and Volkan D. for showing me what hard work and dedication was by example.

Many thanks to my research assistants over these past few years, Qi Y., Charles T., Mike O., Shu Min G. and Nick K. who have put up with my bossiness and even louder voice yet shone through with their natural talents and helped substantiate a lot of the body of work ahead. Special thanks particularly to Dan M. whose enthusiasm for his senior project invigorated me to see the value in my own work.

I would like to thank the Rutgers MSE subgroup ‘Happy Valley’ and its members, past present and future and to all the good times we’ve shared, particularly Cecilia P., Fred M., Chris Z., Laura R., Steve M., Slava D., Anil K., Mihaela J., Qiqen F., Scot D., Chuck M., Brant J., Andrea G., Alfonso M., Timmy T., Andy M., Rich D., Earl A., Joe P., Ashwin R., Brian M., Kyle, Billy, Adam P., Jeff S., Paul S. and Yao Y.. I’d also like to thank Jennifer C. for her assistance and training on the mercury porosimeter.

Many thanks to my friends Te L., Jaime G.-L., Steve B., Dan M., Paul S., Heather H.-S., Devon M., Angie M.-M., Kevyn S., Rafael P., Liz O., Leo T., Omir O. and Roxana S., who have seen my struggles and triumphs firsthand and who never stopped believing in me. Special thanks are owed to Mukund R. for always being a friend whenever he was needed without exception and for teaching me to believe in myself and stand up for what I thought was right. Further special thanks to Shanti S. for being a caring and wonderful person and for being my own source of peace. Thanks to the entire Sambandan family too.

Many thanks to Priya, Magesh, Divya, Ganga athai, Raman athimber, Mani mama, Raji mami, Mahesh, Jaya, Ananya, Aju, Janaki, Anita, Vivek, Spriha, Lata,

Sekhar, Samyu, Siddhart, Ramu, Jayanthi, Aditya, Aruni, Santanam, Padma, Srivats, Bharat, Surekha, Lax, Rohan, Priya R., Kishore, Shreya, Suresh, Anu and a myriad of other family members, both blood and extended, too numerous to mention by name who have all supported and encouraged me and watched me grow as a person.

I deeply want to thank my brother Rajesh and sister-in-law Marcella, who were my biggest supporters since I first mentioned the words “grad school” some 6 years ago and have been my sympathizers, scolders, counselors and substitute parents throughout.

Many, many, many thanks to my mother Janaki and father Venugopal, for incredible moral support, for intangibles, for guidance, and love. I know that what good I’ve ever done with my life has been all because of you.

I would like to give thanks to my paati (paternal grandmother), who passed away before I even went to grad school but lived a full and happy life seeing all but one of her grandchildren (guess who) get married or engaged and who always wanted a Ph.D. among her grandchildren.

Lastly, my heartfelt thanks to my nephews Ravi Riccardo Venugopal and Kiran Davide Venugopal. Both shining stars, hopes for the future, born during my time as a graduate student.

I could not have carried out this work without your help, assistance, guidance or support and for that, thank you all very much.

Table of Contents	Page
Abstract of the Dissertation.....	ii
Acknowledgements.....	iv
Table of Contents.....	vii
List of Tables.....	xiii
List of Figures.....	xiv
I. Introduction.....	1
II. Literature Review.....	3
II.1. Selective Catalytic Reduction.....	3
II.1.1. NO _x	3
II.1.2. History of Environmental Regulation.....	4
II.1.3. Current Technology Implementation.....	7
II.1.3.1. Selective Catalytic Reduction.....	7
II.1.3.2. NO _x Absorber Catalysts.....	9
II.2. Titanium Dioxide.....	10
II.2.1. Physical properties.....	11
II.2.2. Synthesis Techniques.....	13
II.2.3. Applications.....	17
II.3. Definitions.....	18
II.3.1. Nanosized Material.....	18
II.3.2. Colloid.....	18
II.3.3. Ultrafine/Fine.....	19
II.3.4. Aggregate.....	19

II.3.5. Primary Particle.....	20
II.3.6. Agglomerate.....	20
II.3.7. Floc.....	20
II.3.8. Coagulate.....	20
II.3.9. Aggregation stages.....	20
II.4. Cause of Aggregation.....	22
II.4.1. DLVO Theory.....	22
II.4.2. Exacerbation at the Nanometer Length Scale.....	25
II.5. Modeling of Aggregate Systems.....	26
II.5.1. Number of Spheres.....	26
II.5.2. Fractal Dimension.....	26
II.5.3. Average Agglomerate Number.....	29
II.6. Rheology.....	31
II.6.1. Basic principles.....	31
II.6.1.1. Flow Models.....	38
II.6.1.1.1. Newtonian	40
II.6.1.1.2. Casson	40
II.6.1.1.3. Power-law.....	41
II.6.1.1.4. Cross	42
II.6.1.1.5. Bingham.....	42
II.6.1.1.6. Herschel-Bulkley.....	42
II.6.1.2. Thixotropy.....	43
II.6.2. Viscoelasticity.....	44

II.6.3. Aggregate Network Model.....	48
II.6.3.1. Rheology of Suspensions of Spherical Particles.....	48
II.6.3.2. Impulse theory.....	50
II.6.3.3. Dual Moduli.....	51
II.6.3.4. Wu and Morbidielli's Scaling Model.....	52
II.6.4. Measurement.....	56
II.6.5. Role of Soluble Ions.....	60
II.6.6. Effect of Temperature.....	61
II.7. Tape Casting.....	62
II.7.1. History and Schematic.....	62
II.7.2. Slip Composition and Material Considerations.....	65
II.7.3. Fluid Flow and the Texturing of Slurries during Tape Casting.....	66
II.8. Powder Compaction.....	72
II.8.1. Overview of Compaction Processes.....	73
II.8.1.1. Die Pressing.....	73
II.8.1.2. Isostatic Pressing.....	78
II.8.2. Compaction Curves.....	79
II.9. Particle Packing and Permeability.....	84
II.9.1. Packing of Monomodal Nonporous Spheres.....	84
II.9.2. Packing of particles of Multimodal and Continuous Size Distribution.....	87
III. Method of Attack.....	89
III.1. Objective One: Characterization of Degree of Powder Aggregation.....	89

III.2. Objective Two: Measurement of Strengths of Various Aggregation	
Stages.....	90
III.3. Objective Three: Impact on Packing Characteristics of Various Shear	
Conditions.....	91
IV. Experimental Methods.....	93
IV.1. System of Study.....	93
IV.2. Aggregate Characterization.....	93
IV.2.1. Average Agglomerate Number.....	93
IV.2.1.1. Particle Size Measurement.....	93
IV.2.1.2. Surface Area Measurement.....	94
IV.2.2. Sulfate Measurement.....	95
IV.3. Stress-Controlled Rheometry.....	96
IV.4. Tape Casting.....	96
IV.4.1. Modeling Shear Stresses in a Tape Casting System.....	97
IV.4.2. Tape Casting Procedure.....	97
IV.4.3. Assessment of Packing Characteristics.....	98
IV.5. Compaction Curves.....	98
IV.5.1. Sample Preparation.....	98
IV.5.2. Compaction Procedure.....	99
IV.5.3. Compaction Data Manipulation.....	99
IV.5.4. Linear Regression of Compaction Curve Stages and	
Numerical Calculation of Yield Point.....	101

IV.5.5. Empty Die Compaction Run for Back-Calculation of Machine Compliance.....	102
V. Results and Discussion.....	103
V.1. Powder/Aggregate Characterization.....	103
V.1.1. Powder characteristics.....	103
V.1.1.1. Particle Size Distribution/Specific Surface Area.....	103
V.1.1.2. Soluble Sulfate Level.....	104
V.1.1.3. Scales of Aggregation.....	105
V.1.2. Average Agglomerate Number.....	107
V.1.3. Powder Washing Investigation.....	108
V.2. Determination of Aggregate Scale Yield Strength.....	115
V.2.1. Dynamic Stress Rheometry.....	115
V.2.1.1. Optimal Solids Concentration.....	118
V.2.1.2. Variation of Yield Stresses and Linear Elastic Storage Modulus.....	123
V.2.2. Compaction Curves.....	138
V.3. Phase Three.....	144
V.3.1. Tape Casting.....	144
V.3.2. Mercury Porosimetry.....	149
VI. Conclusions.....	156
VI.1. Particle Characterization.....	156
VI.2. Strength of Aggregation Stages.....	157
VI.3. Impact on Bulk Porosity of Varying Shear Conditions.....	158

VII. Future Work.....	159
VIII. References.....	166
IX. Curriculum Vita.....	171

List of Tables

Table	Description	Page
II.1	Physical properties of Rutile and Anatase	13
II.2	An example of several processes and the typical shear strain rates involved.....	31
II.3	Computed Theoretical Void Volumes for the Packing Models Presented by White and Walton.....	85
V.1	A summary of powder characteristics and computed quantities	103
V.2	A summary of measurements obtained via stress-rheometry	128
V.3	Calculated Yield Points in Compaction.....	144
V.4	A summary of the fit constants for power-law rheology used for the various powders.....	145

List of Figures

Figure	Description	Page
II.1	Schematic of a SCR within a stationary NO _x producing boiler	9
II.2	The rutile (left) and anatase (right) crystal structures (not drawn to scale).....	12
II.3	Flowchart of the sulfate process for production of titanium dioxide.....	14
II.4	Flowchart of the chloride process used to synthesize titanium dioxide.....	15
II.5	Schematic of the flame-hydrolysis technique used to synthesize titanium dioxide.....	16
II.6	An illustration of the various powder length scale classifications and their associated size ranges.....	22
II.7	The various terms for particle groupings illustrated.....	22
II.8	The DLVO curve showing the balance between van der Waals attraction and electrostatic repulsion	24
II.9	An illustration of reducing unit size and self-similar structure propagation; structures represented show increasing fractal dimension from left to right	28
II.10	Comparison of Aggregate Volume and Primary Particle Volume in Computing Average Agglomerate Number.....	30

II.11	Examples of deformation via a tensile stress, σ (top) and a shear stress, τ , (bottom). Dark dashed line represents the plane of action for the stress applied.....	33
II.12	a) Couette drag flow between sliding planes b) Couette drag flow between concentric cylinders c) Poiseuille pressure flow through a cylindrical pipe.....	37
II.13	An illustration of common rheological measurements by type.....	39
II.14	Typical thixotropic behavior exhibited with arrows indicating increasing time and the hysteresis associated with this behavior	40
II.15	Maxwell model with spring and dashpot.....	45
II.16	Linear and non-linear viscoelasticity as distinguished from viscous fluid-like behavior and elastic solid-like behavior.....	46
II.17	The network model in conjunction with Wu and Morbidielli's concepts of (a) 'interfloc' bonding and (b) intrafloc bonding	54
II.18	A schematic of a capillary rheometry assembly	57
II.19	Schematic of a tape casting process; Slurry height, H_0 , tape thickness, h_{tape} , doctor blade thickness, h_0 , doctor blade length, L_0 , doctor blade width, W_0 , casting velocity, U_0	63
II.20	The varying configurations for tape casting (a) Doctor-blade casting (b) Batch casting (c) Rotation casting.....	65

II.21	An illustration of the two scenarios of Pitchumani in the doctor blade channel.....	68
II.22	Schematic of tape casting apparatus with a beveled doctor blade....	71
II.23	Illustration of configurations for single action (left) and dual action punch (right) in die pressing. Arrows indicate pressing action direction.....	74
II.24	Schematic of Reed and DiMilia's setup for measuring stress transmission.....	77
II.25	A sample compaction curve illustrating the various stages.....	80
II.26	Compaction curve uncorrected for machine compliance showing the erroneous high pressure breakpoint.....	82
II.27	Illustration of the various packing models presented by White and Walton.....	86
IV.1	Machine Compliance Curve Obtained via Empty Die.....	102
V.1	Particle size distributions of the powders investigated via light scattering.....	104
V.2	Multiple Aggregation Stages via seen via Scanning Electron Microscopy.....	106
V.3	Powder 3 after a) 1 wash cycle b) 3 wash cycles c) 5 wash cycles...	110
V.4	Powder 5 after a) 1 wash cycle b) 3 wash cycles c) 5 wash cycles...	111
V.5	Particle size distributions of Powder 3 slurries during washing	112
V.6	Particle size distributions of Powder 5 slurries during washing.....	112
V.7	Supernatant Sulfate Level as a Function of Wash Cycle Iteration....	113

V.8	Supernatant pH Measured as a Function of Wash Cycle Iteration...	113
V.9	Micrograph of Particles in the Supernatant Showing a Reduction in Primary Aggregate Size	114
V.10	Powder 2 solids loading buildups for a) 2.3% by volume (5% by weight) b) 6.6% by volume (15% by weight) c) 10.6% by volume (25% by weight) d) 14.2% by volume (35% by weight) e) 17.6% by volume (45% by weight).....	120
V.11	Powder 4 solids loading buildups for a) 2.3% by volume (5% by weight) b) 6.6% by volume (15% by weight) c) 10.6% by volume (25% by weight) d) 14.2% by volume (35% by weight) e) 17.6% by volume (45% by weight).....	121
V.12	Stress-controlled rheometry measurements at 45% by weight for the various powders (Dashed line indicates yield stress).....	127
V.13	Illustration of the reduced networking between powders of greater (left) soluble ion content and greater networking due to lower soluble ion (right) content caused by broader double layer interaction.....	129
V.14	Comparison of Suspension Storage Modulus (G') Prior to Yield with Soluble Sulfate Level of the Powder.....	131
V.15	Comparison of Suspension Yield Stress (τ_Y) with Soluble Sulfate Level of the Powder.....	132
V.16	Time sweep for 45 weight % suspension of Powder 1 at 3-second pulses of an oscillatory stress value of 5.0 Pa.....	134

V.17	Time sweep for 45 weight % suspension of Powder 6 at 3-second pulses of an oscillatory stress value of 3.0 Pa.....	134
V.18	Powder 2 (a) prior to yield (b) upon yield.....	135
V.19	Powder 4 (a) prior to yield (b) upon yield.....	136
V.20	The suspension sample upon yield for (a) Powder 2 (b) Powder 4.....	137
V.21	Compaction curves generated for Powder 1.....	139
V.22	Compaction curves generated for Powder 2.....	139
V.23	Compaction curves generated for Powder 3.....	140
V.24	Compaction curves generated for Powder 4.....	140
V.25	Compaction curves generated for Powder 5.....	141
V.26	Compaction curves generated for Powder 6.....	141
V.27	(a) Extrapolated Yield Points via Compaction for each Powder. Error bars denote 1 standard deviation (b) Extrapolated Yield Points plotted against Sulfate Level	143
V.28	Viscometry of the various powder suspensions.....	146
V.29	Shear profile of Powder 3 for 250 μm blade gap and casting velocity of 0.85 cm/sec.....	147
V.30	Shear profile of Powder 3 for 250 μm blade gap and casting velocity of 0.85 cm/sec.....	147
V.31	Shear profile of Powder 3 for 250 μm blade gap and casting velocity of 0.85 cm/sec.....	147

V.32	Shear profile of Powder 3 for 250 μm blade gap and casting velocity of 0.85 cm/sec.....	147
V.33	Micrographs exhibiting the microstructure of the top surface of tapes corresponding to a) Powder 2 cast at 9.09 cm/sec b) Powder 2 cast at 0.85 cm/sec c) Powder 4 cast at 9.09 cm/sec d) Powder 4 cast at 0.85 cm/sec e) Powder 6 cast at 9.09 cm/sec f) Powder 6 cast at 0.85 cm/sec.....	148
V.34	Mercury porosimetry of tapes cast at 0.85 cm/sec.....	150
V.35	Mercury porosimetry of tapes cast at 9.09 cm/sec.....	150
V.36	2-dimensional comparison of the interstices produces between particles of high aspect ratio (left) and smooth spheres	155
VII.1	Quick network recovery resulting in open assemblages.....	159
VII.2	Slower network recovery resulting in more ordered assemblages....	160

I. Introduction

The use of nanomaterials to form bulk shapes has gained significant attention due to their offering unique properties with regards to rules established for conventional materials as well as their superior inherent advantages for variables such as diffusion length, specific surface area and particle number density. A common drawback of materials exhibiting this length scale is the large amount of fluid vehicle required to facilitate their processability by conventional techniques including paste or slurry formation. Consequences of this include undesired aggregation into micron-sized 'effective units' denying the advantages afforded at the nanoscale.

Titanium dioxide is widely available and broadly used ceramic material that has applications in photovoltaics, pigments and coatings. In this investigation, the applicability of TiO_2 in a de- NO_x catalyst monolith substrate will be addressed. Commonly these materials are synthesized through a sulfate process with numerous intermediate stages providing opportunities to manipulate synthesis variables and produce powders of varying starting properties. The feedstock ilmenite ore is digested via sulfuric acid then washed to remove the iron component before being seeded, washed and ultimately calcined prior to packaging. The powder is then batched in combination with a vanadia source such as ammonium vanadate to serve as the active NO_x reduction catalyst along with a binder plasticizer and lubricant to aid in extrudability. The batch is then extruded into a honeycomb shape then dried and fired.

The extrudability of a paste is strongly dependent on the physical and chemical characteristics of the bulk paste imparted by the source material and its additives.

Frequently the extrusion additives in the batch require lengthy firing cycles that affect production throughput by lengthening the unit production time. Seeking a means to minimize the amount of organic extrusion aids or active catalytic compound by determining the starting powders' role in extrudability and contribution to factors affecting catalytic properties is essential to minimize unit production cost as well as maximizing throughput. It is subsequently the goal of this thesis to investigate the role of starting powder characteristics, specifically aggregation in the extrusion performance of nanosized TiO_2 -based NO_x catalysts.

II. Literature Review

II.1 Selective Catalytic Reduction

II.1.1 NO_x

The United States Environmental Protection Agency (EPA) defines NO_x as the generic term for “a group of highly reactive gases, all of whom contain nitrogen and oxygen in varying amounts.” As of 1998, the EPA identified motor vehicles and other mobile sources as contributing to approximately 49% of the present-day quantities of NO_x, power utilities as providing 27% of current levels of NO_x, Industrial and Commercial sources as providing 19% and all other sources providing 5% of present-day NO_x levels¹.

NO_x is identified as a serious environmental pollutant for its contributions to many problems including¹:

- Contributions to ground-level ozone: NO_x and volatile organic compounds (VOCs) react in the presence of sunlight to produce smog which can damage the lung tissue of children and the elderly
- Formation of nitrate particles and nitric acid vapor: Small particles can penetrate deep into the lungs where they can further damage lung tissue and aggravate existent respiratory ailments such as bronchitis or emphysema
- Contribution to acid rain formation: This can manifest as rain, snow or dry particulate falling to earth and cause damage to vegetation, automobiles, buildings

and historical monuments; furthermore, acidification of lakes and other bodies of water affect its ability to further sustain existing wildlife.

- Water quality deterioration: Increasing nitrogen levels in water leads to an effect known as eutrophication that causes oxygen depletion and further affects aquatic wildlife; this has been especially identified as a harmful situation in the Chesapeake Bay.
- Atmospheric visibility impairment: Nitrate particulate and NO_2 block the transmission of light which impairs visibility in urban areas.
- Formation of toxic chemicals: In air, NO_x can react with common organic chemicals and ozone to form toxic products such as nitroarenes and nitrosamines with potential for causing biological mutations

NO_x has additionally been found to be a contributor to global warming because of its identification as a greenhouse gas^{1,2}.

II.1.2 History of Environmental Regulation

With the rise in automobile transport the United States Congress first identified air pollution as a problem that simultaneously necessitated nationwide legislation and research to combat the problem in 1955 with the passing of the Air Pollution Act. The act is widely believed to have done relatively little in terms of actively tackling the problem beyond merely recognizing air pollution as a national problem. This act was amended twice: once in 1960 to extend funding for this act and once more in 1962 calling for the US Surgeon General to determine the deleterious health effects of air pollution contributed by motor vehicle exhaust³.

In 1963, these actions were followed by the passage of the Clean Air Act (CAA) which set the standards for harmful emissions from stationary sources and motor vehicle exhaust. The act additionally sought to limit pollution from the use of high sulfur bearing coal and other fuels. This act was amended first in 1965 by the passage of the Motor Vehicle Air Pollution Control Act which established standards for automobile emissions and transboundary air pollution, which was concerned with the effects of air pollution on Canada and Mexico as well. Another amendment followed in 1967 with the passage of the Air Quality Act. The Air Quality Act mainly divided the nation into Air Quality Control Regions (AQCRs) and set standards for emissions from stationary sources, regardless of the industry³.

This was followed in 1970 by the Second CAA which placed additional and more stringent standards for emissions from stationary as well as mobile sources. This act sought to place National Air Quality Standards (NAQS) and New Source Performance Standards (NSPS). In particular, the act empowered citizens to take legal action against violators of these standards. Additionally in 1970, the Environmental Protection Agency was created by Congress to carry out and enforce the provisions of this act. Due to the inability to meet the standards set in this act, the deadlines for meeting emissions criteria were extended via amendments to the Second CAA in 1977¹⁻³.

In 1990, more addenda were placed by the passage of the Clean Air Act Amendment (CAAA). Six target materials were identified for limitation: NO_x, SO₂, CO, ozone, lead and particulate matter (PM). Specific deadlines were permitted for the various pollutants based on variations in the severity of each pollutant. Limitations were enacted to deal with existing and new sources of pollutants. To tackle existing sources of

pollutants a limitation known as Reasonably Available Control Technology (RACT) was enacted. This measure placed limitations specifically on facilities that emitted more than the stipulated quantities of volatile organic compounds. For new sources of pollution, three limitations were enacted. New Source Performance Standards (NSPS) were instituted to set standards for existing facilities such as steel plants, lead/zinc refineries and rubber/tire factories while newer facilities were placed under more stringent regulations. Lowest Achievable Emission Rate (LAER) criteria were placed for facilities emitting more than 100 tons/year of NO_x, SO₂, CO, ozone and PM. Best Available Control Technology (BACT) targeted industries that emitted more than 100 tons/year of a target material or more than 250 tons/year of one or more of the aforementioned six target materials³.

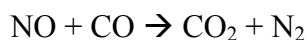
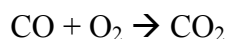
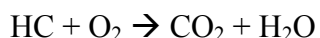
Title IV of the 1990 CAAA eventually resulted in the establishment of the Acid Rain Program in 1995 by the EPA. This program was specifically designed for reduction of quantities of SO₂, NO_x and suppression of acid rain via economically feasible means. In 1999, the Ozone Transport Commission NO_x Budget Program set maximum emission values based on the values from the 1990 CAAA. The targets of this program were 100 steam boilers and 900 thermal-power generation facilities in 12 Eastern US states. In 2005, the Clean Air Interstate Rule was established to further reduce NO_x and SO₂ emissions from coal-fired power plants in 28 eastern US states and the District of Columbia².

Presently under review is an initiative undertaken in 2003 by the Bush administration known as the Clear Skies Initiative, which eventually became the Clear Skies Act. In particular, the Clear Skies Act has sought to cut SO₂ emissions by 73%

from the level present at the time. Further agendas included reduction of mercury emissions by 69% and reduction of NO_x emissions by 67% from levels recorded in 2000. Specifically the initiative sought to have reduced NO_x emissions from 48 tons in 2003 to a maximum of 26 tons by 2010 and ultimately to a maximum of 15 tons in 2018.

II.1.3 Current Technology Implementation

Typically for NO_x removal from both stationary and mobile sources, three different options are utilized. Selective Catalytic Reduction and NO_x adsorber catalysts are utilized for both stationary and mobile sources. A third technique for mobile gasoline-powered sources is the so-called 3-way catalyst where the following reactions occur upon passage of engine combustion products³:



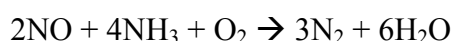
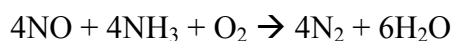
The substrate support for a 3-way catalyst is typically a high surface area alumina body with a surface treatment of washcoated Pt, Pd and Rh as the active catalytic compounds. For stationary sources, the third option is catalytic combustion which uses a PdO catalyst to severely limit the formation of NO_x in a high temperature burner³.

II.1.3.1 Selective Catalytic Reduction

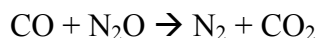
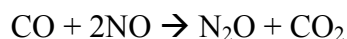
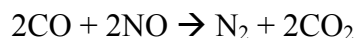
Alternately, heterogeneous catalysts are developed to isolate and attack one of the four aforementioned species. The technology for handling of NO_x has sought to reduce it

to the much less pernicious N_2 gas. Typical means of implementing this conversion usually involve a process called Selective Catalytic Reduction (SCR). The process is named as such usually because in combustion of coal, which is the major application of SCR due to the presence of nitrates in coal, because while reduction of NO_x to N_2 is sought, simultaneously the oxidation of an additional byproduct, SO_x , to SO_2 is desired³⁻⁹.

The SCR reaction typically is achieved by passage of ammonia in the presence of the SCR catalyst bed to produce nitrogen and water vapor, as shown in Figure II.1. This is carried out by one of the following two reactions:



The active catalytic compound that typically carries out the SCR reaction is WO_3 , V_2O_5 or MoO_3 . Most common commercial applications have been documented to specifically use V_2O_5 as the active compound. This system, however, is not unique in its application to NO_x catalysis. This system has also been utilized for the removal of hazardous organic components such as monochlorene benzene via oxidation. Platinum and rhodium are also used as active catalytic compounds in 3-way catalytic converters for mobile sources. The reactions typically employed there are:



Ongoing research towards improving SCR sought to attack existent issues within the process such as ammonia breakthrough (subsequently serving as a pollutant on its own), equipment corrosion and the high cost of ammonia. One option presently under

investigation is the use of methane as the selective reducing agent. This is highly convenient because of the use of methane as an energy source in power and gas-turbine plants. This is referred to as the “new SCR” process or (SCR NO_x HC)⁴.

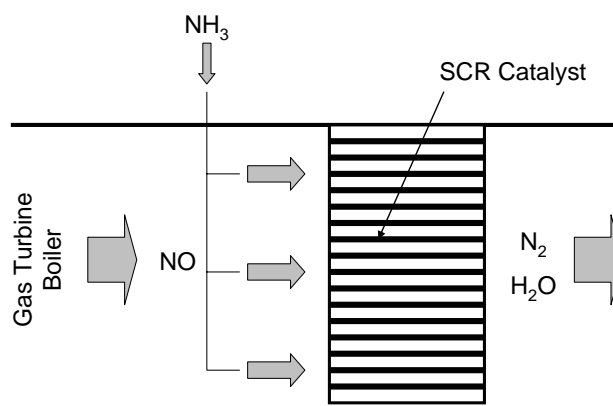


Figure II.1 Schematic of a SCR within a stationary NO_x producing boiler (redrawn from [3])

Alternatives are presently being explored to this mainstream application. Zeolites are also used as an alternative. Additionally, work is presented over the use of layered structures, such as montmorillonites and clays as the substrate material. Work by Olszewska⁵ in particular focuses on the use of montmorillonites with MnO_x as the active catalytic compound in the reduction of NO_x. They cite the variable chemistry of nanosized montmorillonites as being highly beneficial to the catalytic properties of the material.

II.1.3.2 NO_x adsorber catalysts

The alternate mechanism used to tackle NO_x attacks it via an entirely different approach than SCR. Rather than reduce, NO_x adsorption catalysts or NACs, react NO gas with oxygen to form NO₂ gas which readily adsorbs to a platinum catalyst. This platinum catalyst is mounted onto an alkaline earth oxide (e.g. BaCO₃) mounted on a

substrate. The NO_2 undergoes a replacement reaction with the alkaline earth oxide to form an alkaline earth nitrate whereupon CO_2 is released; alternately CO is released and is subsequently fully oxidized by adsorbing onto other free catalyst sites. The drawbacks with this approach, however, are the finite amount of reduction of NO_x adsorption that can occur in addition to the deactivation of the catalyst in the presence of SO_2 ; the latter is specifically avoided in an SCR reaction. This application appears to be sought primarily in automotive and mobile applications while SCR by contrast is desired for stationary NO_x emitters¹⁰.

II.2 Titanium Dioxide

Titanium dioxide (TiO_2) or titania is the most commonly found oxide of titanium metal. Other oxides that exist include titanium monoxide (TiO), titanium sesquioxide (Ti_2O_3), and trititanium pentoxide (Ti_3O_5). Titanium is the ninth most abundant element in the earth's crust, comprising 0.62%¹¹.

The typical source material for titania is either an ilmenite ore or a rutile ore. Ilmenite (FeTiO_3) theoretically yields 52.7% TiO_2 but the actual content has been seen to vary in reality from 43-65%^{11, 12}. Some sources indicate that hard rock primary deposits provide ilmenite of lower TiO_2 content (35-40%)¹³. At times the titania yield can be as low as 8 to 37%¹². Typically a concentration process is utilized to obtain a greater yield of titania from the ore. Typical extraction from rutile ores after concentration yields rutile with a 96% titania yield. Alternately, heavy-mineral beach sand deposits have been seen to provide higher TiO_2 content¹³.

Ilmenite ore is found in large deposits in Quebec, Ontario and Newfoundland, Canada. In the US, major deposits occur in New York, Wyoming and Montana. Other countries with large ilmenite deposits include Norway, Finland, Russia and the Ukraine. Rutile deposits are typically found in aforementioned beach sand deposits along with ilmenite and zircon. Major producing countries include Australia, South Africa and Sierra Leone. Additional rutile-bearing beach sand deposits occur in India, Sri Lanka, Malaysia and Thailand. In the US, these beach sands deposits are located in Florida, New Jersey, Georgia, Tennessee, North Carolina and South Carolina^{11,13}.

The other major alternate source of titania ore is anatase ore in Brazil. Some sources suggest that perovskite ore (CaTiO_3) or titaniferous magnetite can be considered significant TiO_2 sources but concede that processes for extraction from these sources is either economically impractical or still not technologically mature¹³.

II.2.1 Physical Properties

Titania exhibits three known phases: rutile, anatase and brookite. Anatase and rutile are each stable at room temperature. A full list of the properties of titania is presented in Table II.1. Both rutile and anatase are commercially produced in large quantities by many major manufacturers with annual production tonnages ranging as high as 300,000 for some production sites. The relative difficulty of producing brookite coupled with an overall lack of information regarding its stability under room temperature has limited its interest and study. Documented techniques show that synthesis of brookite requires amorphous titania to be heated in the presence of alkali hydroxides at 200-600 Celsius for several days in an autoclave. Two more minor

polymorphs have been documented. One form, referred to as TiO_2 (B), is formed from hydrolysis of $\text{K}_2\text{Ti}_4\text{O}_9$ to form $\text{H}_2\text{Ti}_4\text{O}_9$. The material is then calcined at 500 C followed by removal of K_2O from the system, leaving behind a relatively open structure. The second form, referred to as TiO_2 (ii), is synthesized at high pressures to form an orthorhombic isomorph of $\alpha\text{-PbO}_2$ ^{12,14,15}.

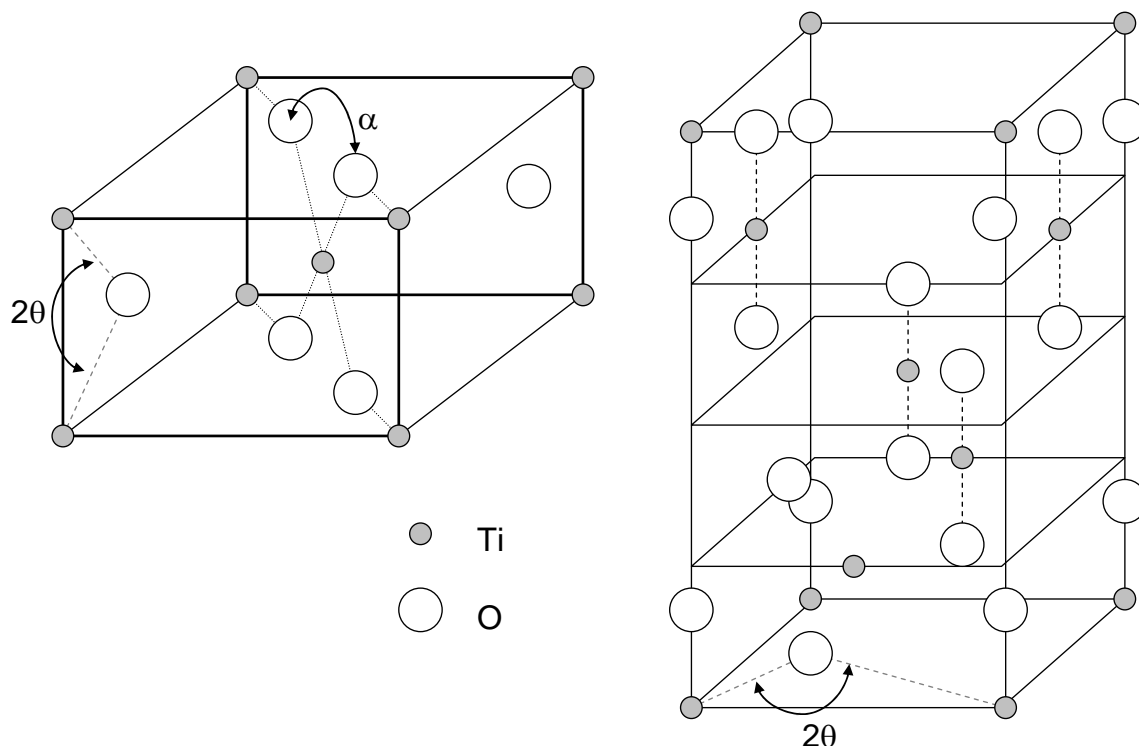


Figure II.2 The rutile (left) and anatase (right) crystal structures (not drawn to scale)

While both phases are stable at room temperature, it is argued that rutile is more stable than anatase. As such, anatase TiO_2 will not directly melt without undergoing a phase transition to rutile first. Both rutile and anatase exhibit tetragonal structures, with variations in the c -axis prompting differences in their electrical and optical properties. Rutile is also the general name for the isomorphs of its namesake. These isomorphs are also typically metal dioxides and include GeO_2 , SnO_2 , RuO_2 and IrO_2 ¹⁴.

For both anatase and rutile, Ti^{4+} is octahedrally coordinated to six O^{2-} ions. Fahmi et al. describe the difference between the two as being the distortion within the octahedral and the assembly as a structure, as seen in Figure II.2. For each system, the nature of the bonding can be characterized by two distinct bond angles as seen in Figure II.2: the Ti-O-Ti bond angle (given by 2θ) and the O-Ti-O bond angle (given by α). Fahmi¹⁵ provides the structural parameters for rutile as having a 2θ value of 98.88 degrees and an α value of 81.12 degrees. Anatase by contrast has a 2θ value of 156.20 degrees and an α value of 78.10 degrees.

Phase	Rutile	Anatase
Crystal System	Tetragonal	Tetragonal
a (Å)	4.59	3.78
b (Å)	4.59	3.78
c (Å)	2.96	9.51
Theoretical Density (g/cm^3)	4.250	3.895
Hardness (Moh's scale)	7-7.5	5.5-6
Band Gap (eV)	3.25	3.04

Table II.1 Physical properties of Rutile and Anatase

II.2.2 Synthesis Techniques

Two major synthesis techniques are used to produce titania, a sulfate process and a chloride process. An illustration of each of these two processes is provided as Figures II.3 and II.4.

The sulfate process used in production of titania began in 1916 and was used by pigment manufacturers through the 1950s. The process starts typically with an ilmenite ore being reacted with sulfuric acid in order to form titanyl sulfate. The source ilmenite ore selection is of great concern during synthesis because of the presence of chromium or vanadium or niobium impurities which could adversely affect the final products applicability as a pigment. Iron typically comprises a large percentage of ilmenite and is removed after digestion with sulfuric acid. The resulting product is a mineral of indefinite composition known as leucoxene. Leucoxene has no specific role other than as an intermediary product in the synthesis of titania. Occasionally it is separated and used as part of an alternative chloride process feedstock including rutile and ilmenite. After removal of the impurities from the system, seed particles are introduced whereupon titania is precipitated from the titanyl sulfate. The powder is then washed with a controlled volume and pH whereupon further precipitation of titania can occur. Finally the titania is calcined in order to remove any impurities remaining in the system^{11-13,16,17}.

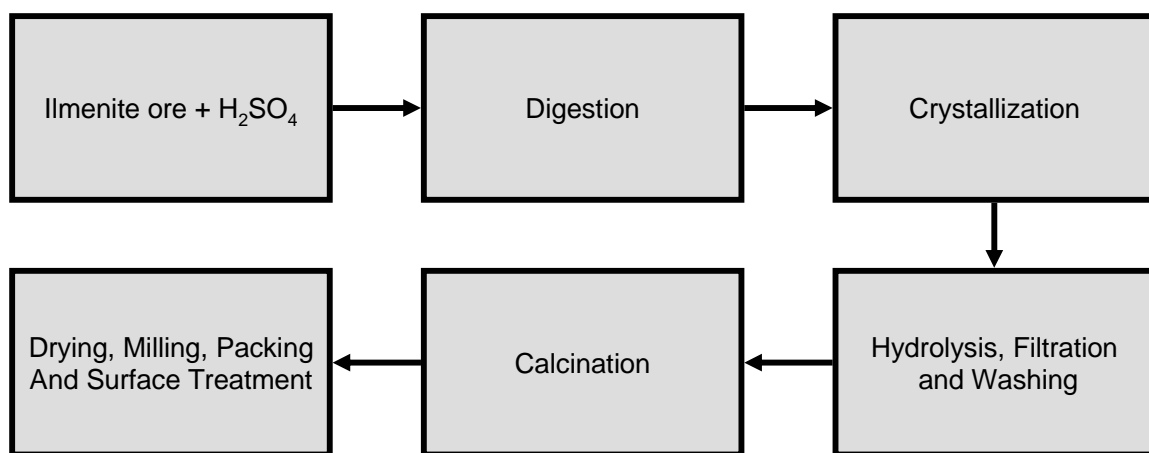


Figure II.3 Flowchart of the sulfate process for production of titanium dioxide

The chloride process was developed as an alternative to the sulfate process by 1958 as an alternative to the sulfate process. The chloride process by contrast utilizes a

rutile ore which is subsequently reacted with chlorine in order to produce titanium tetrachloride (TiCl_4) as well as iron chlorides, and the chlorides of other metal impurities in the ore. The titanium tetrachloride is purified and then converted to TiO_2 via an oxygenating reactor. The chlorine removed from the system during oxygenation is subsequently recycled into the chlorination process, allowing for greater continuity than the far more discrete disjointed steps required in a sulfate process. Additionally, because of the use of a higher titania yielding raw material in addition to the efficiency imparted by recycling the chlorinating agent, the process is favored for large scale synthesis of pigment grade TiO_2 . The process typically yields rutile phase preferentially yet can be manipulated to yield anatase by using anatase seed crystals¹¹⁻¹³.

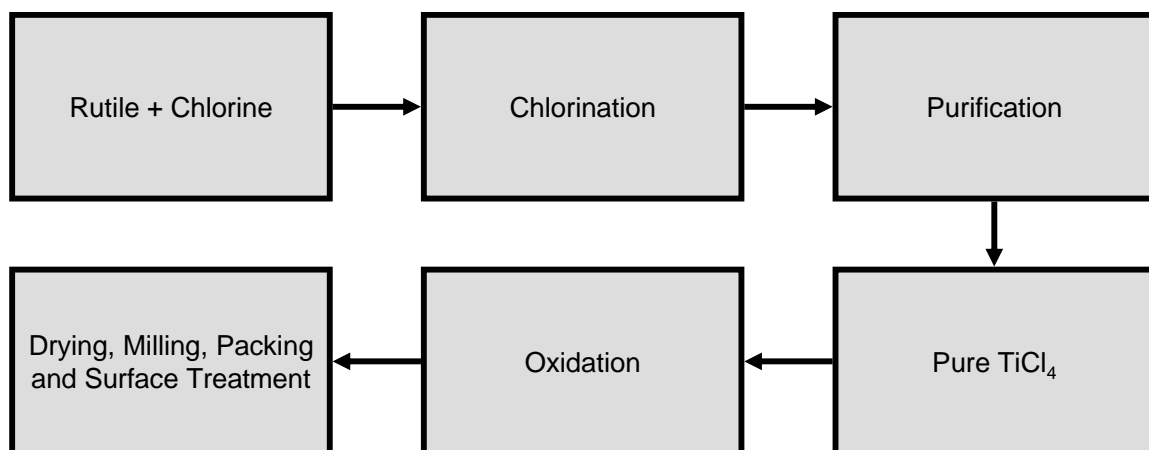


Figure II.4 Flowchart of the chloride process used to synthesize titanium dioxide

A third process utilized by some manufacturers was developed by Degussa GmbH in 1942. This technique, known as a flame hydrolysis process¹⁸ (alternately referred to as the AEROSIL® process) has been used to produce numerous oxide materials, include TiO_2 (from TiCl_4), with a typical feedstock raw material being a chloride or carbonate of the target oxide sought. This is illustrated in Figure II.5. The chloride material is typically carried via an argon flow into a flame of approximately 1000 degrees Celsius

and reacted with a mixture of air and hydrogen whereupon the fumed oxide is produced with a byproduct of HCl gas¹⁹. Dopants are typically added into the system to control powder characteristics such as morphology, phase composition and primary particle size. These dopants typically are other chloride based feedstocks such as PCl_3 , BCl_3 or ZrCl_4 ¹⁹.

Examples of other oxides produced include Al_2O_3 (from AlCl_3), ZrO_2 (ZrCl_4), AlPO_4 ($\text{AlCl}_3/\text{PCl}_3$). The technique can also be used to produce mixed oxide systems such as $\text{Al}_2\text{O}_3\text{-ZrO}_2$ and $\text{Al}_2\text{O}_3\text{-TiO}_2$. Commercial powders produced through this process can be synthesized with particle sizes ranging from 7-50 nm and surface areas ranging from 50-380 m^2/g . However, while this process has been lauded for its ability to produce a higher purity titania (i.e. with a smaller concentration of impurities) this process has also been criticized for its inability to exclusively produce rutile or anatase; frequently a mixture of rutile and anatase results from the process¹². Moreover, the resultant pyrogenic material tends to exhibit a very low bulk density¹⁸.

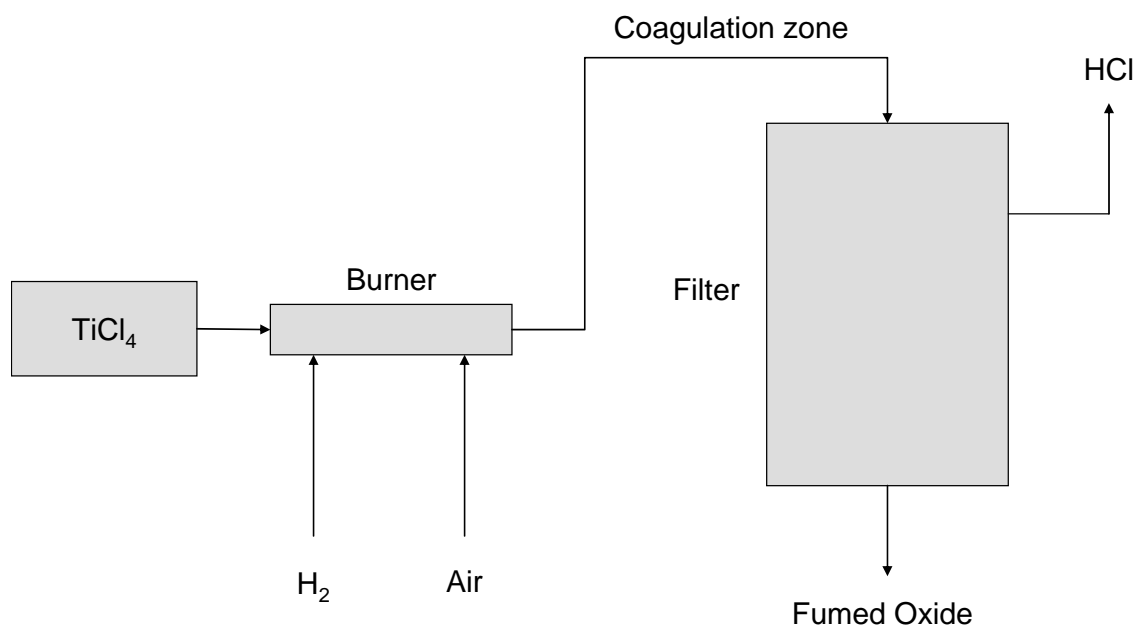


Figure II.5 Schematic of the flame-hydrolysis technique used to synthesize titanium dioxide

II.2.3 Applications

The predominant application among many for titania is in pigments, particularly in the paint industry due to its high refractive index. Additional related applications of titania include a surface coating and a colorant in plastics. Indeed, most of the major applications of titania involve its optical properties. This also extends into the ceramics industry where titanias are used in glazes and enamels. In the latter, the titania also increases the acid attack resistance. Titania is also commonly utilized in a paper coating for its opacifying properties. Typically rutile is used because it has a higher refractive index than anatase (2.76 for rutile vs. 2.55 for anatase)^{11,17}.

The optical properties further apply titania for use as a photocatalyst because of its ability to absorb in the UV range. Anatase is reported to have a wider band gap (3.23 eV) than rutile (3.02 eV). The anatase phase is reported to be preferred because of higher efficiency, yet there is some disagreement on the nature of this discrepancy. Opinions range from the nature of UV irradiation on the recombination of electron-hole pairs and intrinsic crystal phase properties to kinetic parameters rooted in microstructural and powder properties rooted in manufacturing such as porosity and specific surface area. This absorptiveness in the UV range has also led to its use in consumer sun-block products. Other electronic material-based applications include varistors, capacitors. Additionally TiO_2 is used in conjunction with numerous alkaline earth oxides to form perovskite crystal structures^{20,21}.

The environmental applications for TiO_2 include the aforementioned use in catalysis but also include use as an oxygen sensor in automotive applications. Its

chemical and biological inertness have also permitted its use in food, pharmaceutical and cosmetic products¹¹.

II.3 Definitions and Nomenclature

It is necessary to establish clear definitions to establish a clear nomenclature in this thesis. It should be noted that the definitions are applicable to the body of work presented in the results of this study yet may not be applicable to some of the background material. Frequently common terms are used somewhat loosely and interchangeably (this is applicable to some of the background literature to be presented below as well). However, to establish boundaries, if only for the results to be presented further below, the following definitions will be employed²².

II.3.1 Nanosized Material

A nanosized material is defined by Hackley as a material whose average dimensions are smaller than 100 nm. This definition was also used by El-Shall and Edelstein when they delineate nanomaterials as materials whose size range varies from dimers to particles exhibiting diameters up to 100 nm²³.

II.3.2 Colloid

A colloid is a particle whose dimensions are identified as being between 'roughly 1 nm and 1 μ m. On face this would appear to overlap the size range identified as

‘nanosized’. However, the distinction made for colloids is their susceptibility to Brownian motion²⁴.

II.3.3 Ultrafine/Fine

Ultrafine particles are identified as exhibiting a maximum dimension ranging between 1 μm and 10 μm . Fine powders are identified as having a maximum dimension smaller than 37 μm ²⁴.

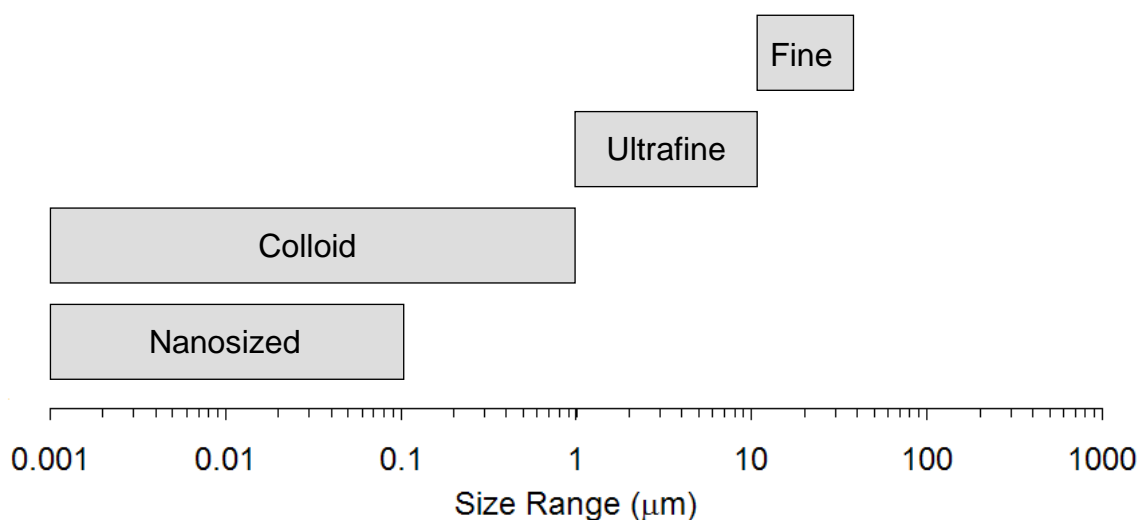


Figure II.6 An illustration of the various powder length scale classifications and their associated size ranges

II.3.4 Aggregate

Aggregate is a term used by Hackley²⁴ to refer to a cohesive mass of subunits. This term appears to be very general in nature and does not stipulate a mechanism for the formation of aggregates. Rather, when a specific mechanism for the formation of an aggregate is invoked, the term aggregate is substituted with either coagulate or floc or agglomerate.

This definition is somewhat corroborated by Shanefield²³ when he describes an aggregate as “small particles [that] have somehow become stuck together very strongly, so that they cannot be easily separated”.

II.3.5 Primary Particle

Primary particles are the subunits of an aggregate. These are the smallest reducible constituents that can be treated as separate individual entities²⁴.

II.3.6 Agglomerate

Agglomerate is defined as being an aggregate in which the primary particles are held together by physical or electrostatic forces. Commonly additional descriptors such as hard-agglomerate or soft-agglomerate are employed. Hackley²⁴, however, appears to discourage the use of such terminology for a lack of precision offered.

II.3.7 Floc

A floc is an aggregate that is formed by the addition of a polymer²⁴.

II.3.8 Coagulate

A coagulate is an aggregate formed by the addition of an electrolyte into the system²⁴.

II.3.9 Aggregation Stages

Multi-tiered aggregation phenomena have been documented in numerous systems. Many of these systems are nanosized due to the multiple length scales afforded before it reaches the micron scale above which agglomerates tend to be highly unstable, often broken down (and reformed in handling stresses).

However, unlike the body of work presented by Hackley, no clear nomenclature has been established to denominate the levels of aggregation seen in various systems. This is primarily because orders of aggregation are largely a function of the synthesis conditions utilized as well as the nature of target material. An example of this can be seen in a system presented by David et al.²⁵, in synthesis of ZnS from a solution technique. They contend that during synthesis, two small units (referred to previously by Hackley as ‘primary particles’; David et al. refer to primary particles as ‘mother crystals’) collide to form a binary doublet. Upon reaching a stable size, the resultant unit is a first stage (or primary) agglomerate; bridges between these primary agglomerates produce an overall stage II (or secondary) agglomerate. Groups of secondary agglomerates will combine to form a stage III agglomerate and so forth.

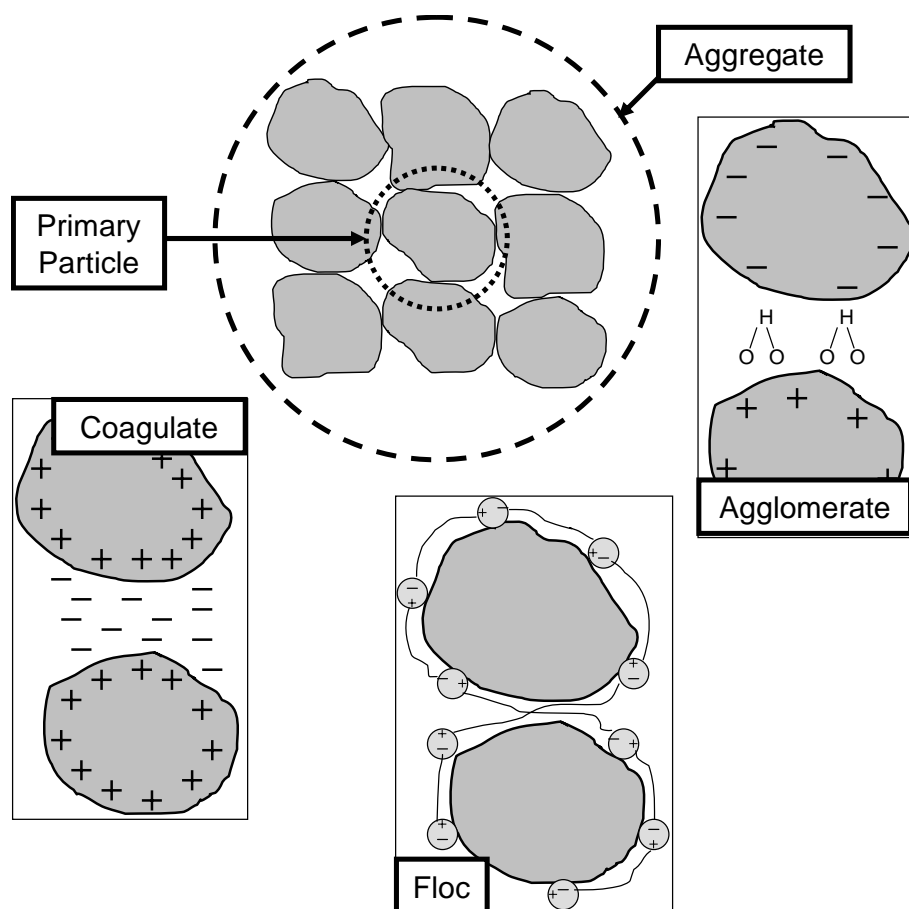


Figure II.7 The various terms for particle groupings illustrated

II.4 Cause of Aggregation

II.4.1 DLVO Theory

The nature of solid charged species in suspension is governed by a theory put forth by Derjaguin, Landau, Verwey and Overbeek, commonly referred to as DLVO theory. DLVO theory establishes that particulate in suspension experience two competing forces: attraction due van der Waals forces and repulsion due to electrostatic forces. Van der Waals forces are the general name for three types of dipole interactions that can occur. Keesom forces are resultant from permanent molecular dipoles producing

an electric field. Induced dipole interactions are known as Debye forces. Finally, London forces are resultant from instantaneous dipoles. Van der Waals forces are described by Horn as being ‘ubiquitous’ and perpetually attractive. All three forces are described by Horn as decaying with as a function of d^{-7} , where ‘ d ’ is the separation between the surfaces of two molecules. For atoms, this decay is a function of d^{-8} . For macroscopic bodies however, the force of attraction exhibits a different dependency. For two spherical macroscopic bodies of radius ‘ R ’, the force of attraction due to van der Waals forces is given by^{26,27}:

$$F = -\frac{AR}{12d^2} \quad \text{II.1}$$

Here, ‘ A ’ is a term known as the Hamaker constant, which is dependent on a number of material constants in the bodies in question.

Electrostatic forces in particulate suspensions are delineated by Horn into nonpolar and polar solvent media. For nonpolar media, electrostatic charges come from surface charge interactions with ions in solution. However, for polar solvent media, which are commonly utilized in ceramic systems (predominantly water) Horn²⁶ contends that the surface of a material immersed will immediately attain a charge in order to satisfy some chemical equilibrium with the surrounding. Oppositely charged counterions will be attracted to the surface of the particle. The surface charge and the surrounding diffuse counter ion cloud constitute what is referred to as the electrical double layer. The thickness of the double-layer is given by a term, κ^{-1} , where ‘ κ ’ is known as the Debye-Huckel parameter. This thickness is given via the following equation²⁸:

$$\kappa^{-1} = \left(\frac{e^2 \sum_i \rho_i z_i^2}{\epsilon_0 \epsilon_r kT} \right)^{-0.5} \quad \text{II.2}$$

Here, ' e ' is electronic charge; ' ρ_i ' is the number density of species i ; ' z_i ' is the valence charge of species i ; ' ϵ_0 ' is the dielectric permittivity of a vacuum; ' ϵ_r ' is the relative permittivity of the medium²⁸.

It can be seen from this equation that the thickness of the electrical double layer will be inversely related to the quantity of charged ionic species in the system. However, Gouy and Chapman further complicate this model by arguing the Coulombic interactions with the counterions in suspension are in fact screened interactions and as such, the force of repulsion for a distance, ' d ', outside the electrical double layer for counterions is given as²⁸:

$$F = \left(\frac{64 \rho kT}{\kappa} \right) \left[\tanh \left(\frac{ze\psi_0}{4kT} \right) \right]^2 \exp(-\kappa d) \quad \text{II.3}$$

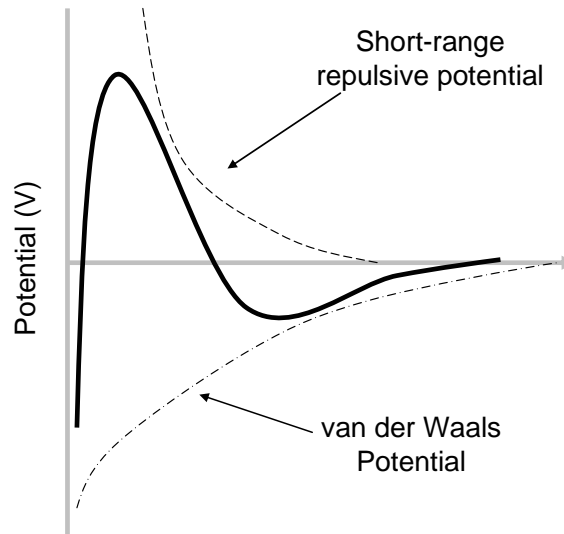


Figure II.8 The DLVO curve showing the balance between van der Waals attraction and electrostatic repulsion

Here, ' ρ ' is the summation of the charge densities for all components; ' ψ_0 ' is the surface potential of the particle; the competition between electrostatic repulsion and van der Waals attraction is illustrated in the DLVO curve in Figure II.8.

II.4.2 Exacerbation at the Nanometer Length Scale

Kallay and Zalac²⁹ take this a step further. They argue that in a polar solvent medium (such as water), a hydration layer is formed around a particle. Their argument is that a reduction to the nanometer length scale creates several problems for the conventional approach to a colloidal system. They argue that DLVO theory cannot be utilized because the creation of a hydration layer is dependent on the charge generated at the surface of the particle. Moreover, this hydration layer shows a weak (if any) dependence on the size of the particle and as such, the hydration layer begins to approach the size of the particle. With the proliferation of particle number density at this length scale, the effective particle size produced as a result of forming this diffuse layer, systems of nanoparticles are far more prone to aggregation because of the significantly increased occurrence of double-layer overlap. Furthermore, the increased particle number density also contributes to a relative increase in particle collision frequency. Their approach uses a Bronsted-acid since they argue that ionic contributions dominate at this length scale. Their argument ultimately is that the particle size of a system is inversely related to the particle number density and collision frequency by factors of a^3 and a^6 respectively, where ' a ' is the particle diameter. Their specific example that they postulate involves a system where the particle size is reduced 10-fold from 30 nm to 3 nm resulting in what

they believe to be a 1,000-fold increase in particle number density and a particle collision frequency that is 1,000,000 times greater.

II.5 Modeling of Aggregate Systems

The modeling of the aggregate system is inherently complicated by the irregular geometry of the structures that aggregates will assemble into. Modeling of such systems is frequently related by empirical measurements and observations. Examples of such have previously included average size and reciprocal packing efficiency.

II.5.1 Number of Spheres

One such empirical parameter is offered by van de Ven and Hunter³⁰. They offer an equation which quantifies the degree of aggregation by estimating the ‘number of spheres’ comprising the aggregate. In particular, they offer the following equation:

$$n_s = \frac{a^3}{C_{FP} r^3} \quad \text{II.4}$$

Here ‘ n_s ’ is the number of spheres comprising the aggregate; ‘ a ’ is described as being the floc radius; ‘ C_{FP} ’ is the ratio of the volume fraction of aggregates to the volume fraction of the particles; ‘ r ’ is the radius of the primary particle. However, their experimental technique documents relatively imprecise methods such as turbidity to measure ‘ a ’ with calibration performed by extrinsic measurement of the flocs via photography.

II.5.2 Fractal Dimension

Fractal dimension is another term that has been found suitably applicable to describing the nature of aggregate systems. The term was initially developed by Benoit Mandelbrot³¹ in his investigation to measure the length of the English coastline in the 1970s. Yet the concept of fractals has existed for centuries beforehand to describe a structure that is self propagating with continuing reduction in the length scale. The classic example used of a fractal structure is typically a snowflake. Mandelbrot's coining of the term 'fractal' is rooted in the Latin word 'fractus' meaning 'broken'. Sorensen et al.³² provide the following equation to relate primary particles and aggregates via fractal dimension.

$$N = k_0 \left(\frac{R_g}{a} \right)^{D_f} \quad \text{II.5}$$

Here ' N ' is referred to as 'the number of monomer primary particles' comprising the aggregate; ' k_0 ' is a prefactor term; ' R_g ' is the radius of gyration of the aggregate; ' a ' is the aggregate radius; ' D_f ' is the fractal dimension term. The equation provided by Sorensen is noteworthy for several reasons. Firstly, it is likely the most complete equation regarding fractal dimension because of its inclusion of the prefactor term, k_0 . The prefactor is often excluded by others^{33,34}, possibly because it often is discarded. Taking logarithms of both sides yields a linear relationship between $\ln N$ and $\ln (R_g/a)$ with the slope of the equation being D_f and with any extraneous coefficients that are not functions of particle or aggregate radii from the initial equation reduced to serving as a intercept term in this manipulation. Wu et al.³⁵ contend that this term (which they refer to simply as ' A ' in their investigation) is of the order of unity in a study regarding aerosols of chromium oxide and silver aggregates.

DeBoer identifies boundary conditions for D_f as 1 and 3. Each boundary condition represents a different qualitative extreme regarding the nature of an aggregate with $D_f = 1$ representing a densely aggregated structure and $D_f = 3$ representing an open, loose, porous aggregate. A more intuitive understanding is provided by Mandelbrot et al.³¹ in suggesting that $D_f = 1$ represents a closed convex structure whereas $D_f = 3$ represents a structure similar to a snowflake^{31,33}.

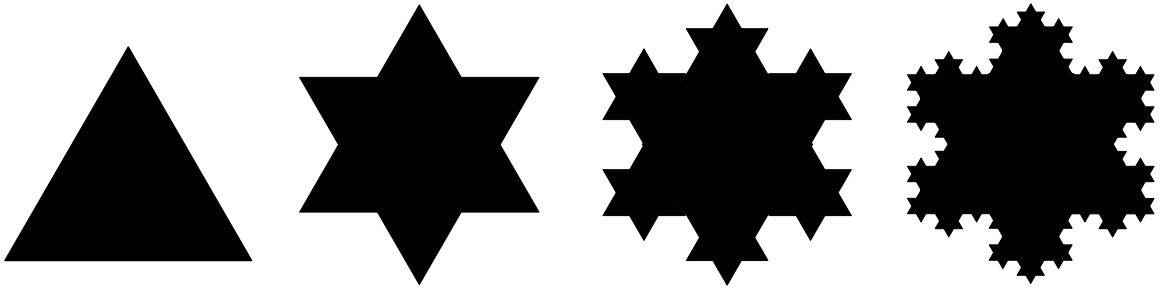


Figure II.9: An illustration of reducing unit size and self-similar structure propagation; structures represented show increasing fractal dimension from left to right

Fractal dimension becomes a useful term when considering aggregation mechanisms. For small particles where Brownian motion becomes significant, two specific regimes are identified: Diffusion-Limited Colloid (or Cluster) Aggregation (DLCA) and Rate-Limited Colloid Aggregation (RLCA). Tang³⁶ differentiates these regimes by a parameter referred to as the ‘sticking probability’. DLCA is given by a sticking probability of one while RLCA is for sticking probabilities much less than 1. Subsequently, DLCA is identified as the regime when the repulsive forces are negligible in the system. By contrast, in RLCA particle “monomers” will undergo numerous collisions before sticking, making the sticking probability very small. Each of these mechanisms exhibit different relationships with regards to fractal dimension. Tang cites work identifying two distinct fractal dimensions for the different mechanisms (1.8 for

DLCA and 2.1 for RLCA). Moreover, for systems undergoing aggregation, the change in the aggregate hydrodynamic radius, ‘ R ’, with time, ‘ t ’, varies as a function of the regime.

For DLCA:

$$R \propto t^{1/D_f} \quad \text{II.6}$$

For RLCA:

$$R \propto \exp(\Gamma t) \quad \text{II.7}$$

Here, ‘ Γ ’ is a function of experimental conditions³⁶.

II.5.3 Average Agglomerate Number

Another term that can be used to quantify an aggregate system is known as the Average Agglomerate Number (AAN). The AAN is computed via the following equation²⁴:

$$AAN = \left(\frac{d_{50,hv}}{ESD_{BET}} \right)^3 \quad \text{II.8}$$

Here ‘ $d_{50,hv}$ ’ is the median diameter obtained via light scattering; ‘ ESD_{BET} ’ is the equivalent spherical diameter computed via BET Nitrogen Adsorption. It is calculated by²⁴:

$$ESD_{BET} = \frac{6}{SSA \times \rho_{particle}} \quad \text{II.9}$$

Where ‘ SSA ’ is the specific surface area; ‘ $\rho_{particle}$ ’ is the particle density. See Figure II.10.

Substituting into the original equation yields:

$$AAN = \left(\frac{d_{50,hv} \times SSA \times \rho_{particle}}{6} \right)^3 \quad \text{II.10}$$

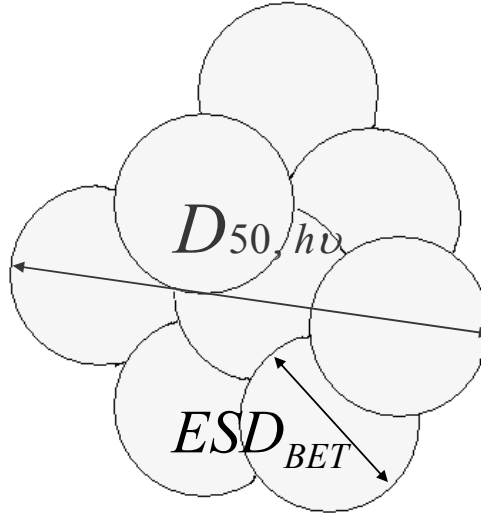


Figure II.10 Comparison of Aggregate Volume and Primary Particle Volume in Computing Average Agglomerate Number

Equation II.10 can be noted for its similarity to Equation II.4 because with the exception of the correction factor, C_{FP} , the terms used are the similar. Average Agglomerate Number, therefore, offers a means to obtain estimate for the number of primary particles comprising an aggregate. It should be noted that the AAN of an aggregate serves an estimate of the degree of aggregation of a system and not an exact quantification of the exact number of primary particles (this is difficult to achieve in general). Moreover, with considerations of terms such as ESD_{BET} and d_{50} , it offers a means to evaluate primary particle and aggregate sizes respectively.

II.6 Rheology

Rheology is the science of deformation and flow. The term that was invented at Lehigh University by a professor named Eugene Bingham (after whom a particular rheological model is named) originating from the Greek word for flow. Rheology is of significant concern in the ceramic industry because of the extensive use of suspensions and pastes to serve as carriers for ceramic powders during forming techniques. Some examples of flow properties dependent on solute properties cited by Galassi³⁶ et al. include particle physics, interfacial chemistry and other rheological characteristics. Moreover, numerous processes can be distinguished by the shear strain utilized (see Table II.2). It subsequently becomes of great concern to understand the nature of the fluid suspension in these varying regimes.

Process	Typical shear strain rate range involved
Screw extruder	10^0 - 10^2 s ⁻¹
Dip Coating	10^1 - 10^2 s ⁻¹
Spraying/Brushing	10^3 - 10^4 s ⁻¹
Blade coating	10^5 - 10^6 s ⁻¹
Lubrication	10^3 - 10^7 s ⁻¹

Table II.2 An example of several processes and the typical shear strain rates involved (from [38])

II.6.1 Basic Principles

In order to understand basic principles of rheology it is important to begin by identifying the different kinds of stresses and deformations that can occur in materials. A linear elastic solid material is conventionally believed to be analogous to a Hookean

spring. In such a material, an applied uniaxial force results exclusively in elastic deformation. This deformation is referred to as strain, and can be understood via the following equation³⁸:

$$\frac{L_f - L_i}{L_i} = \frac{\delta L}{L} = \varepsilon \quad \text{II.11}$$

Here, ' L_f ' is the final length after deformation; ' L_i ' is the initial length; ' ε ' is the strain [unitless].

Consider the classical Hookean spring which is governed by:

$$F = k * \delta L \quad \text{II.12}$$

Where ' F ' is the force of extension, and ' k ' is the spring constant. The force resulting in strain is commonly represented in the form of stress. Stress is defined as force divided by the area over which the force is applied. For elastic solids, the stress and strain are conventionally related by the following equation³⁸:

$$\sigma = E\varepsilon \quad \text{II.13}$$

Here, ' σ ' is the normal stress; ' E ' is the elastic or Young's modulus. This is typically an extension of the Hookean solid model. Alternately, Macosko contends that materials such as rubber can exhibit Neo-Hookean behavior whereupon the stress is linear with the square of the strain³⁸.

In solid bodies, two types of stresses can be identified depending on their relationship to the plane on which they are applied. If a stress is applied normal to its plane of application, it is referred to simply as a normal stress. Pure compression and tension are examples of normal stresses and their potential directionality. However, if the plane of application is in fact parallel to the direction of the stress applied, then in fact the stress is referred to as a shear stress. This is illustrated in Figure II.11.

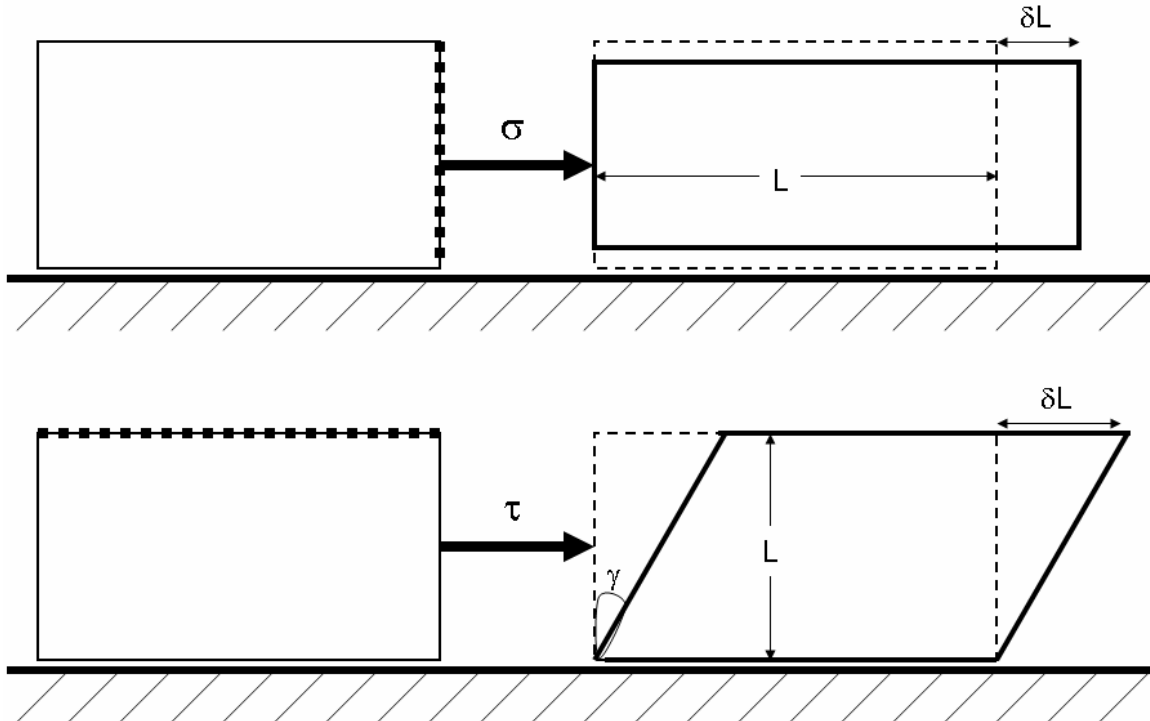


Figure II.11 Examples of deformation via a tensile stress, σ (top) and a shear stress, τ , (bottom). Dark dashed line represents the plane of action for the stress applied

For shear stresses, the deformation and the initial length are related via an angle, ' γ ', whereupon the strain in the system is seen to be related to gamma as:

$$\frac{\delta L}{L} = \tan \gamma \quad \text{II.14}$$

However, since the deformations are typically small and subsequently make ' γ ' small, then:

$$\frac{\delta L}{L} = \tan \gamma \cong \gamma \quad \text{II.15}$$

Much like how normal stress and normal strains are related by the elastic modulus as a constant of proportionality, shear stress and shear strain are related by a value ' G ', known as the Shear Modulus.

$$\tau = G\gamma \quad \text{II.16}$$

Here ‘ τ ’ is the shear stress and ‘ γ ’ is the shear strain.

In considering stresses applied to a fluid, Newton argued that there was a linear relationship between the velocity gradient of fluid layers and the “resistance” applied. The resistance can be interpreted to mean the shear stress while the velocity gradient can be manipulated to seen as the time derivative of shear strain, the shear strain rate. Subsequently, Newton’s law of viscosity was suggested by the following equation^{38,39}:

$$\tau = \eta \dot{\gamma} \quad \text{II.17}$$

Here ‘ τ ’ is the shear stress; ‘ η ’ is the apparent viscosity of the fluid; ‘ $\dot{\gamma}$ ’ is the shear strain rate.

In this particular instance the viscosity can be seen as the ratio of the shear stress to the shear strain rate. For the case of Newtonian fluids, this is further referred to as the ‘apparent viscosity’, ‘ η_a ’, with:

$$\eta_a = \frac{\tau}{\dot{\gamma}} \quad \text{II.18}$$

Generally, however, the dynamic viscosity is defined as:

$$\eta = \frac{d\tau}{d\dot{\gamma}} \quad \text{II.19}$$

In SI units, viscosity is recorded Pascal-seconds (with shear stress in units of Pascals and shear strain rate in terms of sec^{-1}). Alternately, viscosity can be measured in terms of Poise where 1 Poise = 0.1 Pa sec.

Alternately, fluids are also considered in terms of the kinematic viscosity, ‘ ν ’, which is defined by:

$$\nu = \frac{\eta}{\rho} \quad \text{II.20}$$

Here ‘ ρ ’ is the fluid density. Kinematic viscosity as a term is used as a ratio of viscous forces to inertial forces. As such, its role is far more prevalent in discussions of a scenario known as turbulent flow, which is discussed below. With dynamic viscosity recorded in Pa sec and density in kg/m^3 , the units of kinematic viscosity are m^2/sec . Commonly this is simplified to units of Stokes with 1 Stokes being equal to $10^{-4} \text{ m}^2/\text{sec}$.

Fluid flow occurs in one of two forms. Patton describes one scenario as “layers of liquid slid[ing] over each other in an orderly fashion”. This is referred to as laminar flow. Alternately this is called viscous or Newtonian flow. The other scenario is described as “a swirling chaos of eddies and vortices” and is commonly referred to as turbulent flow³⁹.

Laminar flow occurs for generally low shear strain rates in a fluid. At a critical strain rate the system will undergo a transition to turbulent flow. This is described best by a parameter known as the Reynolds number. The Reynolds number historically was used to characterize fluid flow in a pipe. It is calculated from the following equation:

$$\text{Re} = \frac{2\bar{v}D_L R}{\eta_L} \quad \text{II.21}$$

Here, ‘ Re ’ is the Reynolds number [unitless]; ‘ \bar{v} ’ is the average flow velocity; ‘ D_L ’ is the density of the fluid; ‘ R ’ is the radius of the pipe; ‘ η_L ’ is the viscosity of fluid³⁹.

There is some minor disagreement on the Reynolds number value signifying the transition from laminar to turbulent flow. Patton³⁹ contends this occurs for a Reynolds number value of 2000. Reed⁴⁰ more recently has reported a value of 2100 signifying the onset of a transition with full turbulent flow beginning at $\text{Re} > 3000$. Busse⁴¹ has reported that there is some discrepancy regarding the value of the Reynolds whereupon the transition from laminar to turbulent flow occurs. Specifically Busse cites that the transition to turbulent flow is dependent on the nature of the system in which flow is

occurring. For example, in flow between parallel plates, the transition can occur for values as low as 1500 or as high as 7696. Busse further reports that the discrepancy in values for flow through a pipe can be even greater yet does not present examples of values to support this.

Typically laminar flow is preferred to turbulent flows because laminar flow is reflective of bulk properties which become much easier for characterization and subsequent modeling of the system. Some exceptions, as cited by Reed, include spray drying where a turbulent flow is sought. For regions of laminar flow Macosko divides flow into two regimes: viscous drag flow and pressure flow³⁸.

As can be seen in Figure II.12 a) for flow between two plates and in Figure II.12 b) for flow between concentric cylinders, the velocity profile of the liquid indicates a maximum when in the plane of shear, and zero at the plane of zero motion relative to the shear plane. Couette flow allows linear interpolation for determining the velocity of the fluid at a parallel plane located between the aforementioned two. In Figure II.12 c) Poiseuille flow indicates a parabolic velocity profile over the cross section of flow through a cylindrical pipe and is given by the following equation:

$$\Phi = \frac{\pi R^4}{8\eta} \frac{|\Delta P|}{L} \quad \text{II.22}$$

Here, ' Φ ' is the volumetric flow rate; ' R ' is the inner radius of the pipe; ' ΔP ' is the pressure gradient between the ends of the pipe; ' L ' is the length of the pipe.

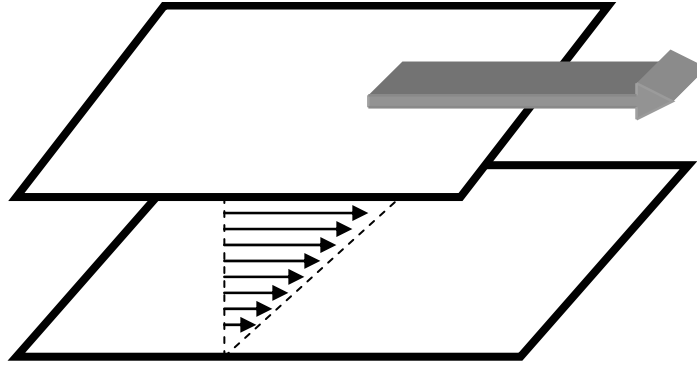


Figure II.12 a) Couette drag flow between sliding planes (redrawn from [38])

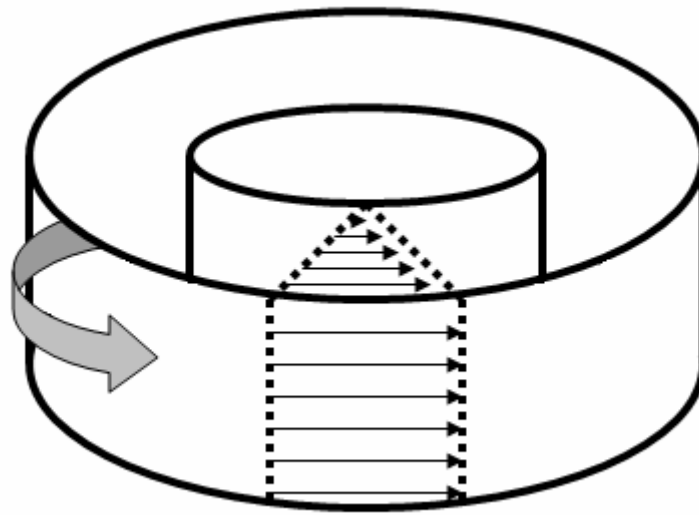


Figure II.12 b) Couette drag flow between concentric cylinders (redrawn from [38])

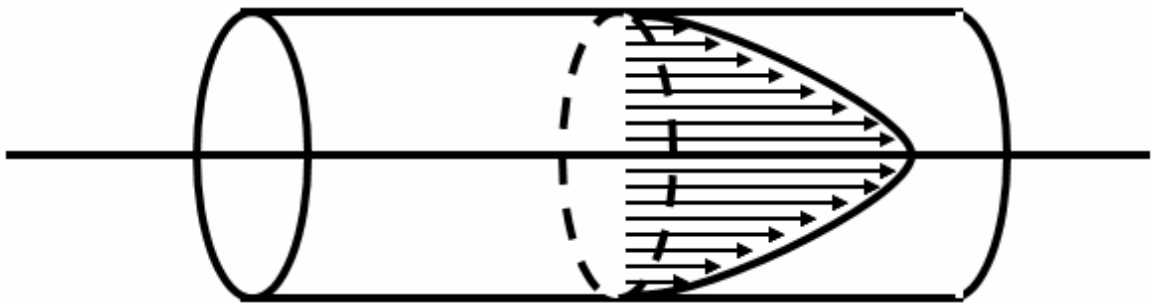


Figure II.12 c) Poiseuille pressure flow through a cylindrical pipe (redrawn from [38])

Flow velocity is maximized at the center of the pipe and zero at the walls. However, as Nycz⁴² notes, the planar Couette model is only applicable for systems

exhibiting Newtonian behavior. For systems exhibiting more complex rheological profiles, the shear profile becomes inherently more complicated.

In turbulent flow by contrast, the shear energy results in the formation of local flow eddies which eventually reach a stable equilibrium size. The length scale, η_k , for which these stable eddy currents form, can be expressed as:

$$\eta_k = \left(\frac{\nu^3}{\varepsilon} \right)^{1/4} \quad \text{II.23}$$

Here, ' ν ' is the aforementioned kinematic viscosity while ' ε ' is the energy dissipation rate of the system. The term ' η_k ' is typically referred to as the Kolmogoroff scale and is typically used as an equilibrium internal scale of turbulence⁴³.

II.6.1.1 Flow Models

Typically in rheology, the shear stress and the viscosity are treated as dependent variables while the applied shear strain rate is kept as an independent variable. A suitable model to fit these is often determined empirically based on data acquired. As such, the relationship between the viscosity, shear stress and the shear strain rate is found to be highly dependent on the system being studied. However, there are specific general models for this relationship into which the system is classified.

Typically, in acquiring data for shear strain rate against measured shear stress, the data are empirically categorized for the nature of its curvature. An example of several of these cases can be seen in Figure II.13. Typically, linear behavior on this curve without an observed yield point is referred to as Newtonian behavior. The increase in the shear stress required to facilitate flow for increasing strain rates is referred to as dilatency or

shear thickening. The opposite of dilatency is called pseudoplastic or shear thinning behavior³⁸.

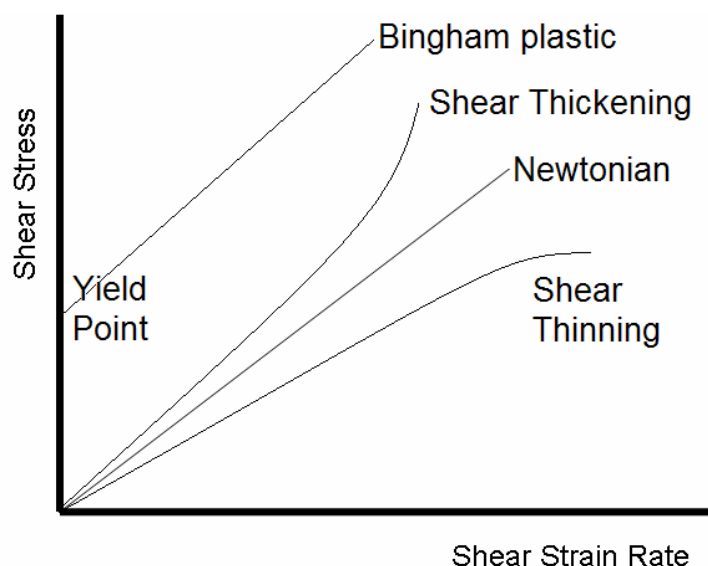


Figure II.13 An illustration of common rheological measurements by type

Each of these situations is predicated on not exhibiting two particular characteristics. Firstly, there can be no apparent initial yield stress value to cause flow. The existence of a yield point results in classifications such as the illustrated Bingham plastic model. The second characteristic that is not exhibited by any of the aforementioned systems in order to remain applicable is a time-dependency. Introduction of a time-dependency via hysteresis in variation of shear stress against shear strain rate automatically classifies a rheological system as being thixotropic (see Figure II.14). General rheological models offer specific cases that can identify a system according to one of the trends described above.

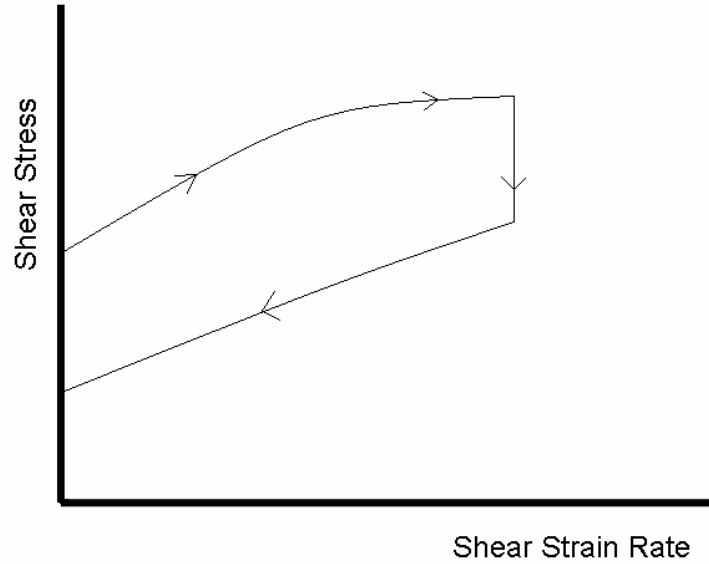


Figure II.14 Typical thixotropic behavior exhibited with arrows indicating increasing time and the hysteresis associated with this behavior.

II.6.1.1.1 Newtonian

The simplest model is the aforementioned Newtonian model. Manipulating equation II.18, it can be seen that the Newtonian relationship for viscosity is:

$$\eta = \frac{\tau}{\dot{\gamma}} \quad \text{II.24}$$

Newtonian fluids are noteworthy because the viscosity of a Newtonian fluid is independent of the shear rate applied. Additionally, Newtonian fluids do not possess a yield stress, meaning that there is no initial yield stress to overcome to facilitate fluid flow³⁸.

II.6.1.1.2 Casson

Another model that is used is the Casson model. This model uses the following relationship³⁸:

$$\tau^{0.5} = k_1 + k_2 \dot{\gamma}^{0.5} \quad \text{II.25}$$

The constants ' k_1 ' and ' k_2 ' are referred to as structure-dependent constants for the system. Casson's model regards the fundamental units controlling the viscosity as being chain-like. Reed⁴⁰ further describes the general form of the Casson model as:

$$\eta_a^m = \eta_\infty^m + \left(\frac{\tau_Y}{\dot{\gamma}} \right)^m \quad \text{II.26}$$

Here ' η_a ' is the apparent viscosity; ' η_∞ ' is the viscosity at a high strain rate after the aforementioned chain-units are sufficiently broken down; ' m ' is an empirical constant indicating deviation from linearity.

II.6.1.1.3 Power-law

Another typical rheological model that is commonly used is the power law rheology model. It is based on the following relationship^{38,44}:

$$\tau = A|\dot{\gamma}|^n \quad \text{II.27}$$

This is alternately sometimes referred to as the Ostwald-de Waele power-law equation⁴⁵. Combining equation II.19 with this, yields:

$$\eta = m\dot{\gamma}^{n-1} \quad \text{II.28}$$

Here, Macosko³⁸ contends that whether $n > 1$ or $n < 1$ can be indicative of shear thinning or thickening behavior in the system. Other efforts at relating the empirical constants to physical parameters are described by Pitchumani⁴⁵ in discussing the Ostwald-de Waele model. He cites earlier work which presents the following relationships:

$$A = C_0 \eta_0 (T_{sl}) (1 - \phi)^{C_1} \quad \text{II.29}$$

$$n = C_2 \log(1 - \phi) + 1 \quad \text{II.30}$$

Here, ' C_2 ', ' C_1 ' and ' C_0 ' are also empirical constants while ϕ is the solids volume fraction in the slurry, ' η_0 ' is the solvent viscosity and ' T_{sl} ' is the slurry temperature.

II.6.1.1.4 Cross

The Cross (or Carreau) model was proposed to provide Newtonian behavior at high and low shear rates. For intermediary shear rates, this is given by³⁸:

$$(\eta - \eta_\infty) \cong (\eta_0 - \eta_\infty) m \dot{\gamma}^{n-1} \quad \text{II.31}$$

II.6.1.1.5 Bingham

Another class of material to be considered is the Bingham plastic. This is described by Benbow⁴⁶ as being incapable of flow for stresses below what is referred to as a yield stress. Taking this into account allows modification of Equation II.24 into:

$$\tau - \tau_i = \eta \dot{\gamma} \quad \text{II.32}$$

Reed⁴⁰ contends that the initial yield point, ' τ_i ', may be present in ceramic systems of high particle concentration or which form "a linkage of bonded molecules and particles". This yield point represents the stress required to stretch, deform and/or ultimately break this linkage and precipitate fluid flow.

II.6.1.1.6 Herschel-Bulkley

One such possibility afforded by the Bingham plastic model is the Herschel-Bulkley fluid. This model uses the following relationship between the shear stress and shear strain rate³⁸:

$$\tau = \tau_y + \eta \dot{\gamma}^n \quad \text{II.33}$$

In some instances, the Herschel-Bulkley fluid falls under the general classification of the Bingham plastic model, since the aforementioned Bingham plastic of Equation II.32 is equivalent to Equation II.33 with $n=1$. However, the generally agreed convention is that for $n \neq 1$, the fluid is a Herschel-Bulkley fluid^{38,46,47}.

II.6.1.2 Thixotropy

The various rheological models listed above describe situations where the properties observed are shear stress or shear strain rate dependent. Additionally, time-dependent phenomena can be observed in systems. Galassi³⁷ contends that time-dependency is often exhibited in highly concentrated suspensions. Such phenomena are believed to exist due to kinetic phenomena controlling the shear dependency of the system and typically associated with changes in the aggregation behavior of the system. Thixotropy is typically identified with systems exhibiting shear-thinning behavior as a function of time. The opposite scenario (i.e., a system exhibiting shear thickening behavior as a function of time) is often referred to as being anti-thixotropic, yet conceded to be less prevalent than the former.

One means by which thixotropy can be observed is in time dependent gelation properties of a suspension. Reed⁴⁰ presents a means of tabulating and measuring the thixotropy by the following equation:

$$B_{gel} = \frac{\tau_{y2} - \tau_{y1}}{\ln\left(\frac{t_2}{t_1}\right)} \quad \text{II.34}$$

Here, ' τ_{Y2} ' and ' τ_{Y1} ' are the yield points of a gel at time ' t_2 ' and ' t_1 ', respectively, while ' B_{gel} ' is an index of structural buildup. The B_{gel} term can be substituted for ' B_{thix} ' which substitutes the differences in plastic viscosities, η_{pl} .

Another possibility offered by Galassi³⁷ is modeling the yield stress decay as a function of time via an exponential decay. Galassi contends that stress recovery with time in a thixotropic system is analogous to chemical reaction kinetics. Indeed, it is conceded that the phenomenon governing the time dependent behavior, such as aggregation, gelation or cross-linking are rooted in similar mechanisms. In accordance with such, the following equation is suggested:

$$\tau = \tau_e + (\tau_e - \tau_i) \exp(-kt) \quad \text{II.35}$$

Here ' τ_e ' and ' τ_i ' are the equilibrium and initial shear stresses respectively while ' k ' is the kinetic constant, which Galassi contends is only dependent on the shear strain rate.

II.6.2 Viscoelasticity

The aforementioned arguments would lead one to believe that materials discretely exhibit either viscous fluid-like behavior or elastic solid-like behavior. However, numerous materials such as gum or rubber have been observed to exhibit a sort of intermediate behavior that obscures this classification. Such materials, under an applied load, do not exhibit the instantaneous recovery to the retraction of the load like a viscous liquid, yet exhibit a slow recovery instead of permanent deformation that would typically be seen in an elastic body. The (creative) term coined to describe this phenomenon is visco-elasticity, suggesting a combination of both these behaviors. In particular,

viscoelastic systems are observed for the time-related behavior with respect to applied shear³⁸.

Ordinarily one would automatically associate viscoelasticity as a subset of thixotropy due to the inherently time-dependent properties. However, as Galassi³⁷ argues, this is a specious argument because responses to stresses and strains in thixotropic systems are typically instantaneous as opposed to the aforementioned definition of viscoelastic behavior. The terms, however, are not mutually exclusive as both types of behavior can coexist in a suspension.

While elasticity of a body is predicated on the Hookean solid model, linear viscoelastic systems are established as conforming to the Maxwell model. This is illustrated in Figure II.15. The time dependent recovery of the system is expressed by the presence of a dashpot to dampen the elastic oscillations³⁸.

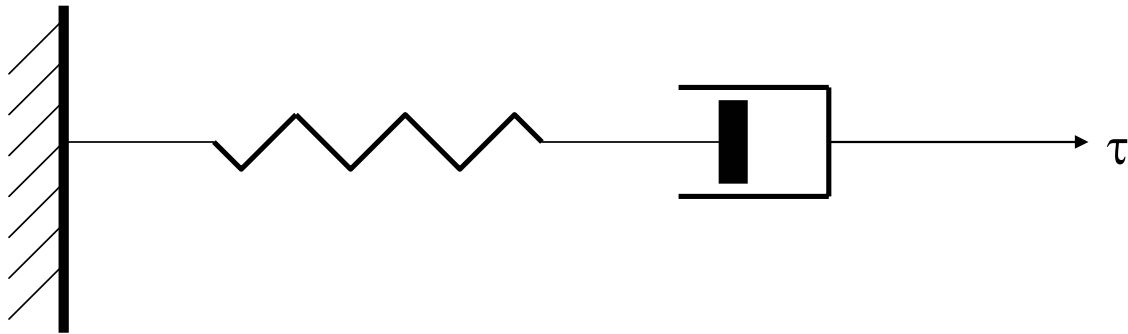


Figure II.15 Maxwell model with spring and dashpot

Consider Equation II.16 now in terms of varying with respect to time and we get the following equation:

$$G(t) = \frac{\tau(t)}{\gamma} \quad \text{II.36}$$

Here, ' t ' is time and ' $G(t)$ ' is the relaxation modulus.

It has been seen that in viscoelastic systems that the retraction of an applied load results in the decay of the relaxation modulus until it ultimately saturates to a constant value. This is referred to as linear viscoelasticity and is typically seen in systems where the shear strain rate is relatively small. Alternately a system can exhibit nonlinear viscoelasticity by not decaying directly towards recovery³⁸. See Figure II.16.

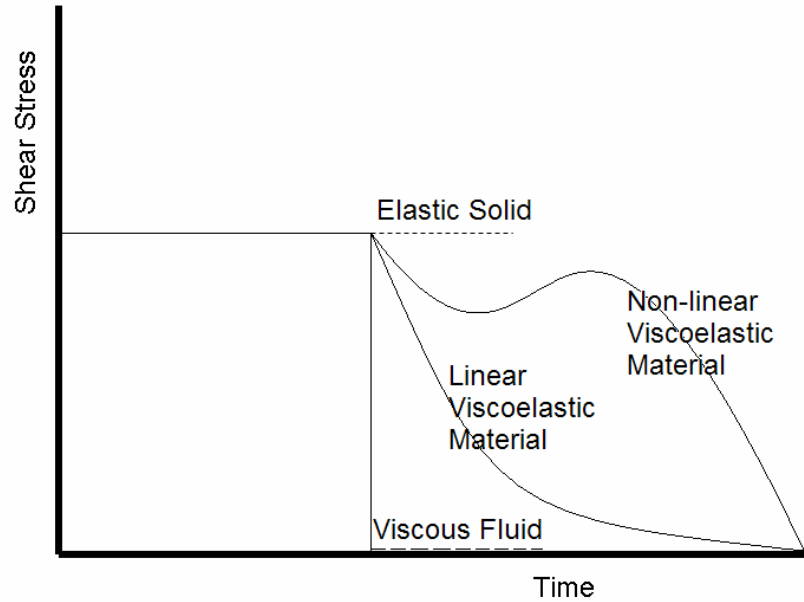


Figure II.16 Linear and non-linear viscoelasticity as distinguished from viscous fluid-like behavior and elastic solid-like behavior

Typical viscoelastic characterization is made through knowledge of the Deborah number. The Deborah number, ' De ', is demonstrated in the following equation³⁷:

$$De = \frac{\lambda}{t_f} \quad \text{II.37}$$

Here, ' λ ' is the relaxation time of the fluid

' t_f ' is the characteristic time of the flow test. This can also be viewed as the reciprocal of the typical shear strain rate $\dot{\gamma}^{-1}$. The nature of the system is assessed by the value of $\log(De)$. For $\log(De) < 0$, the system is said to be liquid-like. Conversely, for $\log(De) > 0$, the system is said to be solid-like.

Another time-based scenario is a pulsed oscillatory shear stress or strain introduced into the system. Typically, if a sinusoidal oscillatory deformation is applied to the system, the strain resulting can be described via the following equation:

$$\gamma = \gamma_0 \sin(\omega t) \quad \text{II.38}$$

Here, ' γ_0 ' is the amplitude of the strain pulse, ' ω ' is the frequency of the oscillation and ' t ' is the time. In order to qualify as a viscoelastic system, the applied oscillatory stress wave cannot always be in phase with the strain wave by definition. Typically, as per convention, it is noted that the shear stress pulse is out of phase by a quantity, ' δ ', prompting the following equation

$$\tau = \tau_0 \sin(\omega t + \delta) \quad \text{II.39}$$

Here ' τ_0 ' is the amplitude of the stress wave. In order to present this equation in similar terms to Equation II.38 we use the following transformation:

$$\sin(a + b) = \sin(a)\cos(b) + \cos(a)\sin(b) \quad \text{II.40}$$

Using this manipulation on Equation II.39 allows the shear wave to be expressed as:

$$\tau = \tau_0 \sin(\omega t) \cos(\delta) + \tau_0 \cos(\omega t) \sin(\delta) \quad \text{II.41}$$

The terms ' $\tau_0 \cos(\delta)$ ' and ' $\tau_0 \sin(\delta)$ ' can be respectively manipulated into ' τ_0 ' and ' τ_0'' ' making the shear wave:

$$\tau = \tau_0' \sin(\omega t) + \tau_0'' \cos(\omega t) \quad \text{II.42}$$

If we regard Equation II.42 as the superpositioning of two waves, it can be argued that two different variables exist, depending on the nature of the system as a function of the applied frequency, time or even shear stress pulse. When ' δ ' is near zero, the strain

wave as a function of these variables is in phase with the stress wave. When ' δ ' is close to $\pi/2$ radians, the stress wave is out of phase with the strain wave and as such the deformation results in large strains in the system. To describe the scenario, two moduli can be derived from the two different stress wave amplitudes in relation to the strain wave amplitude³⁸.

$$G' = \frac{\tau_0'}{\gamma_0} \quad \text{II.43}$$

$$G'' = \frac{\tau_0''}{\gamma_0} \quad \text{II.44}$$

As such, G' is referred to as the in-phase or elastic modulus. Indeed, it is analogous to the elastic modulus of a solid material because the more in-phase relationship of the stress and strain waves represents the maintenance of the relative structure of a fluid suspension. The counterpart variable, G'' , represents a scenario where the strains are out of phase with the applied stress. Moreover, Macosko contends that when plotted simultaneously, τ_0'' is in fact in phase with the strain rate wave suggesting this modulus is related to the viscous flow properties of a viscoelastic suspension.

II.6.3 Aggregate Network Model

II.6.3.1 Rheology of suspensions of spherical particles

Initial investigations by Einstein speculated on the change in viscosity of a suspension of rigid particles as a function of the change in solids volume fraction. However, as Mooney has indicated, the Einstein equation was ignorant of solid-solid

interactions because of the low concentration of solute. Krieger and Dougherty⁴⁸ contend that for low solids concentrations, the relative viscosity, ' η_r ', can be described as:

$$\eta_r = 1 + [\eta]\phi \quad \text{II.45}$$

Here, ' $[\eta]$ ' is the 'intrinsic viscosity, while ' ϕ ' is the volume fraction of particles. For higher concentrations, Mooney⁴⁹ postulated the following equation for monosized spheres:

$$\eta_r = \exp\left(\frac{2.5\phi}{1 - k\phi}\right) \quad \text{II.46}$$

Here, ' k ' is a constant known as the self-crowding factor. Since the exponential relationship allows for additive properties, Mooney further adds that for a bimodal system (i.e. a system of particles of two sizes, ' r_1 ' and ' r_2 ' with volume fractions ' ϕ_1 ' and ' ϕ_2 ' respectively), the relative viscosity can be given by:

$$\eta_r = \exp\left(\frac{2.5(\phi_1 + \phi_2)}{1 - k(\phi_1 + \phi_2)}\right) \quad \text{II.47}$$

Krieger and Dougherty⁴⁸ connect the empirical flow models with solids fraction dependency by indicating that non-Newtonian behavior can occur in particle suspensions that begin exhibiting sufficiently high volume fractions of suspended particles, leading them to suggest that the root cause of deviation from Newtonian behavior is interparticle interactions. In their study, they argue that for particle collisions forming doublets, the rate of aggregation can be viewed as a chemical reaction with associated rate constants. Bulk shear causes these doublets to rupture. Thermal vibrations due to Brownian motion cause the system to aggregate. These thermal vibrations are further associated with a diffusion constant, D , which is responsible for dissociation of the 'doublet' produced.

When considering boundary conditions of zero shear rate and infinite shear rate, they derive the following flow equation:

$$\frac{\eta - \eta_{\infty}}{\eta_0 - \eta_{\infty}} = \left(1 + \frac{|\tau|}{\tau_c}\right)^{-1} \quad \text{II.48}$$

Note the similarity to the terms in the Cross-Carreau model. Furthermore, ‘ τ ’ is the shear stress applied on the system while ‘ τ_c ’ is given by:

$$\tau_c = \frac{\alpha k T}{3a^2} \quad \text{II.49}$$

Here, ‘ α ’ is the constant of proportionality between the particle size, ‘ a ’, and the diffusion length. The authors cite analysis by Einstein of the shear field surrounding a particle which argues that this α is of the order of unity; ‘ k ’ is Boltzmann’s constant; ‘ T ’ is the absolute temperature^{48,50}.

Krieger and Dougherty fitted the theoretical equations to data acquired for suspensions of latex spheres. However, they and Mooney commonly were attempting to fit equations based on empirical results without fundamental insight into the structure of the system with incremental crowding.

II.6.3.2 Impulse Theory

One model presented for discussing the nature of a crowded aggregate system is the Impulse Theory put forth by Goodeve and later extended by Gillespie⁵¹. This model contends that the forces in such a system are comprised of two components: strictly hydrodynamic forces and interparticle interactions. These interactions can be additive and as such can be expressed mathematically as:

$$\tau = \tau_B + \eta\dot{\gamma} \quad \text{II.50}$$

The term ' $\eta\dot{\gamma}$ ' represents the hydrodynamic effects of shear in the system. The ' τ_B ' term is referred to as the Goodeve stress. It is dependent on both time and shear stress. Note the similarity to Equation II.32 of a Bingham plastic body. Goodeve contends that the term is representative of the stress required to disrupt a networked gel-like structure where aggregated units link to each other like chains spanning the entire fluid medium. Shearing the system initially causes stretching of the 'links' before higher stresses eventually result in their rupture. Cessation of shearing is believed to result in a reformation of these links. Goodeve further describes the term in the following equation:

$$\tau_B = \left(\frac{3\phi^2}{2\pi^2 a^3} \right) E_a \quad \text{II.51}$$

Here ' a ' is the particle radius; ' ϕ ' is the volume fraction of the dispersion; ' E_a ' is defined by:

$$E_a = \varepsilon_a * n_L \quad \text{II.52}$$

Here ' n_L ' is the number of links between particles; ' ε_a ' is the energy per link. It is possible therefore to begin to measure the link strength of particles in a network suspension. However, given the sensitivity of ' τ_B ' on the volume fraction, this energy will subsequently vary depending on the volume fraction of particles utilized⁵¹.

II.6.3.3 Dual Moduli

It has been conceded earlier in works by Krieger and Dougherty that non-Newtonian behavior will arise from suspensions of sufficiently high solid particulate

crowding. These arguments were put forth previously in suggesting that at sufficiently high fractions of a ‘dispersed’ (i.e. solid) phase a network structure is created.

The ideas of Goodeve and Gillespie are taken a step further by van dem Temple and Papenhuizen. They argue that for a system under constant stress, the shear strain will increase with time. They fit this particular behavior to the following equation⁵¹:

$$\gamma = \left(\frac{\tau}{G_1} \right) + \left(\frac{\tau}{G_2} \right) \log(t) \quad \text{II.53}$$

Their argument is that there are in fact two moduli ‘ G_1 ’ and ‘ G_2 ’ in the system. Additionally, the two moduli indicate the presence of two types of bonds: primary bonds, which serve as bonds between the individual particles (which they refer to as ‘crystal bridges’) and secondary bridges that are formed because of van der Waals forces. The latter are broken by forces and are subsequently reformed in a more relaxed position. This gives rise to a phenomenon they refer to as ‘retarded elastic behavior’⁵¹.

Furthermore, it is contended that aggregates are connected by van der Waals forces. The subunits that are linked to each other as constituents of the network are ‘agglomerates’ connected by chains. Each agglomerate unit is characterized as having a specific size, L . At a critical stretching force, the bonds break depending on the time afforded to the shearing process. Large deformations may result in reformation in the presence of compressive forces⁵¹.

II.6.3.4 Wu and Morbidielli’s Scaling Model

The relationship between aggregate properties and the ‘structure’ in fluids is further explored by Wu and Morbidielli³⁵. They corroborate the argument of the network model by arguing that the elastic properties of aggregates can be approximated as a linear

chain of springs. Furthermore, they contend that two regimes are possible, based on the differences between what they term 'interfloc' and 'intrafloc' strength. The interfloc strength (see Figure II.17a) is described above as the strength binding separate aggregate constituents in the network while the intrafloc strength is given as the strength of bonding of primary particles within the aggregated network constituent (see Figure II.17b). Given these distinctions, the 'strong-link' regime is where the intrafloc links are weaker than interfloc, and as such reflect the bulk macroscopic rheological measurements. Conversely, the 'weak-link' regime is where the interfloc links are weaker and are thus the reflection of bulk rheological measurements. Their arguments relate the bulk rheological properties obtained via techniques such as oscillation rheometry to aggregate properties via the following equations:

$$G' \propto \phi^A \quad \text{II.54}$$

$$\gamma_0 \propto \phi^B \quad \text{II.55}$$

Here, ' ϕ ' is the volume fraction of particulate and the terms A and B are given by:

$$A = \frac{d + x}{d - d_f} \quad \text{II.56}$$

$$B = -\frac{1 + x}{d - d_f} \quad \text{II.57}$$

Where ' d_f ' is the aforementioned fractal dimension of the aggregates, ' d ' is the Euclidean dimension of the system and ' x ' is the fractal dimension of the 'backbone'. These are the conventional scaling theories that Wu and Morbidelli build their own arguments from. In considering the effective elasticity of a network, they put forth their own scaling relationship of an aggregate of average size ' ξ ' given by³⁵:

$$\xi \propto \varphi^{\frac{1}{d_f-d}}$$

II.58

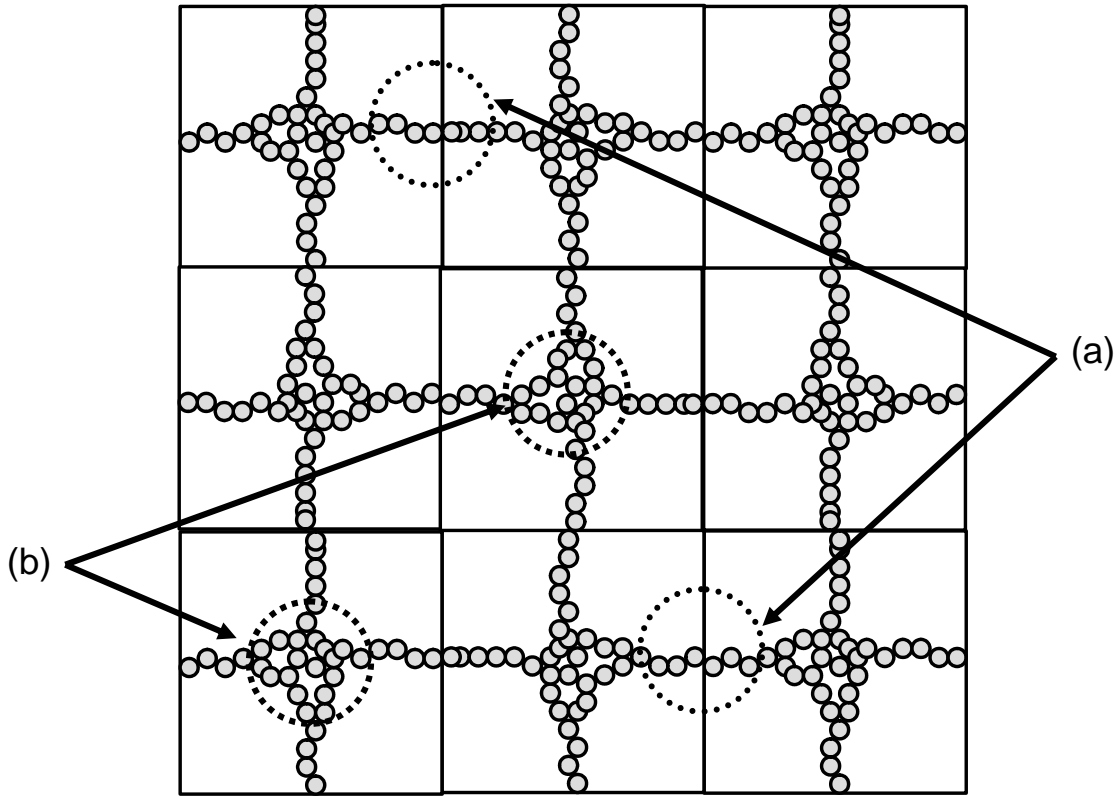


Figure II.17 The network model in conjunction with Wu and Morbidielli's concepts of (a) 'interfloc' bonding and (b) intrafloc bonding

This suggests that materials exhibiting more fractal surface characteristics (i.e. a higher fractal dimension) for a fixed solids concentration will exhibit a smaller average aggregate size. Building from the first scaling model presented, they suggest that the 'effective' elasticity of an aggregate in a network, ' K_{eff} ', is based the elasticity of the intrafloc elasticity, ' K_{ξ} ', and the interfloc elasticity, ' K_I ', via the following relationship:

$$\frac{1}{K_{eff}} = \frac{1}{K_{\xi}} + \frac{1}{K_I} \quad \text{II.59}$$

Since the measured effective elasticity will be controlled by the weaker of the two strengths, if one of the elasticities is significantly greater the other elasticity will be the value that is approximately equal to ' K_{eff} '. The effective elasticity of the aggregate can be

scaled again and is related to the size of the macroscopic gel, ‘ L ’, and the macroscopic gel’s elasticity, ‘ K ’ by:

$$\frac{L^{d-2}}{K} \propto \frac{\xi^{d-2}}{K_{eff}} \quad \text{II.60}$$

Substituting for K_{eff} yields:

$$K \propto \left(\frac{L}{\xi} \right)^{d-2} \left(\frac{K_{\xi}}{1 + \frac{K_{\xi}}{K_1}} \right) \quad \text{II.61}$$

Wu and Morbidielli use the following approximation:

$$\left(\frac{1}{1 + \frac{K_{\xi}}{K_1}} \right) \cong \left(\frac{K_1}{K_{\xi}} \right)^{\alpha} \quad \text{II.62}$$

Substituting this into the above equation yields:

$$K \propto \left(\frac{L}{\xi} \right)^{d-2} K_{\xi} \left(\frac{K_1}{K_{\xi}} \right)^{\alpha} \quad \text{II.63}$$

Here, ‘ α ’ is a unitless gel parameter between 0 and 1. These boundaries reflect whether the system is exhibiting a strong-link regime ($\alpha = 0$) or a weak-link regime ($\alpha = 1$). From here, further relations can be derived such as the number of springs (or what van de Ven and Hunter earlier described as the floc coordination number or what the Goodeve model describes as the number of ‘links’), ‘ N_s ’, in relation to the average aggregate size, ξ , and backbone fractal dimension, x :

$$N_s \propto \xi^x \quad \text{II.64}$$

II.6.4 Measurement

Measurement of viscosity has relied on several effects observed in viscous fluids. The most common method used typically is a rotating viscometer operating with controlled angular velocity, ' ω '. A cylindrical spindle of depth, ' L ', and radius, ' r_1 ', rotates within a cylindrical chamber of radius, ' r_2 '. Shear resistance of the fluid medium exerts a torque, ' T ', on the outer surface of the spindle. Via measurement of the torque, and use of calibrated spindles of specified ' r_1 ' and ' L ' values, viscometers often are used to compute the apparent viscosity via the following equation⁴⁰:

$$\eta_a = \frac{T}{\omega} \frac{r_2^2 - r_1^2}{r_1^2 r_2^2 4\pi L} \quad \text{II.65}$$

Another method is the use of Stokes' law to calculate the viscosity of a fluid medium. Stokes law is based on a particle of a size sufficiently large enough (or under sufficient gravitational or centrifugal force) to be unaffected by Brownian motion settling in a fluid medium under laminar flow. It is assumed by Stokes law that viscous drag of the fluid medium is sufficient to produce a near-instant terminal velocity such that the distance descended in the fluid over time is approximately linear. This is represented by the following equation⁴⁰:

$$\eta_a = \frac{a^2 (D_p - D_L) g t}{18H} \quad \text{II.66}$$

Here, ' a ' is the diameter of the powder particle, ' D_p ' is the density of the powder particle ' D_L ' is the density of the liquid medium, ' g ' is the acceleration due to gravity or centrifugation, ' t ' is the duration the particle has been settling in the fluid, ' H ' is the distance traveled by the particle and ' η_L ' is the viscosity of the fluid medium. This is referred to Macosko³⁸ as the falling ball viscometer. The ball can be substituted with

other geometries such as cylinders or plates. However, this has been criticized for unsteady shear at the edges of the geometry used. Alternately, a rolling ball is used with fiber optic sensors tracking the motion of the ball. The apparent viscosity is calculated as:

$$\eta_a = \frac{a^2 (D_P - D_L) g t \sin \theta}{4H} \quad \text{II.67}$$

Here, ' θ ' is the angle of incline. Other techniques utilized to measure viscosity include viscous damping of sonic probes, torsional resistances to rotation of a fixture or measurements of time to flow an orifice in a cup. All of these tests are predicated on variation of the shear rate.

For higher viscosity materials such as extrusion pastes where simple viscometry is insufficient to assess the system, Benbow⁴⁶ suggests that capillary rheometry can be utilized to assess the flow behavior. In capillary rheometry, a paste is forced via a piston ram through an orifice of specific diameter and length, as seen in Figure II.18.

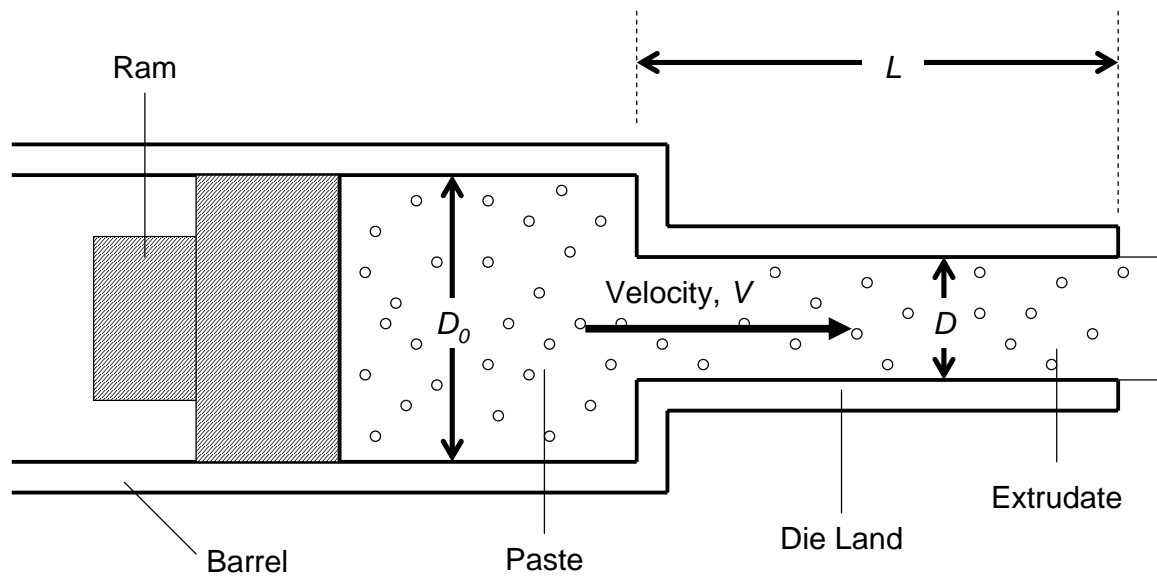


Figure II.18 A schematic of a capillary rheometry assembly (redrawn from [46])

Since fluid rheology can be extended to materials such as extrusion pastes, this technique is commonly used to rheologically evaluate the bulk properties of extrusion formulations. Benbow analytically computes that the overall pressure drop in the process of capillary rheometry can be given as the sum of pressure effects from two distinct processes. The first pressure drop, ' P_1 ', is the entry of the paste from the barrel into the die land, given by:

$$P_1 = 2\sigma \ln\left(\frac{D_0}{D}\right) \quad \text{II.68}$$

Here, ' D_0 ' and ' D ' are the diameters of the barrel and die respectively. The uniaxial yield stress is given as ' σ ', which can be further expanded as:

$$\sigma = \sigma_0 + \alpha V \quad \text{II.69}$$

Here ' σ_0 ' is the yield stress extrapolated to zero velocity, ' V ' is the extrusion velocity and ' α ' is a factor characterizing the velocity effect on pressure. Benbow contends that the ' αV ' term is analogous to the ' $\eta\dot{\gamma}$ ' term for a liquid in a shear flow and as such, analogous to the Bingham plastic described in Equation II.51. Substituting this term into Equation II.68 yields:

$$P_1 = 2(\sigma_0 + \alpha V) \ln\left(\frac{D_0}{D}\right) \quad \text{II.70}$$

The second pressure drop, ' P_2 ', is the pressure in the die land and is given by:

$$P_2 = 4\tau \ln\left(\frac{L}{D}\right) \quad \text{II.71}$$

Here, ' L ' is the die land length, ' D ' is the die diameter and ' τ ' is the paste yield stress extrapolated to $L/D = 0$ related to shearing effects at the wall of the die land. As with σ , τ can be modeled as a Bingham plastic body by:

$$\tau = \tau_0 + \beta V \quad \text{II.72}$$

Here, ' τ_0 ' is the wall shear stress extrapolated to zero velocity, ' V ' is the extrusion velocity while ' β ' is the velocity dependent factor of wall shear stress. Expanding the ' P_2 ' term by this relationship and combining P_1 and P_2 produces an equation for the overall pressure drop in the system, ' P ', as:

$$P = 2(\sigma_0 + \alpha V) \ln\left(\frac{D_0}{D}\right) + 4(\tau_0 + \beta V) \left(\frac{L}{D}\right) \quad \text{II.73}$$

Benbow⁴⁶ recognizes the assumptions of Bingham behavior and includes terms to accommodate the general Herschel-Bulkley model by modifying the equations as:

$$P = 2(\sigma_0 + \alpha V^m) \ln\left(\frac{D_0}{D}\right) + 4(\tau_0 + \beta V^n) \left(\frac{L}{D}\right) \quad \text{II.74}$$

The aim of capillary rheometry is characterization of the pastes via determination of the values α , β , σ_0 , τ_0 . This is typically carried out by monitoring the barrel pressure via a transducer and the use of multiple extrusion velocities with many different dies to obtain a variation of the L/D term.

It should be recognized that Equation II.73 is derived based on circular dies. The equations are summarily generalized by Benbow for flow from circular cylinders into a square entry die land by:

$$P = 2 \ln\left(\frac{D_0}{D}\right) f(V) + 4 \left(\frac{L}{D}\right) g(V) \quad \text{II.75}$$

Here, ' $f(V)$ ' and ' $g(V)$ ' are the terms used to characterize the paste; the former is related to the change in the cross-sectional area of the paste due to extension in the die entry and $g(V)$ is a parameter detailing the shear flow of the paste along the die land.

II.6.5 Role of Soluble Ionic Species

The work documented above focuses largely on bulk hydrodynamic and shearing effects on the rheology of a ceramic particulate suspension. However, of significant concern beyond these are surface considerations which can largely affect the properties of the free-flowing hydrodynamic unit.

Lange⁵² further adds to the discussion by arguing that the equilibrium separation distance, ' h ', between two particles is analogous to the equilibrium separation of springs. Note the agreement with the aforementioned Maxwell model for elasticity of bodies. In particular, Lange argues that the second derivative of the equilibrium curve with respect to h yields the 'spring constant' of the elastic component, and can be subsequently related to G' . Lange further contends that for a fixed interparticulate potential, elastic moduli and yield stress will increase as a function of the volume fraction with exponents from 3.5-4.5 (in contrast with Equation II.51 which argues this exponent should be 2). Lange's overall approach was to contrast this theory with pressing techniques to observe a brittle to plastic transition in via stress-strain curves and varying the amount NH_4Cl to affect the flowability of the material.

Another investigation is provided by Rand et al.⁵³ Their investigation incorporated earlier arguments from Krieger and Dougherty on the role of solid particulate fraction on the rheology of a suspension and coupled this with the role of soluble ions in suspension in forming 'soft particles'. While earlier aforementioned sources effectively illustrate a network model, Rand et al. argue that this network need not be created by solid particle-particle contacts as the network model earlier would suggest. Rather, their contention is that the network is formed due to particle crowding

resulting in electrical double layer overlap. Their efforts were concentrated on adding KCl in varying molar concentrations to a suspension on nanosized alumina such that the KCl added served as an indifferent electrolyte in the system. Indifferent electrolytes are components of the solution which do not chemically interact with the surface of the particles yet contribute to the overall ionic strength of the suspension.

Rand et al. argue that increasing the ionic strength via the indifferent electrolyte decreases the size of the electrical double layer formed about the surface of the particle. The effective particle is, therefore, smaller, which affects the elasticity imparted to the suspension, specifically via characterization of G' , the so-called elastic component of viscoelastic measurements. Rand et al. argue that the number of attractive links in the network above the critical coagulation concentration is reduced as the overall interaction potential is reduced. This further suggests that the elasticity of a suspension as a bulk characterization is highly dependent on the proximity of the individual particles to one another.

II.6.6 Effect of Temperature

Viscous flow can be viewed as a kinetic phenomenon and is classified typically as exhibiting inverse Arrhenius behavior. Per such, viscosity's relationship with temperature is often represented by the Andrade-Eyring equation:

$$\eta_L = A \exp\left(\frac{Q}{RT}\right) \quad \text{II.76}$$

Here, ' A ' is a pre-exponential term; ' Q ' is the kinetic barrier or activation energy for viscous flow; ' R ' is the gas constant and ' T ' is the absolute temperature. Macosko

contends this equation is based on the hypothesis that small molecules move by jumping into unoccupied holes³⁸.

II.7 Tape Casting

II.7.1 History and Schematic

Tape casting (or doctor blading or knife coating as it is alternately referred to) is a common ceramic green fabrication technique utilized to prepare thin flexible sheets of material. The process originates in the paint industries who sought a means of testing the covering ability of their formulations. The technique was adopted by Glen Howatt, who attempted to fabricate a capacitor material whose structure mimicked the natural ‘platy’ structure of mica while providing its high dielectric strength and low dielectric loss. Motivated by shortages of mica caused by the Second World War, he developed an apparatus at Fort Monmouth in Eatontown, NJ for ‘thin sheet extrusion’ of capacitor materials (indeed the instrument appeared in fact to be modified from the design of an extruder). This is widely believed to be prototype for the modern tape caster^{54,55}.

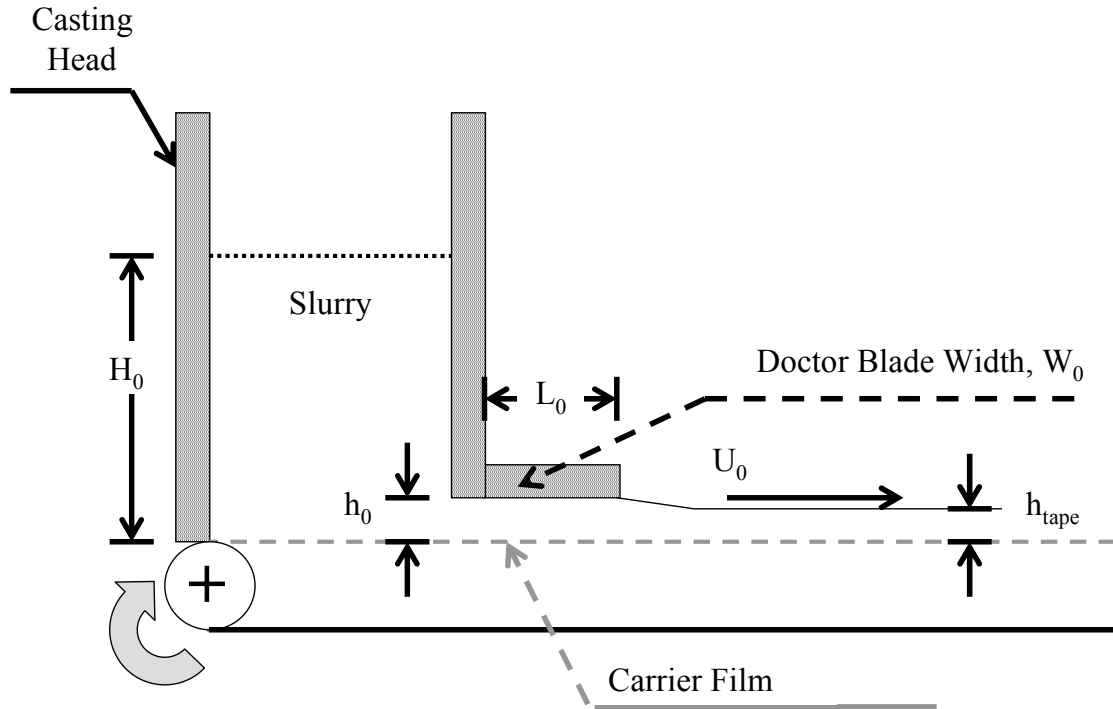


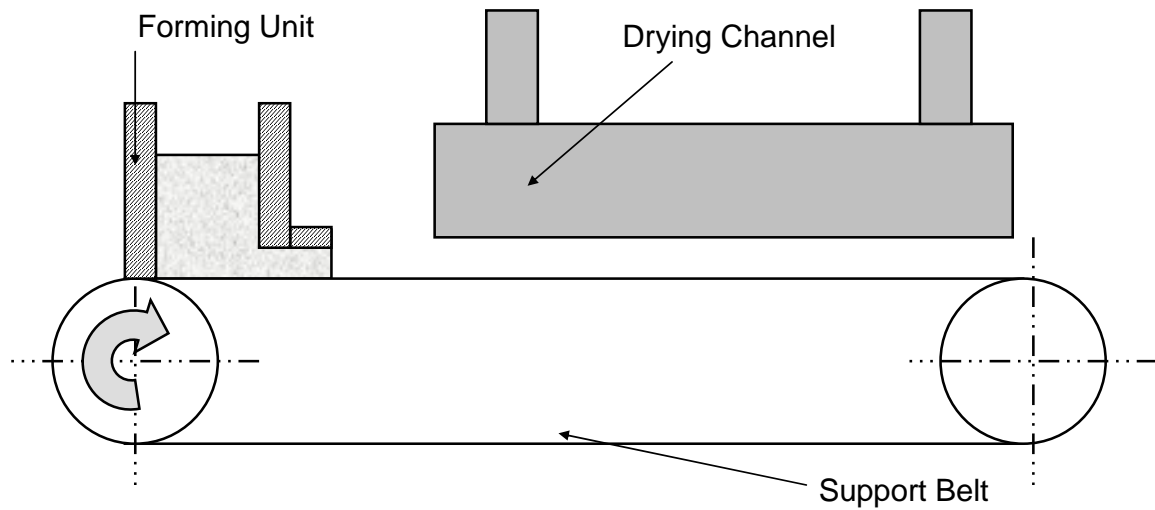
Figure II.19 Schematic of a tape casting process; Slurry height, H_0 , tape thickness, h_{tape} , doctor blade thickness, h_0 , doctor blade length, L_0 , doctor blade width, W_0 , casting velocity, U_0 .

A typical tape casting operation involves the motion of a carrier film relative to a stationary doctor blade, prescribed for the desired green thickness of the part. A reservoir placed behind the doctor blade houses the ‘slip’ which is cast via motion of the carrier film. Typical thicknesses sought in manufacturing range from millimeter to single-digit micron thicknesses. The relatively large aspect ratio of the tape’s x-y direction (casting direction and width) to the z-direction (thickness) often imparts flexibility when utilized with a corresponding carrier. The carrier typically in fabrication of ceramic devices has been a nonabsorptive polymer (commonly silicon-coated Mylar is used). This allows for continuous production. Typical manufacturing proceeds in three stages⁵⁴:

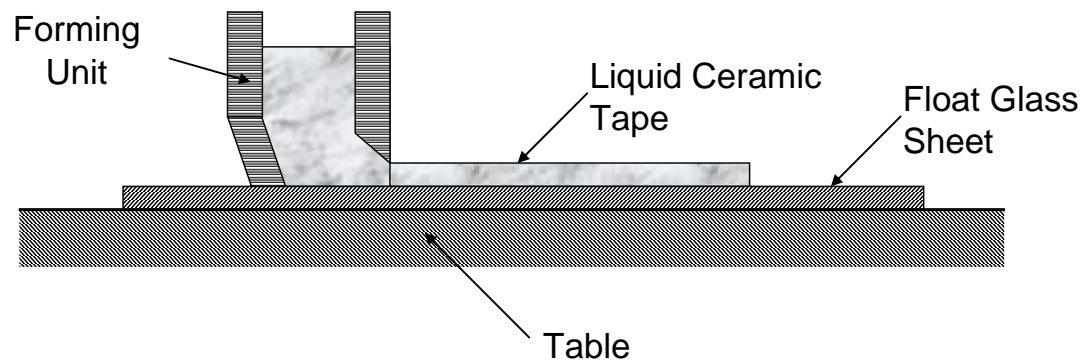
1. Forming of a liquid ceramic sheet on a support belt or glass sheet
2. Drying of the wet sheet
3. Removal of the dry sheet

A schematic of the most basic tape casting apparatus is presented in Figure II.19.

Variations on this design are shown in Figure II.20^{24,56}.



(a) Doctor-blade casting



(b) Batch casting

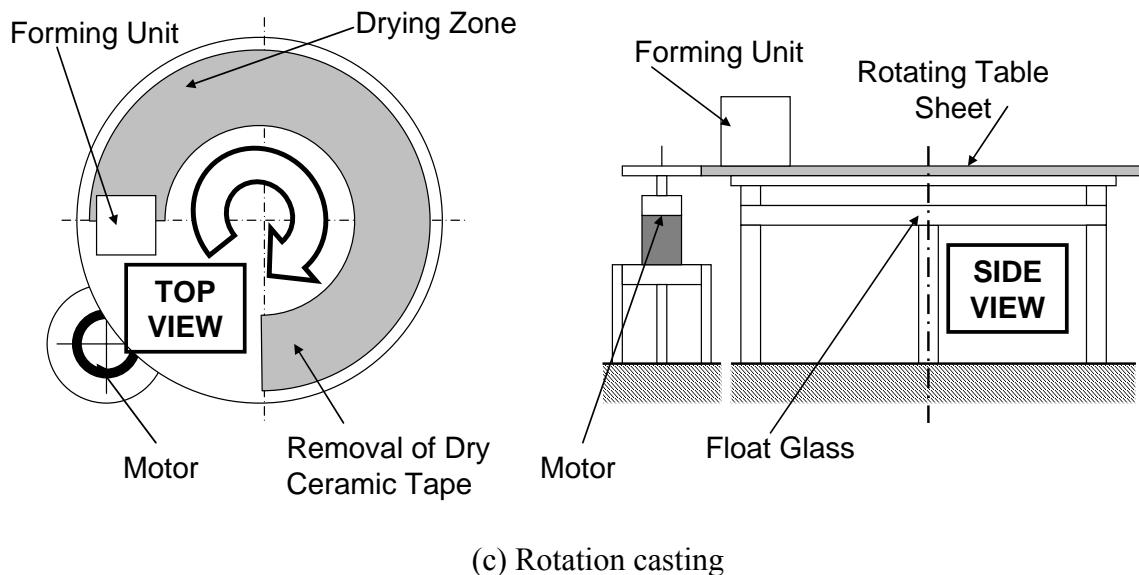


Figure II.20 The varying configurations for tape casting (a) Doctor-blade casting (b) Batch casting (c) Rotation casting (redrawn from [56])

After casting, components are typically stacked in layers and then sintered to form the final product.

II.7.2 Slip composition and Materials Considerations

Like slip casting, tape casting typically requires the use of a low viscosity suspension. Rheological concerns involve the presence of agglomerates to impart bulk yield shear strength to the suspension. As such typical tape casting procedures involve milling to reduce the presence of agglomerates. Moreover, compositional considerations may include the presence of a binder to further impart flexibility in the green body as well as providing rigidity and contiguity for the part prior to sintering. Additional components of the slip may include wetting aids and dispersants to promote wetting of the carrier film and lowering the viscosity respectively⁵⁴.

The solvent used to create the slip commonly is water. Other organic solvents such as Methyl Ethyl Ketone (MEK) or 1,1,2 methyl pyrrolidinone can be utilized

because of the increased drying rate they afford. Mistler argues that the choice of solvent is inherently rooted in production rate as well as the ability to dissolve the additional batch components listed above⁵⁴.

Additional processes employed to optimize the slip may include de-airing via a low vacuum at pressures of 635-700 mm Hg to eliminate the presence of gas bubbles within the slip which would otherwise produce pinholes and subsequent 'crow's feet' cracking⁵⁴.

II.7.3 Fluid Flow and Texturing of Slurries during Tape Casting

Particulate considerations become relevant in tape casting typically when anisotropic particles are utilized. The nature of the process' uniaxial flow direction coupled with particle mobility in the slip results typically in a phenomenon known as texturing, or preferred orientation, occurring. An understanding of fluid flow under the various parameters offered in tape casting is essential regarding slurries where texturing is essential to optimizing properties that involve particulate and grain orientation. This is preferable to the alternative of using pressure during sintering to align grains. Furthermore, it is established by Watanabe et al.⁵⁷ that increased orientation of particles in a green body results in greater grain orientation in a sintered product. Additionally, complications due to formation of menisci upon exiting the doctor blade channel result in deviation in the height of the tape from the doctor blade thickness. Fluid flow studies described below have attempted to resolve this discrepancy.

Studies initiated by Chou et al.⁵⁸ attempted to use fluid dynamics models to predict the effect of variables such as viscosity, casting velocity and casting head

geometry. However, of critical note in the analysis by Chou et al. is the assumption of Newtonian behavior and, subsequently, Couette flow for the casting slurry. Chou's results found what they determined to be a reasonable agreement between the predicted thickness of the tape and experimental results of casting a 50 weight% suspension of CaTiO_3 with a 402 μm doctor blade thickness.

Pitchumani et al.⁴⁴ took the efforts of Chou et al. a step further by considering the casting of an Ostwald-de Waele fluid. In consideration of a tape casting assembly, Pitchumani uses a value, α , given by:

$$\alpha = \frac{\text{Re}}{\text{Fr}} \left(\frac{h_0}{L_0} \right) \quad \text{II.77}$$

Here, 'Re' is the Reynolds number of the slurry, defined earlier, ' h_0 ' is the doctor blade height, ' L_0 ' is the length of the doctor blade channel and ' Fr ' is the Froude number, which is given by:

$$\text{Fr} = \frac{U_0^2}{gH_0} \quad \text{II.78}$$

Here, ' U_0 ' is the velocity of the substrate, ' H_0 ' is the height of the slurry in the reservoir and ' g ' is the gravitational acceleration. The Froude number is described as being indicative of hydrostatic head effects in the slurry due to the height of the reservoir. The value, ' α ', appears to serve as a demarcation between two types of flow behavior. In Case I, for low values of this term, there is a low pressure gradient relative to the drag effects of the moving substrate. Conversely higher values result in the opposite scenario Case II. Flow profiles for either case are suggested by Pitchumani et al. and illustrated as Figure II.21.

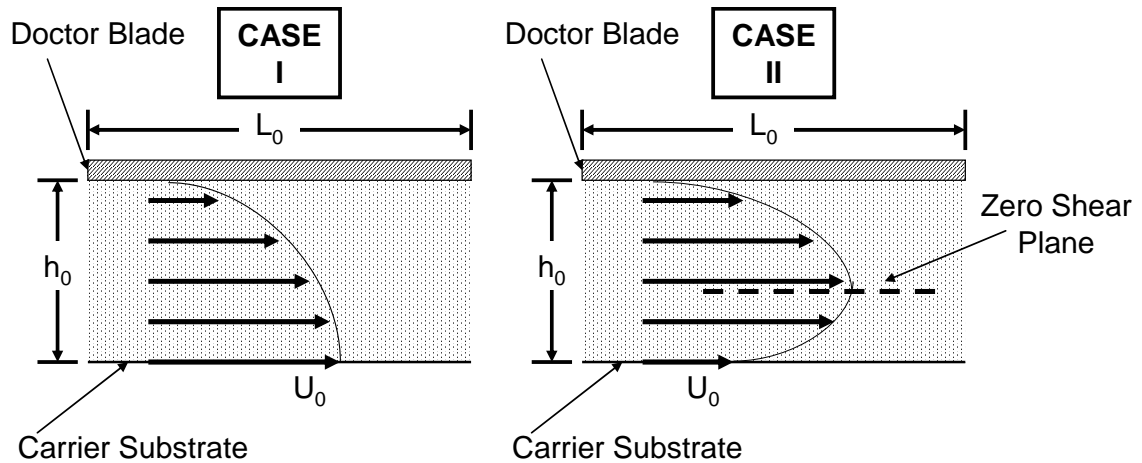


Figure II.21 Illustration of the two scenarios of Pitchumani⁴⁴ in the doctor blade channel

Their results seem to maintain that a more uniform thickness is attained for lower values of α (i.e., for Case I). Additionally, given the absence of non-Newtonian effects below a certain observed α value, it is suggested that the use of this parameter can serve as an auxiliary technique to evaluate the rheology of the suspension. The overall suggestion of their work is the favorability of Case I as opposed to Case II due to the zero shear plane found in the latter resulting in uneven particle packing and thickness gradients⁴⁴.

Another study performed by Loest et al.⁵⁶ attempted to use Finite Element Modeling (FEM) to predict the flow behavior of an α -alumina suspension. The model was carried out on slurries that were assumed to obey Bingham plastic behavior.

Alternately, Schmidt et al.⁵⁹ attempted to use laser Doppler effects to investigate the local flow effects in the slurry. Their technique employed spatial and temporal resolutions of 24 μm and 5 μs respectively. Their measured velocity profiles as a function of tape thickness show how for a variety of casting velocities, a transition between Pitchumani and Karbhari's Case I and Case II can almost be measured experimentally. This system, however, utilized highly simplistic models for fluid flow

providing planar Couette flow contributions from drag flow of the substrate and a Poiseuille pressure flow analogue as the two extremes when considering the dominance of pressure-driven flow from the reservoir.

Watanabe et al.⁵⁷ studied texture produced in tape casting of plate-like bismuth titanate suspensions as a function of rheology, particle content and velocity gradient. They used similar assumptions of Newtonian behavior in tape casting since their computed Reynolds number was very low (4×10^{-2}) meaning that the fluid flow under the doctor blade was laminar. Their results concluded that the shear stress above a critical velocity gradient did not result in greater particle orientation. Moreover, their results indicated that while casting resulted in orientation due to minimizing flow resistance, increasing solids content resulted in mutual parallelism of particles, suggesting that the increased viscosity did not impede particle alignment.

Raj and Cannon⁶⁰ take this a step further in assessing alumina by assessing sintered shrinkage in the x-y plane (Watanabe's work is argued by Raj to concern itself with particle alignment in the x-z plane) of A-16SG alumina. The origin of the shrinkage anisotropy, they contend, is in the greater amount of particle-particle contacts in the transverse direction due to texturing of the particles. Their work appeared to confirm Watanabe's results by showing a greater amount of anisotropic shrinkage in systems of higher solids loading, as well as greater shearing conditions created by faster casting velocities and smaller doctor blade gaps. An interesting auxiliary argument to their work contended that agglomeration reduced the amount of anisotropy suggesting that either the agglomeration resulted in a less anisotropic flowing unit or that aggregate breakdown and particle alignment were competitive processes under shear.

Additional investigation came from Patwardhan et al.⁶¹. They contend that beyond a certain threshold of shear strain rate, the degree of anisotropic shrinkage is fairly constant. Furthermore, there is additional corroboration of Watanabe's argument of increasing orientation with increasing solids, as evidenced by anisotropic shrinkage yet the authors contend that this increase is small over a broad solids range (35-56 vol. %) for their system of study. Greater shrinkage is seen in the z-direction than the others yet the authors contend that this is more related to the distribution of binder normal to the z-plane than to anisotropy.

Commonly, many of the investigations described above use an extended doctor blade, resulting in creation of a rectangular 'channel'. However, as Kim et al.⁶² point out, doctor blade configuration may also include beveled surfaces which further complicate the fluid flow, as seen in Figure II.22. Kim et al. offer their own contribution to this discussion by introducing a term, ' Π ', serving as the ratio of pressure forces to viscous forces and given by:

$$\Pi = \frac{\Delta P H_1^2}{2\eta L_0 U_0} \quad \text{II.79}$$

Here, ' ΔP ' is the pressure flow gradient, ' H_1 ' is the doctor blade channel height upon exit from the reservoir, ' η ' is the slurry viscosity, ' L_0 ' is the length of the doctor blade channel parallel to the casting direction and ' U_0 ' is the aforementioned casting velocity. In comparison with aforementioned scenarios, $\Pi=0$ is the planar Couette flow profile as seen in Figure II.12a); $\Pi=1$ is comparable to Pitchumani and Kharbari's Case I. For instances of $1 < \Pi < 3$, the velocity profile is similar to Pitchumani and Kharbari's Case II. However, for $\Pi > 3$, the profile of Case II is further exacerbated; moreover, their

indication is that with increasing values of Π , the wet tape thickness begins to approach the doctor blade thickness and eventually equals the blade gap at $\Pi=3$ and ultimately surpasses this thickness for $\Pi > 3$ ⁶².

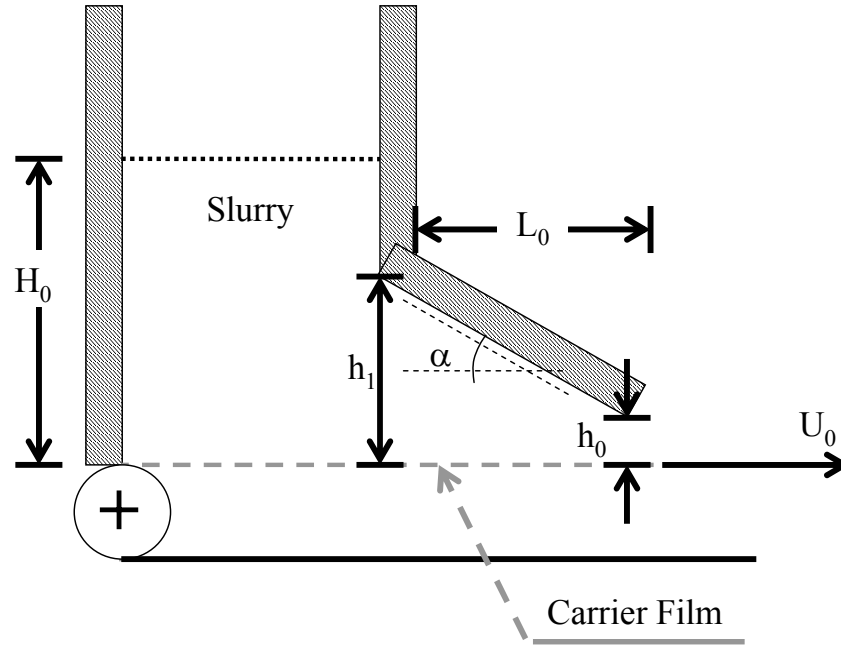


Figure II.22 Schematic of tape casting apparatus with a beveled doctor blade

For beveled surfaces, Kim et al.⁶² introduce a series of variables based on the position of the tape relative to various points in the assembly. The wet tape to doctor blade thickness ratio, ' ε_{wt} ', can then be expressed as:

$$\varepsilon_{wt} = \left(\frac{1}{\chi + 1} \right) \left(1 + \frac{\chi \Pi}{3} \right) \quad \text{II.80}$$

Where, ' χ ' is given by:

$$\chi = \frac{h_0}{h_1} \quad \text{II.81}$$

Note that substitution of $\Pi = 3$ yields $\varepsilon_{wt} = 1$ regardless of χ . Their findings showed that this term allows for consideration of pressure and viscous flows with pressure flows for beveled surfaces also accounting for hydrostatic pressure from the

slurry head and fluid flow in the channel. The relationship provided between ε_{wt} and χ appears to indicate that for various values of Π , ε_{wt} approaches unity as χ approaches 0. The increased pressure under the blade for beveled surfaces is believed to be undesirable when attempting to deliberately orient particles in a green body because of the creation of the aforementioned zero-shear plane⁶².

Another study carried out by Nycz⁴¹ sought to investigate the effects of texture in ‘platy’ anisometric alumina particles using an polarized light optical microscopy technique. Additionally, rheological studies were manipulated into Finite Element Modeling simulations of shear profiles to determine the regions of study for particle orientation effects. The study found that upon input of fit parameters, simulations indicated a strong concentration of shear at the doctor blade tip for a power-law input rheological model. This is in stark contrast to the linear Couette flow shear gradient with respect to the height of the tape that had been commonly used. The simulations of Nycz also indicated that the shear profile extended into the reservoir of the tape as well.

Moreover, the variation in shear profiles between the top and bottom surfaces is reflected in the degree of texture measured between these two surfaces of the tape. Nycz further measured the elastic modulus as an indication of texture variation due to anisotropy in the alpha alumina phase being reflected in varying elastic moduli along different axes. A greater degree of texturing in the c-axis would, therefore, reflect an increase in the elastic modulus in the through-thickness direction. This technique is corroborated by other texture dependent properties such as dielectric properties⁴¹.

II.8 Powder Compaction

II.8.1 Overview of Compaction Processes

Powder compaction is a widely utilized green forming technique in the ceramic (and many other) industries for mass production of products. The technique utilizes either a rigid die or a flexible mold in order to fabricate the shape desired with controlled dimensions. In industrial-scale production, because of the need for a high production output, feedstock powders are typically granulated for optimum flowability (typically via spray drying) such that die fill times are minimized and die fill is uniform. McEntire⁶³ argues that for a die pressing procedure, depending on the size and complexity of the part sought, pressing can yield production rates of up to several hundred parts per minute.

II.8.1.1 Dry Pressing

Dry pressing involves the use of a rigid metal die and a punch (see Figure II.23) resulting in a uniaxial compaction. Die pressing is described by McEntire as being a 3-stage process:

- Die Fill
- Compaction
- Ejection

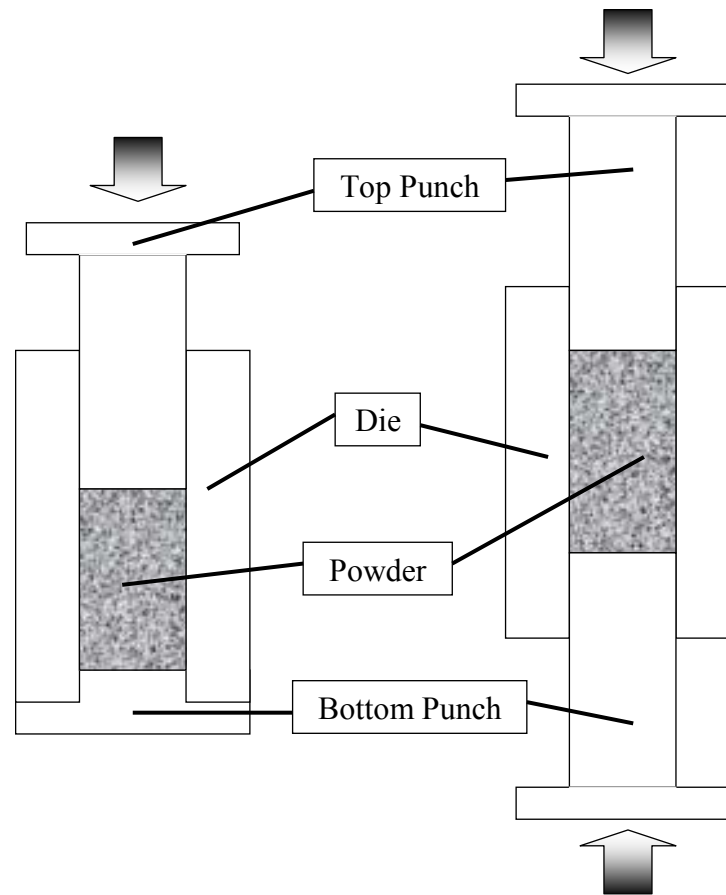


Figure II.23 Illustration of configurations for single action (left) and dual action punch (right) in die pressing. Arrows indicate pressing action direction.

The two major components of a die pressing technique are the die, into which the powder feedstock is loaded and the punch which performs the act of compaction. Compaction via die pressing can be either single action or a dual action. In the case of the former, the powder typically is loaded onto a stationary bottom punch while the top punch performs compaction. For dual action pressing, both the top and bottom punches are mobile. Dies and punches are typically made of hardened steel; depending on the wear of the desired application, these are substituted with specialized steel and carbide inserts^{63,64}.

Die pressing is typically performed with maximum pressures of 20-100 MPa. The process of die pressing has been sufficiently automated and crafted to ensure such reproducibility that industrial advertised tolerances are <1% variability in mass and ± 0.02 mm thickness. To facilitate ejection from the die, the die wall can be tapered by no more than $10\mu\text{m}/\text{cm}$. Typically, the pressing feedstock material is prepared as coarse spherical granules (according to Reed, typically with a size greater than $20\mu\text{m}$) with a smooth surface. This promotes a good flow rate which provides convenience for high production rates because of the low die fill time^{64,65}.

One pressing additive is a lubricant. Lubricants are defined as an interfacial phase that reduces the resistance to sliding between particles. These can exist in the form of low viscosity films between particles, adsorbed boundary films or solid particles with a laminar structure. A lubricant can be added to the feedstock slurry prior to spray drying or to the exterior surface of the resulting granules, leading to their classification as internal and external lubricants respectively. Balasubranian et al.⁶⁶ conducted a study on die pressing and found the use of an internal lubricant to effectively reduce the porosity when evaluating bodies at a fixed compaction pressure.

Binder is a necessary addition to a feedstock slurry in order to provide a polymer backbone structure to improve the green strength of the pressed part. In order for a binder to provide suitable flexibility to the green body, a low glass transition temperature (T_g) is typically desired. Often a plasticizer is added specifically to lower this T_g by reducing the van der Waals forces between the binder molecules. Plasticizer, like lubricants, can be applied internally or externally⁶⁷.

Compacts are typically assessed by a term known as the compaction ratio, 'CR'.

The CR is computed as:

$$CR = \frac{V_{fill}}{V_{pressed}} = \frac{D_{pressed}}{D_{fill}} \quad \text{II.82}$$

Here, ' V_{fill} ' and ' $V_{pressed}$ ' are the volumes of the filled die prior to pressing and the pressed part respectively; ' D_{fill} ' and ' $D_{pressed}$ ' are the corresponding densities. Typically for ceramic powders, powder consolidation results in pressed density that is below the maximum packing fraction of the particles because of high interparticle friction inhibiting sliding and optimal configuration. Typically in ceramics, a $CR < 2.0$ is desired. This is typically attained by a high fill density. Brittle ceramic particulate of high elasticity typically prevent this ratio from being higher. For pressing of ductile powders, usually a compaction ratio significantly greater than 2.0 is achieved⁶⁴.

DiMilia and Reed⁶⁸ conducted a study on the effects of wall friction on spray-dried alumina granules. They utilized a compaction procedure whereupon the applied stress was monitored simultaneously by a top load cell (recording the load imparted overall by the frame) and a bottom load cell recording the stress transmitted through the compact. This is shown in Figure II.24. Strain gauges were utilized to monitor the radial stress produced and studies were conducted with and without the use of an external stearic acid lubricant. Their results showed two major findings. Firstly, at greater strain rates (i.e. at greater strain rates), the use of stearic acid as a lubricant lowered the overall frictional effects as measured by the term $\mu_w K''$, where μ_w is the coefficient of wall friction and K'' is given by:

$$K'' = \frac{\bar{\sigma}_w}{\sigma_a} \quad \text{II.83}$$

Here, ' $\bar{\sigma}_w$ ' is the average wall stress and ' $\bar{\sigma}_a$ ' is the applied stress measured from the top load cell.

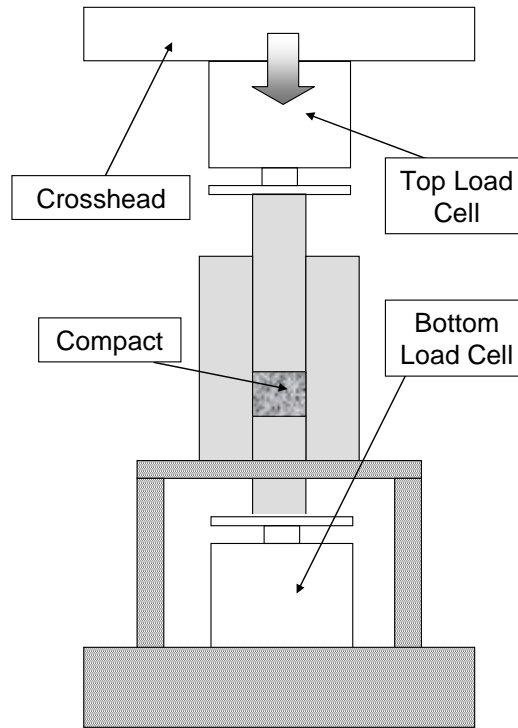


Figure II.24 Schematic of Reed and DiMilia's setup for measuring stress transmission (redrawn from [68])

Secondly, the wall stress plays a key factor in the transmission of stress to the compact. For pressed parts in unlubricated dies vs. lubricated dies, the ratio of the stress recorded in the bottom load cell to the stress recorded in the top load cell was lower overall, suggesting that the use of merely an external lubricant assures a greater transmission of the applied stress into the compact. It should be noted, however, that for parts of lower aspect ratio (i.e. the ratio of the height of the compact to its diameter), in both lubricated and unlubricated dies, the ratio of bottom to top load cell stresses approached 1 at the same aspect ratio. This suggests below a critical aspect ratio, the role of a lubricant is insignificant. Furthermore, it also suggests that the thickness of the pressed compact itself plays a role in stress transmission⁶⁸.

II.8.1.2 Isostatic Pressing

Die pressing as a production technique has limited possibilities for geometries producible based on the die utilized as well as the uniaxial pressing direction. These limitations are partly overcome through the use of a second pressing technique, isostatic pressing, which utilizes a flexible elastomeric mold instead of rigid metallic dies. Isostatic pressing is believed to overcome the issue of density gradients in the pressed part which typically plagues die-pressed parts because the elastomeric mold is believed to mitigate the wall friction effects⁶⁴. However, this has come under some scrutiny as Glass et al contend that there have been measured density gradients in isostatically pressed pieces leading to their suggestion that interparticle forces also play a significant role in producing density gradients⁶⁹.

Isostatic pressing is typically divided into two types, wet bag and dry bag isostatic pressing. In wet bag isostatic pressing, the mold is filled with the powder feedstock and sealed. The bag is then placed into a pressure vessel whereupon compaction is performed using an oil/water mixture. Typically, wet bag isostatic pressing is not used as an industrial procedure because it is highly labor intensive and difficult to automate. Furthermore, because the dimensional control is poor compared to dry-bag isostatic pressing, large parts are typically produced and then green machined to obtain the desired dimensions. This technique is typically desirable for high pressure compaction with typical pressures ranging from 275-1380 MPa⁷⁰.

In dry-bag isostatic pressing, the sealed elastomeric bag is subjected to radial compaction via hydraulic fluid from within a rigid shell. Typical pressing ranges for dry-

bag isostatic pressing are 21-275 MPa. This procedure is far more commercially viable than wet-bag isopressing with production rates of up to 60 parts per minute. Dry bag isopressing is typically used for elongated parts such as spark plug insulators^{70,71}.

II.8.2 Compaction Curves

Typically in ceramic powder compaction, three stages are observed when observing a property of the pressed part such as porosity or relative density against punch pressure. Reed identifies these stages as:

Stage I – Granule flow and rearrangement

Stage II – Granule deformation predominates

Stage III – Granule densification predominates

During Stage I compaction, granule rearrangement occurs with Lannutti contending that the pressure effects in this stage are due to granule-granule friction. Since the pressure effects result primarily in reconfiguration of the granule packing bed, the pressure effects cause a relatively small change in the density with increasing pressure. The transition from Stage I to Stage II is referred to as the Yield Point. At this point, granule rearrangement has ceased with increasing pressure resulting in the onset of granule deformation. During Stage II compaction, granule deformation continues and further densification is produced from rearrangement now of the primary particles in the granule filling the interstices. The transition from Stage II to Stage III is referred to as the joining point. In Stage III the voids inside granules are reduced by particle rearrangement. In this region, the granules begin to lose their separate identity and act

like the bulk nonaggregated powder^{64,72-75}. These data are typically plotted as seen in Figure II.25 and referred to as a compaction curve.

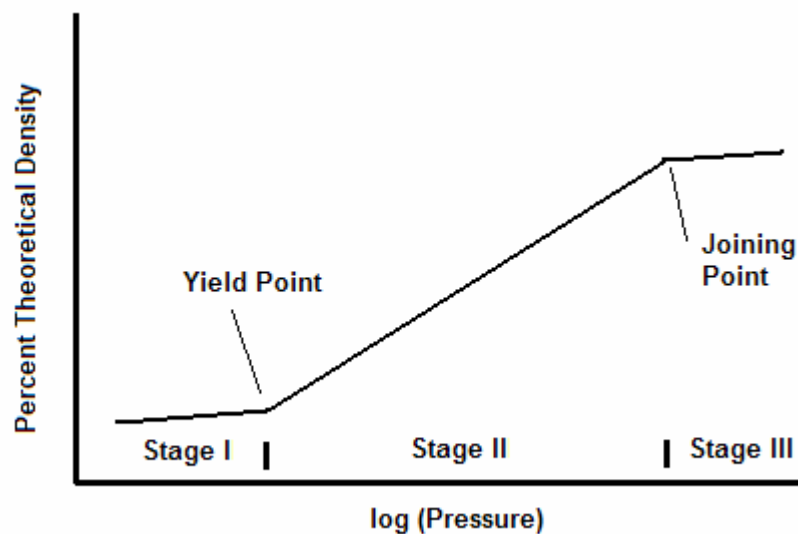


Figure II.25 A sample compaction curve illustrating the various stages

The study of compaction behavior has shown the relationship between density and compaction pressure to be empirically related via an equation of the form:

$$\rho - \rho_Y = m \ln \left(\frac{P}{P_Y} \right) \quad \text{II.84}$$

Here ' ρ ' is the density at a pressure, ' P ' above the apparent yield point ' P_Y ', where the pressed piece exhibits a density, ' ρ_Y '; ' m ' is an empirical slope. This equation is parametric as each of the three Stages has a specific slope associated with it, indicative of the varying densification mechanisms eliciting different compaction responses. This relationship is identified as being entirely empirical as there is no fundamental explanation for this semi-log dependency⁶⁴.

Compaction curves can be obtained by one of two methods. The first method, used by Niesz et al.⁷⁵, involved the pressing of numerous samples from 0.01 MPa to 137.89 MPa via a dual action steel die and from 6.89 to 689.48 MPa via isostatic

pressing. Samples were pressed and then ejected to obtain the densities of each sample. This technique eventually was found to be cumbersome because of the large volume of samples required to generate useful data.

An improvement on this technique was the use of a press where a specific height of the loading crosshead was achieved and the load was recorded as a function of this position. The crosshead position could then be manipulated with knowledge of die parameters to serve as a measure of relative density. This technique was finally automated by Messing et al., whereupon through computer interface, the crosshead position could be actively monitored along with the registered load such that in-line continuous monitoring of compaction could be achieved. This technique was heralded as being the most realistic means of assessing compaction in real industrial processes since there had been some question raised regarding previous techniques because of the discontinuity resulting from samples pressed to different pressures⁷⁶.

Messing's technique was amended by Matsumoto⁷⁴ who cautioned that the technique did not take into account an important parameter, machine compliance. Matsumoto identifies the frame, the die itself, the compact and the load cell as being contributors to compliance, yet the contribution of former three is argued to be insignificant compared to the load cell. Since a load cell is effectively a Hookean linear elastic solid, higher loads will result in a higher displacement. Since the crosshead travel during compaction is monitored relative to the frame, the displacement of the load cell is not taken into consideration. This allowed for a correction to the apparently erroneous 'high pressure breakpoint' that had been observed, such as in Figure II.26. The rationale

for this technique, according to Matsumoto, is to accurately track density values during this technique⁷⁶.

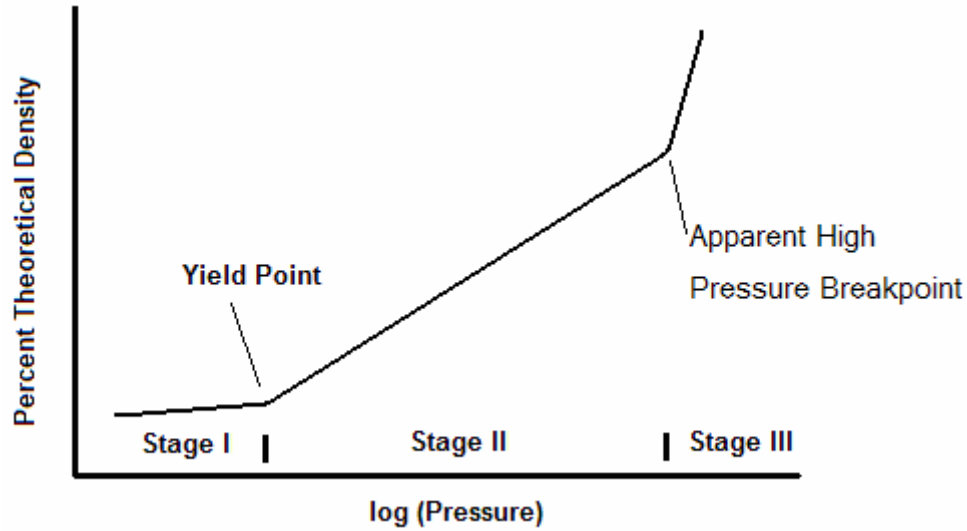


Figure II.26 Compaction curve uncorrected for machine compliance showing the erroneous high pressure breakpoint

Mort⁷⁷ suggests an equation for machine compliance correction via a technique referred to as the unload-subtraction method. In this technique, the following equation is proposed:

$$L = L_{final} + Z_{load} - Z_{unload} \quad \text{II.85}$$

Here, ' L ' and ' L_{final} ' are the thicknesses for any given load and the thickness of the ejected pellet respectively; ' Z_{load} ' and ' Z_{unload} ' are the crosshead positions at the given load during the loading and unloading cycles respectively⁷⁷.

Compaction curves typically are used to evaluate properties of the granule feedstock with respect to the final microstructure produced. For example, Reed maintains that the measure of the yield point can vary according to the content of binder and plasticizer in the system according to the following equation:

$$P_Y = K \left(\frac{PF}{1 - PF} \right) \left(\frac{V_b}{V_p} \right) S_0 \quad \text{II.86}$$

Here, ' P_Y ' is the yield point during compaction; ' K ' is an empirical constant; ' PF ' is the packing fraction; ' V_b ' and ' V_p ' are the volumes of binder and plasticizer respectively; S_0 is the strength of the binder phase. Balasubramanian et al. hypothesized that an external plasticizer softened the exterior surface of spray-dried granules, which they argue is reflected in a lower yield point measured in compaction curves^{64,67}.

Reynolds investigated the influence of fatty acids of different molecule chain lengths as a lubricant via compaction curves. Reynolds' work found that while a lubricant was a significant factor in reducing the apparent yield point, there was no correlation between lubricant chain length and the degree of lubrication attained⁷⁸.

Another study performed by Niesz et al. used the yield point to determine the strength of aggregates of alumina. Their work was concerned with powders of primary particle size in the submicron range with surface areas ranging from 3 m²/g to 13 m²/g exhibiting different degrees of porous aggregation based on varying levels of calcinations. The technique ceded by this investigation was the extrapolation of the apparent Stage I and Stage II regimes on a semi-log plot to an intersection point. The pressure corresponding to this intersection point was argued to be the extrapolated yield point⁷⁵.

II.9 Particle packing and permeability

II.9.1 Packing of Monomodal Nonporous Spheres

The packing and size characteristics of a ceramic body are critical in consideration of numerous stages of ceramic processing, be it during pre-forming stages to control the angle of repose, during forming to control factors such as slip flowability, or during post-processing to control density and of a body⁷⁹.

Westman and Hugill⁸⁰ first published data suggesting that spherical particles of uniform size appeared to pack in such a manner as to consistently provide a void volume percentage of approximately 40% for spheres of sizes ranging from approximately 1.02-4.83 mm in diameter suggesting a size-independent effect.

This theory is expanded by White and Walton⁸¹ who contend that monosized spheres under cubic packing will provide voids occupying 47.64% of total cubical unit volume whereas in a cylinder of diameter d , a sphere of diameter d will contribute 33.3% of the void volume; eight smaller monosized spheres will contribute 42.5% of the void volume. Ultimately with decreasing sphere diameter to cylinder diameter, this void fraction begins to approach the same value as cubical unit void volume. Ultimately five types of models for packing are described by White and Walton: Cubical, Single-Stagger, Double Stagger, Pyramidal and Tetrahedral. These models are described in Figure II.27 while computed theoretical void volumes for each of these configurations is presented in Table II.3.

Single Stagger is later renamed by McGear⁸² as Orthorhombic while Pyramidal (referred to as Face-Centered Cubic) and Tetrahedral (referred to as Hexagonal-Close

Packed) are combined into one. McGeary experimentally found the cubical packing to be inherently unstable and found the orthorhombic configuration as the predominantly occurring arrangement. Moreover, experimental variations of cylinder to sphere diameter packing as described from the efforts of White and Walton found that for a 200:1 ratio good agreement was reached between theoretical solids volume fraction of 62.5% and experimental results^{81,82}.

<u>Packing Model</u>	<u>Void Volume Percentage (%)</u>
Cubical	47.64
Single Stagger	39.55
Double Stagger	30.20
Pyramidal	25.95
Tetrahedral	25.95

Table II.3 Computed Theoretical Void Volumes for the Packing Models Presented by White and Walton

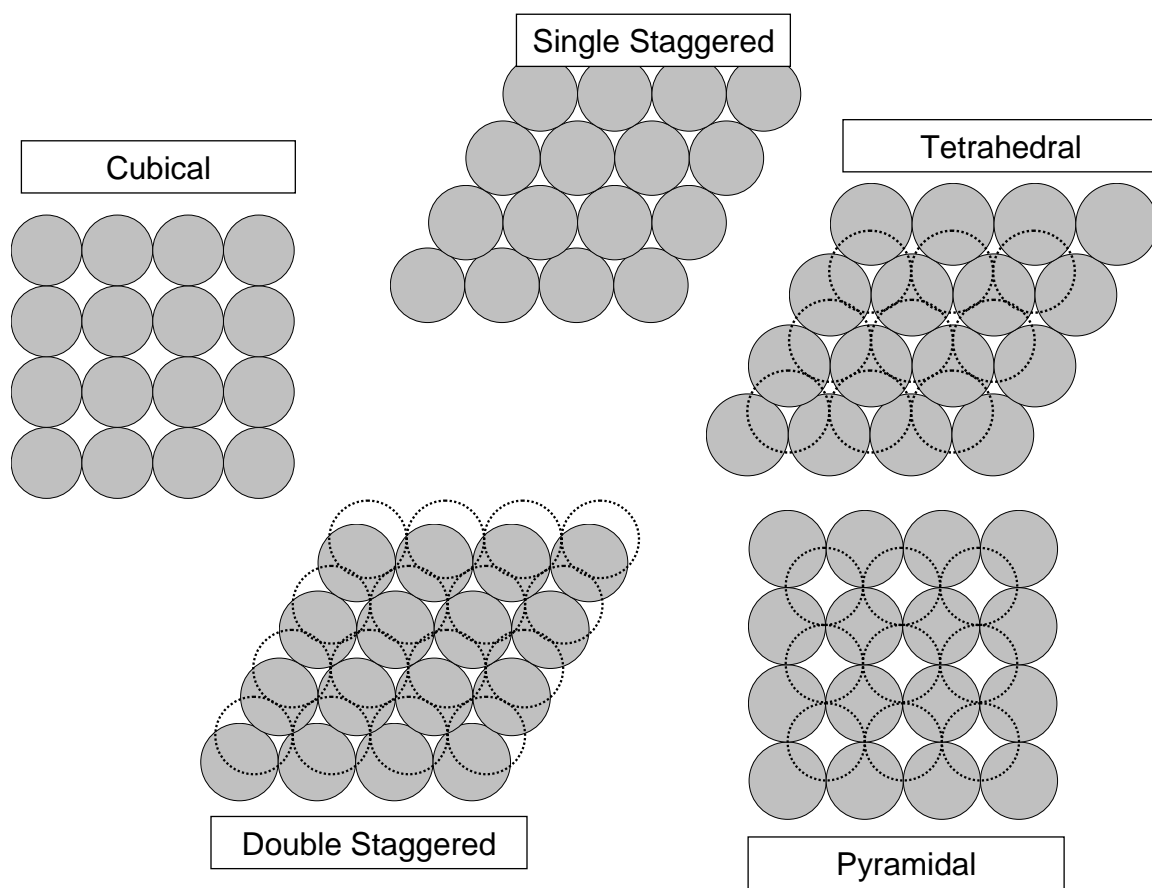


Figure II.27 Illustration of the various packing models presented by White and Walton (redrawn from [79])

The packing models described above universally concede that if monosized spherical particles pack according to a particular model or exhibit a specific non-stochastic configuration, then the volume of pores in the bulk structure comprised of these units is a function of the porosity at the local packing configuration regardless of the size of the spheres being packed. This means that for spherical particle groupings that can be vaguely described by terms such as ‘coarse’ or ‘fine’, the void volume created by interstices between particles is the same regardless of the particle size.

However, further presented is that the ordered nonstochastic packing of particles of a specific size does result in the creation of interstices which are in fact a function of the size of the particles themselves. Reed specifically cites that specifically for the low density cubic model and the higher packing efficiency tetrahedral model the ratios of the interstice diameter to particle diameter are 0.51 and 0.22 respectively. This can be seen as reflective of the differences in the packing efficiency between the two models⁷⁹.

Additionally there is a commonly accepted random packing model for systems, referred to as the Random Close-Packed Model (RCP). Despite the delineation as exhibiting a specific behavior, this is often broadly and loosely characterized as a model. It is conceded, however, that typically a close-packed random packed structure of monosized spheres will exhibit a packing efficiency of approximately 64%. It can be argued that the ratio of the interstice size to particle size will subsequently exhibit much broader, less discrete values, as the aforementioned models⁸³.

Reed, however, further contends that in real particle systems, the optimal packing may be inhibited by factors such as surface roughness causing friction and impairing the

rearrangement of particles into their optimal packing configuration. This is referred to as hindered packing. This can be overcome either by lubrication to aid in particles ‘sliding’ into a denser configuration or mechanical forces such as vibration⁷⁹.

II.9.2. Packing of particles of Multimodal and Continuous Size Distribution

In ceramic systems where considerations of density and shrinkage become highly relevant it is necessary to optimize the green density of a body. One means of doing such is the use of controlled particle sizes to optimize packing distributions. The models presented above indicate that monosized systems will exhibit a maximum packing efficiency, ‘ PE_{\max} ’ of 74.05% of the total available volume. Such a high percentage of voids is undesirable in the preparation of dense ceramic bodies and as such, typically monomodal size distributions are avoided. The simplest remedy to this situation is the incorporation of a second mode of particle size that is sufficiently small so as to occupy the interstices created by the original particle size mode. In the incorporation of this bimodal size distribution (which for discussion purposes will be labeled empirically as ‘coarse’ and ‘medium’ depending on size rankings) the packing of these bodies Equation II.106 describes the resultant new PE_{\max} term^{84,85}:

$$PE_{\max} = PE_c + (1 - PE_c)PE_m \quad \text{II.87}$$

Where ‘ PE_c ’ is the packing efficiency of the coarse particles and ‘ PE_m ’ is the packing efficiency of the medium particles. The inclusion of a third mode of particles (labeled ‘fine’ with a packing efficiency ‘ PE_f ’) to fit into the new interstices created by the medium particles modifies Equation II.106 to read^{79,84}:

$$PE_{\max} = PE_c + (1 - PE_c)PE_m + (1 - PE_c)(1 - PE_m)PE_f \quad \text{II.88}$$

This is referred to as the Furnas model. These equations are relevant for discrete multi-modal sizes. However, more commonly encountered in ceramic powder systems are continuous distributions. Such a model is presented as the Andreasen model per the following equation:

$$F_v(a) = \left(\frac{a}{a_{\max}} \right)^n \quad \text{II.89}$$

Here, ' $F_v(a)$ ' is the cumulative finer volume distribution, ' a_{\max} ' is the maximum particle size. The exponent ' n ' is not entirely explained and remains an empirical fit component. Zheng et al.⁸⁴ would later adapt the Andreasen model to a discrete system such that n was related to real parameters by:

$$n = \frac{-\log \phi}{\log R} \quad \text{II.90}$$

Here, ' ϕ ' is the interstitial pore fraction or porosity and ' R ' is the particle size ratio of coarse to fine. The work of Andreasen argues that dense packing requires n to be between 0.33 and 0.50. In order to acclimate this to a real particle system, since Andreasen's equations are not exclusive of particles of infinitesimal size, Dinger and Funk modified Equation II.108 to include the minimum particle size, ' a_{\min} ', by:

$$F_v(a) = \frac{a^n - a_{\min}^n}{a_{\max}^n - a_{\min}^n} \quad \text{II.91}$$

III. Method of Attack

The extrusion of NO_x catalysts from starting materials of high surface area is largely complicated by the amount vehicle required to impart sufficient plasticity to facilitate extrusion. In addition, it is common that organic additives such as surfactants, plasticizers, lubricants and binders are utilized. To aid in the extrudability of a paste, titanias utilized for this application are anatase phase synthesized from the sulfate process. In the process of synthesizing anatase for this application, Kobayashi⁸⁶ argues that a residual amount of sulfate is preserved to provide Brønsted acid sites for ammonia adsorption in the SCR process for faster catalysis. In production of anatase it is common to alter synthesis parameters so as to produce titanias of different residual sulfate content. The observed consequence of synthesis variable modification has been observed to vary the extrudability. The goal of this work is to explain these differences in extrudability for powders of different synthesis conditions by evaluating their degree of aggregation, strength of aggregation and resultant microstructure for suitability as a catalyst. In order to achieve this goal, the following objectives will be met.

III.1 Objective One: Characterization of Degree of Powder Aggregation

Powder characterization will be performed by evaluating the Average Agglomerate Number of each powder. This will be carried out by ultrasonication and light scattering to determine the aggregate diameter and measurement of BET surface area to characterize the primary particle diameter. This would offer a means to evaluate the as-synthesized degree of aggregation for the starting powder. The powder sulfate

level will be evaluated by turbidity measurements of a centrifuged supernatant of the sample. Scanning Electron Microscopy (SEM) of the dry powder will be conducted to establish the approximate size of the various orders of aggregation encountered in this system. Due to the nature of synthesis and initial digestion to form titanyl sulfate a degree of residual sulfate is often present in these systems. Moreover, some have argued that a residual amount of sulfate creates Bronsted acid sites for ammonia adsorption in SCR NO_x catalysts. Sulfate can be present either as an intercrystalline bridging mechanism for primary particles or as unreacted surface soluble sulfate. A powder washing study will be conducted to investigate the quantity of sulfate removed with successive wash iterations and track the microstructure of the bulk powders to assess whether the role of sulfate is as an intercrystalline bridging mechanism or soluble surface accessible sulfate.

III.2 Objective Two: Measurement of Strengths of Various Aggregation Stages

Dynamic Stress Rheometry (DSR) will be utilized to measure the strength of interaction between secondary and higher order aggregate stages. Prior to investigation, a common solids concentration must be established whereupon a transition between linear elastic and viscous fluid behavior can be clearly observed for the six powders under study. Solids concentration buildups will be performed in 5 percent (by mass) increments until a common solids loading where the elastic to viscous transition is observed for low and high sulfate powders at stresses ranging from 0.1 to 100 Pa. This stress range is sought to imitate the shear stresses encountered during extrusion. The linear elastic G' and powder yield stress will be correlated with powder surface properties to determine

the role of the starting powder in the suspension elasticity and in the strength of the aggregate network. The yield behavior will be corroborated via immersing a sample of low and high sulfate suspensions drawn from both the linear elastic regime and the yield regime in liquid nitrogen to preserve the structure for investigation via scanning electron microscopy.

It is hypothesized that stress rheometry up to 100 Pa will not provide sufficient shear conditions to rupture primary scale aggregates. This implies that the typical extrusion conditions preserve primary scale aggregates. Compaction will be utilized via a computer-controlled constant velocity crosshead to apply compressive loads up to 750 MPa. Stages I and II will be empirically identified and separately linearized to extrapolate the intersection point. Due to the use of extrapolation, this will be repeated five times to establish a mean extrapolated yield point in compaction.

III.3 Objective Three: Impact on Packing Characteristics of Various Shear Conditions

Aggregates are argued to be distinguishable from dense structures because of the open and more disordered structure producing irregular packing of the aggregate subunits. Reed identifies coagulation, flocculation and similar processes as impeding the packing characteristics but stops short of referring to an aggregate as a general form of hindered packing of its constituent subunits. A rupture of the aggregate can cause a reordering and reorganization into a denser configuration. The presence of a denser configuration from reordered subunits can be reflected in the size of the resulting

interstices since the interstices produced will be a function of the size of the subunits being reconfigured.

In order to achieve this, tape casting will be utilized to produce bulk structures at shear conditions similar to extrusion such that the necessary additives to produce an extrusion body can be omitted so as to avoid obscuration of aggregate properties. Casting will be carried out at two different velocities one order of magnitude apart to evaluate variation of different levels of shear on aggregate breakdown via microstructure of the tape. Initially viscometry will be performed to determine the appropriate rheological model to serve as an input variable in Finite Element Modeling (FEM) simulations. Upon determining via FEM simulations the region of maximum shear, this region will be investigated via SEM to assess the state of aggregation of the tapes. Mercury porosimetry will be performed on the produced tapes as well as the pellets formed in powder compaction to determine the size of the interstices produced in these processes and subsequently the size of the flowing unit under the shear conditions specific to each process.

IV. Experimental Methods

IV.1 System of Study

This investigation was conducted on a series of nanosized titanias from Millennium Inorganic Chemicals that were synthesized via a sulfate process illustrated in the adjacent figure. The source ore for the procedure is typically ilmenite (FeTiO_3) which is subsequently reacted with sulfuric acid. The iron is then typically washed from the system leaving titanyl sulfate. The system is then subsequently washed with water to remove the sulfate, while seed particles of TiO_2 are used to nucleate the target product. The final product is subsequently calcined, milled and then packaged. Through a patented Design of Experiment procedure, variation of specific synthesis parameters has resulted in numerous variants. These variants are seen to vary specifically in their residual sulfate level and in their specific surface area.

IV.2 Aggregate Characterization

IV.2.1 Average Agglomerate Number

The individual powders were characterized for their degree of aggregation via Average Agglomerate Number (AAN). Two specific measurements are required in order to compute the AAN of a specific powder: the particle size of the powder system and the equivalent spherical diameter obtained from knowledge of the BET surface area.

IV.2.1.1 Particle Size Measurement

Particle size measurement was performed using laser light scattering via a Coulter LS230 with a small volume module. Background and auto-alignment calibrations were performed prior to the start of each sample. All samples were initially weighed as 0.05 g of powder and combined with 49.95 g of deionized water to create a 50 g suspension of a low solids concentration in order to facilitate minimal interparticle interactions that would prematurely aggregate the system. The resultant suspension was then ultrasonicated for 2 minutes to break down any secondary or higher order aggregation stages. All ultrasonication was performed via a Heat Systems-Ultrasonics Inc W-385 Ultrasonicator using a 20 kHz probe on a continuous output while employing a 50% duty cycle.

Upon completion of ultrasonication, the samples were immediately injected into the light scattering chamber using 1 ml polyethylene pipets. The obscuration of the module was monitored via a computer-controlled program interface. The parameters employed required an obscuration value between 40% and 55%. The ultrasonicated suspension was added until the obscuration of the module was within these parameters. The d₅₀ or median particle size was measured via a computer recorded histogram via a log-normal size scale. The d₅₀ was recorded for each powder.

IV.2.1.2 Surface Area Measurement

Surface area measurements were performed via a Coulter SA3100 Surface Area Analyzer. All samples were initially weighed as 0.5 gram samples and placed in a drying oven for 24 hours prior to testing. A sample tube and spacer was selected and weighed prior to insertion of the powder sample. Three weights were recorded of the tube and

glass spacer rod together and the average was recorded as the tube weight. The sample was then inserted and then outgassed at 300 Celsius for one hour. Upon completion of the outgas phase, the sample tube was then weighed. Three weights were recorded and averaged to obtain the average weight of the sample tube with the sample inserted. The original average sample tube and spacer weight was then subtracted from this weight in order to obtain the 'true' sample weight. Multipoint BET analysis was conducted from p/p_0 values ranging from 0.0 to 0.2. The BET surface area was reported by the instrument and then logged for each sample. Equivalent spherical diameter calculations were obtained by Equation II.28. The requisite powder density was obtained from the manufacturer to be 3.84 g/cm^3 .

IV.2.2 Sulfate Measurement

Sulfate measurements were performed using a turbidity test via spectrophotometry. All powder samples were prepared from 10 g powder and 90 g deionized water. Suspensions were mixed by hand for approximately 1 minute. The suspensions were then centrifuged via a Beckman J21-M centrifuge at 10,000 RPM, 10 degrees Celsius for 5 minutes. The supernatant produced was then decanted and stored separately.

Spectrophotometry was performed using a Betz DR2000 spectrophotometry. Per the requirements of sulfate testing, a wavelength of 450 nm was set as the test parameter. 24 ml of deionized water and 1 ml of the supernatant were placed into the reference cell and the test cell. The contents of the test cell were reacted with a barium chloride (BaCl_2) reagent supplied by Hach Co.. The test cell was rotated by hand until the particulate

reagent had been completely dissolved. The reference cell was then tested in order to obtain a 'zero' reading, whereupon the test cell was then measured to obtain the sulfate level in 1 ml of the supernatant. The value obtained via the test was multiplied by the dilution factor (here, 25) to obtain the concentration of sulfate in the supernatant. This value was subsequently divided by the mass of powder used in centrifugation to obtain the level of sulfate in the powder.

IV.3 Stress-Controlled Rheometry

Stress-controlled rheometry was performed using a TA Instruments AR-1000N Rheometer. Samples were initially weighed as 22.5 g of powder and 27.5 g of deionized water and mixed by hand for approximately 1 minute. Testing parameters for this experiment included an aluminum vaned rotor geometry and a 50 ml capacity aluminum sample chamber. Samples were then initially pre-sheared at a fixed angular velocity of 20 radians per second for a period of 2 minutes to obtain a greater degree of mixing and suspension homogeneity. Upon completion of the pre-shearing, the samples were allowed to equilibrate for an additional 2 minutes to allow the suspension to regain its structure. Samples were then tested in logarithmic oscillatory stress increments from 0.1 to 100.0 Pa with a span of 20 points per logarithmic decade and a 3 second equilibration between increasing pulses of applied oscillatory shear stress.

IV.4 Tape Casting

IV.4.1 Modeling the Shear Stresses in a Tape Casting System

In order to fully investigate the effect of applied shear in a tape casting system, a commercial Finite Element Modeling software package POLYFLOW^{TM*} was utilized. Input variables for this software required were doctor blade gap, casting velocity and rheological model. In order to obtain the rheological model that was appropriate, viscometry was utilized to measure the viscosity of the targeted tape casting medium as a function of applied shear rate. Viscometry was performed using a TA Instruments AR-1000 Rheometer via a constant flow procedure. Samples were prepared as 22.5 g powder, 27.5 g deionized water and then mixed by hand for approximately one minute. The samples were then tested using an aluminum vaned rotor geometry in a 50 ml aluminum cell. No preshearing or equilibration was utilized. Viscometry tests were performed from shear rates of 1 sec^{-1} to 100.0 sec^{-1} . The viscosity data were then plotted as a function of the applied shear rate and an appropriate rheological model and appropriate fit constants were chosen and input into the software in order to generate the simulation.

IV.4.2 Tape Casting Procedure

Tape casting was performed via an air-driven motor with a moving doctor blade. The doctor blade was manufactured by and obtained from Richard Mistler Inc.. Doctor blade height was adjusted via micrometers attached to the doctor blade. Casting was carried out on a glass substrate, onto which a Mylar film was placed. Doctor blade motion was attained by placement on a chain connected to the air-motor assembly. Variation of the air pressure resulted in variation in the chain velocity and ultimately the

*POLYFLOWTM is a product of a Fluent Inc.

casting speed. Pressures of 20 and 55 psi were found to correspond to casting velocities of 0.85 cm/sec and 9.09 cm/sec. A small quantity of slurry was placed ahead of the doctor blade. The slurry was composed of Deionized water and titania with no additional additives or surfactants employed. Upon casting the tape was dried overnight and then calcined at 600 degrees Celsius overnight. Calcination temperature was limited by observations of Augustine et al.⁸⁷ regarding the effect of calcination temperature on the necking and degradation of specific surface area in nanosized titania catalysts as well as simulating typical firing conditions for the bulk extrudate.

IV.4.3 Assessment of Packing Characteristics

Packing characteristics of the resultant tape were assessed via mercury porosimetry. Each sample was dried for 24 hours prior to testing. For all mercury porosimetry, samples were dried for 24 hours at 110 degrees Celsius. Samples were then placed in 3 cc bulbs that were evacuated to 50 μ m Hg pressure for 5 minutes before being filled with mercury. High pressure analysis was performed via a Micromeritics 366 Porosimeter for applied pressures ranging from 0.5 to 30,000 psi.

IV.5 Compaction Curves

IV.5.1 Sample Preparation

For compaction curves, 10 g of powder were weighed and mixed with 90 g of deionized water by hand. The suspension was then placed inside zip-lock polyethylene bags and sealed. The bags housing the suspension were placed inside a centrifuge vessel

and centrifuged at 10,000 RPM at 10 degrees Celsius for 5 minutes. Upon completion, the resulting supernatant was decanted and stored separately while the polyethylene bag was removed from the vessel. The bags were opened to allow the filtrates to dry in ambient conditions for 24 hours to produce a sufficiently solid transferable filtrate. Upon completion of ambient drying, samples were placed in a drying oven at 110 degrees Celsius and dried for an additional 24 hours to remove residual moisture from the system.

The solid filtrate was then weighed as a $0.140 \text{ g sample} \pm 0.005 \text{ g}$ and compacted using a stainless steel cylindrical KBr pellet die with a cross-sectional diameter of 12.7 mm (0.5 inches).

IV.5.2 Compaction Procedure

All compaction was performed via an Instron 4505 loading frame using a 100 kN load cell. The load cell was calibrated and balanced prior to testing. The crosshead was lowered until a near-zero gap was achieved between the crosshead and the top surface of the punch. Compaction loading was performed at a velocity of 1.8 mm/min until the maximum load of 100 kN was achieved, whereupon the computer-controlled crosshead automatically was stopped. Compaction unloading was carried out at 1.8 mm/min immediately following cessation of the load procedure and proceeded until the crosshead was visually observed to no longer be in contact with the top punch. Upon ejection of the sample from the die, the sample thickness was measured using calipers and the mass was measured.

IV.5.3 Compaction Data Manipulation

The output data of compaction provided by the computer-controlled loading were crosshead position and the corresponding load recorded from the transducer at that position. The load recorded by the transducer was converted to pressure by dividing the load recorded by the circular cross-sectional area of the die. The crosshead position was calibrated against the final crosshead position (i.e. the location of the crosshead at 100 kN of load) and added to the measured thickness of the pressed piece in order to obtain the relative height during compaction.

$$L_{relative} = S_i - S_{final} + L_{compact} \quad \text{IV.1}$$

Here ' S_i ' is the crosshead position at the load recorded; ' S_{final} ' is the crosshead position at maximum load; ' $L_{compact}$ ' is the final thickness of the piece; ' $L_{relative}$ ' is the relative height of the piece.

This relative height was multiplied by the circular cross-sectional area of the die in order to obtain the relative volume of the pressed piece. The final mass of the compacted pellet divided by the relative volume at a specific crosshead position provided a means to track the density of the pressed piece as a function of the applied pressure.

$$\rho = \frac{m_{compact}}{L_{relative} * \pi D_{die}^2} \quad \text{IV.2}$$

$$\%TD = \frac{\rho}{\rho_{theoretical}} * 100\% \quad \text{IV.3}$$

Here, ' ρ ' is the relative density; ' $m_{compact}$ ' is the mass of the compacted sample; ' $L_{relative}$ ' is the relative height; ' D_{die} ' is the diameter of the die; ' $\rho_{theoretical}$ ' is the theoretical density; ' $\%TD$ ' is the percent theoretical density

IV.5.4 Linear Regression of Compaction Curve Stages and Numerical Calculation of Yield Point

So-called ‘ideal’ compaction curves show a parametric linear relationships between Percent Theoretical Density and $\ln(\text{Pressure})$. Using linear regression, specific regions believed to correspond to Stage I and Stage II compaction respectively were fit to semi-log equations of the following form:

$$y = A \ln(x) + B \quad \text{IV.4}$$

Here ‘y’ represents the Percent Theoretical Density, ‘x’ represents the Punch Pressure while ‘A’ and ‘B’ are semi-log fit parameters. Therefore, the fit equations for Stage I and Stage II each would have a separate semi-log fit equation would be of the form:

$$y = A_{\text{StageI}} \ln(x) + B_{\text{StageI}} \quad \text{IV.5}$$

$$y = A_{\text{StageII}} \ln(x) + B_{\text{StageII}} \quad \text{IV.6}$$

Each semi-log equation was fit to a line that exhibited a minimum correlation coefficient (R^2) of 0.990. This value was empirically determined to be the minimum correlation coefficient required to produce a sufficient linear fit. Niesz et al. have contended that the transition from Stage I to Stage II compaction can be extrapolated as the intersection point of these two fit equations. Their work argued that this could be done graphically. Pursuant to this endeavor, Mort et al.⁷⁷ have also used linear regression to calculate the transition points between compaction stages.

Determining the compaction pressure corresponding to this extrapolated yield point requires setting the fit equations equal to each other and solving for $\ln(x)$:

$$\ln(x) = \left(\frac{B_{StageII} - B_{StageI}}{A_{StageI} - A_{StageII}} \right) \quad \text{IV.7}$$

Therefore, the extrapolated yield point, and subsequent measured strength of primary scale aggregates can be expressed as:

$$\sigma_{aggregate} = \exp \left(\frac{B_{StageII} - B_{StageI}}{A_{StageI} - A_{StageII}} \right) \quad \text{IV.8}$$

IV.5.5 Empty Die Compaction Run for Back-Calculation of Machine Compliance

An empty die and punch run was conducted from 0 Pa to 750 MPa to serve as a baseline for calculation of machine compliance⁸⁸. The data were obtained but not included in computation of yield points for it was not believed to affect the extrapolation technique given in Appendix I. The machine compliance curve is given as Figure IV.1.

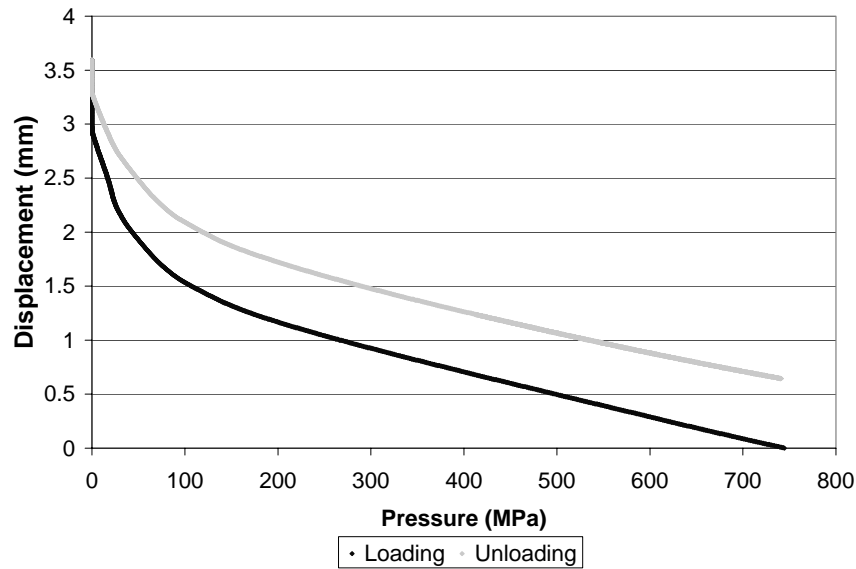


Figure IV.1 Machine Compliance Curve Obtained via Empty Die

V. Results and Discussion

V.1 Powder/Aggregate Characterization

V.1.1 Powder Characteristics

V.1.1.1 Particle Size Distribution/Specific Surface Area

Particle size distribution is presented in Figure V.1, and surface area is presented in the Table V.1. The light-scattering particle size distribution data show little variation in the starting powders size distribution or median particle size. Median particle diameters are centered at approximately 1 μm and appear to exhibit a log-normal distribution extending into the submicron range. The light-scattering data, however, offer few insights into the system without further characterization via other techniques. Such information can be obtained via the multi-point BET surface area measurements provided. The surface areas for the powders investigated in this study ranged from 71 to 127 m^2/g . Using Equation II.28 in combination with density data provided and shown in Table V.1, the equivalent spherical diameter (ESD) was calculated and found to range from 12 to 22 nm.

Powder	d_{50} (μm)	BET (m^2/g)	Calculated ESD (nm)	Density (g/cm^3)	Calculated AAN (unitless)	Soluble sulfate (ppm/L)
1	1.26	89.37	17	3.84	374306	7800
2	1.05	71.64	22	3.84	111619	6600
3	0.95	71.53	22	3.84	82271	5400
4	1.26	126.88	12	3.84	1071103	16800
5	1.15	110.22	14	3.84	533844	16000
6	1.15	117.18	13	3.84	641496	19200

Table V.1 A summary of powder characteristics and computed quantities

It is not suggested that these values represent the exact primary particle sizes but rather that they provide an understanding regarding the order of magnitude of the primary particle size. The BET data subsequently indicate that the primary particle size is approximately in the tens of nanometer size range.

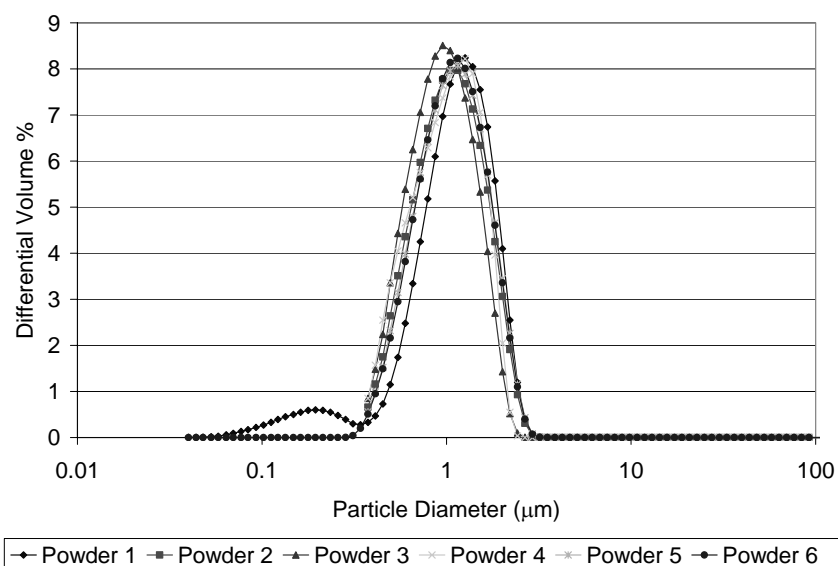


Figure V.1 Particle size distributions of the powders investigated via light scattering

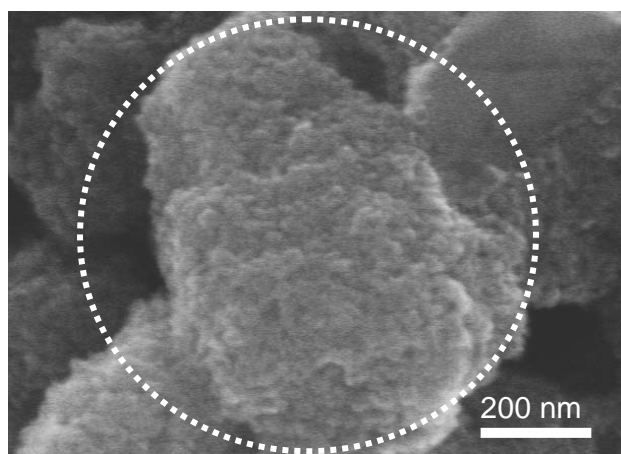
V.1.1.2 Soluble Sulfate Level

It is argued that a by-product of the sulfate solution technique is the inability to fully remove the sulfate ions from the powder during the washing and calcining stages, resulting in a quantity of sulfate remaining in the powder system. Measurements via spectrophotometry are plotted in Table V.1. Spectrophotometry measurements indicate strong variations in the level of soluble sulfate removed via a single wash in deionized water. It is not anticipated that all soluble sulfate was removed from the system on one wash cycle. However, it is believed that sulfate level measured is successive wash cycles will diminish at a level proportional to the quantity removed on the first cycle. As such, references to soluble sulfate level will be limited predominantly to results of sulfate

removal after 1 wash cycle. Powders 4, 5 and 6 show a level of sulfate removed approximately one order of magnitude higher than 1, 2 and 3, suggesting that the starting powders of the former have a significantly higher residual sulfate level than the latter two powders. Additionally, it can be argued that the differences in sulfate levels seen via spectrophotometry suggest that the sulfate is present in the form of soluble sulfate unreacted from the titanyl sulfate formed during digestion of the original ore in synthesis.

V.1.1.3 Scales of Aggregation

The dry powders were investigated via scanning electron microscopy and were found to exhibit three distinct aggregation phases as seen in Figure V.2 a)-c). These three iterations of aggregation were found to exist as three separate size regimes. As indicated in Figure V.2(a), the system appears to initially exhibit primary particle sizes on the order of tens of microns, confirming the approximate order of magnitude given via estimation of ESD via BET. The clustering of primary particles results in a primary scale aggregate approximately 1 μm in diameter, corresponding to the peaks exhibit in light-scattering particle size analysis.



(a)

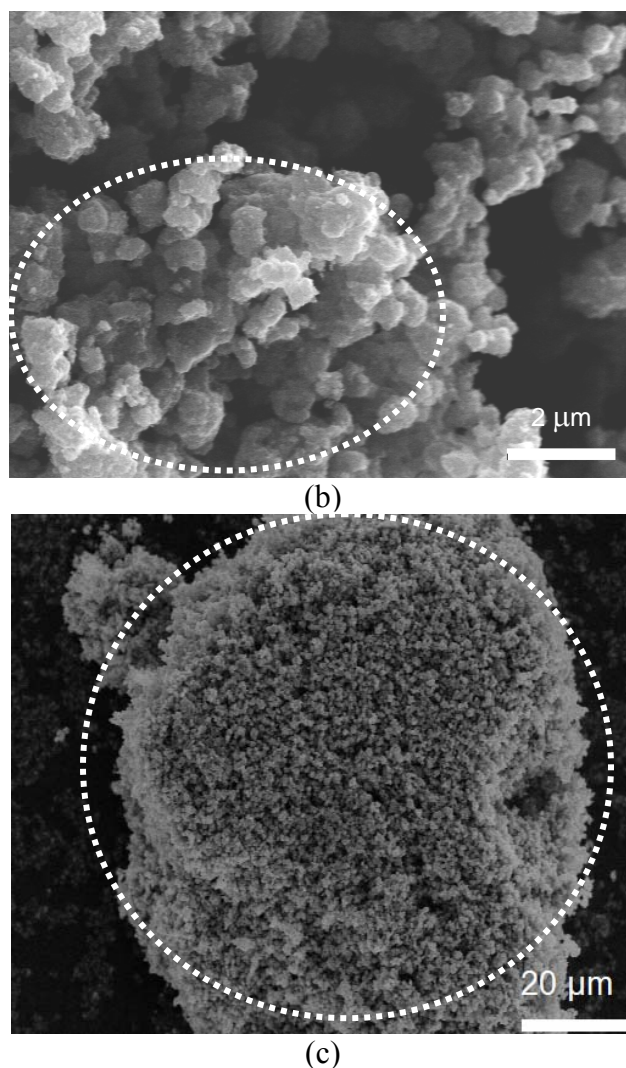


Figure V.2 Multiple Aggregation Stages seen via Scanning Electron Microscopy

In Figure V.2(b) it can be seen that the primary scale aggregates themselves appear to cluster into a secondary scale aggregate approximately 5-10 μm in diameter; in Figure V.2(c), it appears that the secondary scale aggregates form a tertiary scale aggregate of diameter 100 μm and greater. It appears that the aggregates and the primary particles are of ill-defined shape, and cannot be conveniently described by a specific particle shape. This prevents the direct fit to a specific particle packing model of a particular shape. Due to the ill-defined shape and the apparent lack of a specific aspect ratio so as to cause a deviation from a shape factor of 1.0, approximations in

consideration of particle packing for each aggregation iteration will utilize the spherical models detailed earlier.

V.1.2 Average Agglomerate Number

While fractal dimension is the common term utilized to investigate aggregates, this is primarily reserved for systems of primary particles and aggregates that are on the order of microns and tens or hundreds of microns respectively. For nanosized systems this typically requires investigation via Transmission Electron Microscopy where sample preparation techniques undermine the surface characteristics of the aggregate and obscure correlation with synthesis route variation. Average Agglomerate Number (AAN) values are computed by utilizing Equation II.29 to compute the equivalent spherical diameter (ESD) of the powders such that the primary particle size can be obtained. The median peak from light scattering is used as the aggregate diameter. The ratio of these diameters cubed (and subsequently, the ratio of the aggregate volume to primary particle volume) roughly approximates the number of primary particles comprising the aggregate (see Equation II.29). These values are displayed in Table V.1. These values are indicative of strong variations in the degree of aggregation, especially when considering powders 3 and 4. Empirically, a criterion of ‘well-dispersed’ has been previously used for powder systems exhibiting AAN values below 10. The six powders in this system are far from well dispersed; however, given the targeted end-use of the product, a stable aggregate of sufficient size yet exhibiting numerous surface sites for activity may be more desirable.

Furthermore, several key assumptions must be noted. Firstly, in utilization of equation II.10 for computing AAN, it must be assumed that the primary particles do not

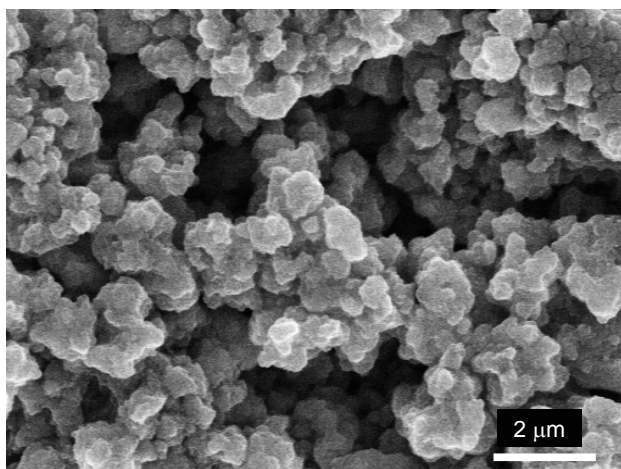
exhibit a large aspect ratio or significant anisotropy in a specific direction unless they aggregate into structures of similar aspect ratio (whereupon the common shape factor term would mutually cancel out in the upper and lower halves of the equation). Secondly, it is assumed that the 1 minute of ultrasonication to which the dilute suspension for light scattering analysis is subjected is sufficient to reduce the aggregate to its primary scale. This appears to be reasonable given the apparent agreement between particle size measurements and the aggregate seen via microscopy.

Finally, it must also be noted that the variations in AAN appear to be exacerbated by apparent gradients in the calculated ESD values. It should be noted that the variation between the minimum and maximum ESD value is nearly a factor of two, meaning that for this system where the primary scale aggregate diameter does not appear to significantly vary, the AAN values are affected by a factor of eight. It cannot be verified through techniques used in this study that the ESD values will exhibit strong variations as a function of synthesis. It is highly possible that since crystallite nucleation in a sulfate process will use similar seed material, the primary particle size should not vary as significantly as indicated. While it is not necessarily suggested that the trend of lower sulfate powders to exhibit higher AAN values is completely artificial it is rather suggested that these differences are exaggerated because of the exaggerated variation in ESD. A useful observation, however, may be that the differences in degree of aggregation are corroborated by a higher surface area reflecting rougher primary aggregate surface features.

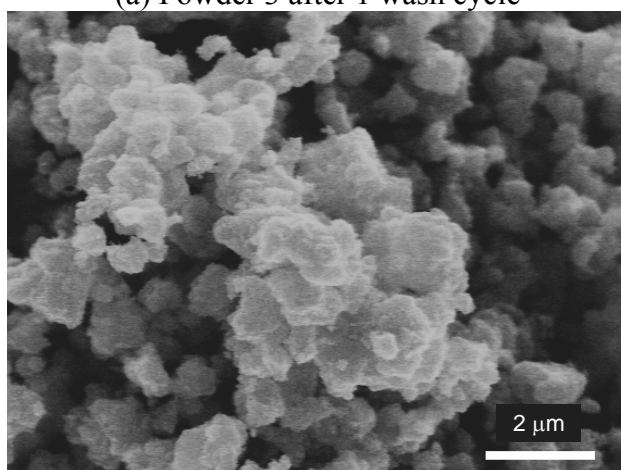
V.1.3 Powder Washing Investigation

To investigate the effect of sulfate on the powder system, powders 3 and 5 were subjected to an iterative washing procedure. A sample of the powder centrifugate after washing was investigated via microscopy to assess the microstructural features. Upon centrifugation, the filtrate was redispersed into a suspension whereupon a sample of the suspension was dried and placed on a sample holder. Micrographs for these investigations are provided in Figure V.3 a)-c) and Figure V.4 a)-c). Light scattering investigation of the slurries is presented in Figure V.5 and V.6.

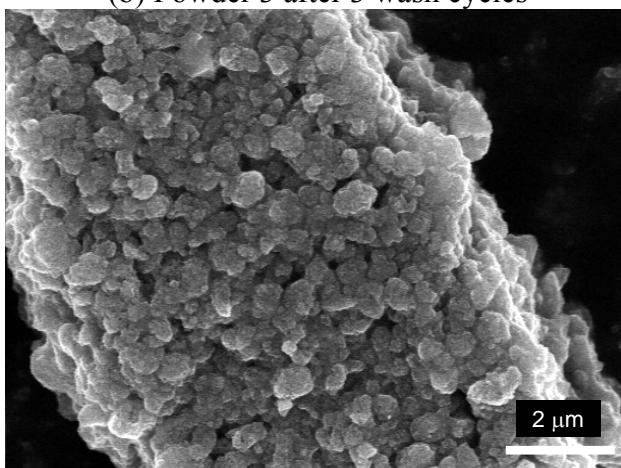
The micrographs appear to show a relatively similar structure for both powders as a function of wash iteration. Powder 3 at the 5th wash appears to exhibit a more aggregated structure between primary scale aggregates yet this distinction is not believed to be significant. Examination of Figure V.5 and V.6 both indicate seemingly larger d_{50} values than reported above. This discrepancy is believed to be rooted in the use of 10 weight % slurries for washed samples, while earlier reported light scattering was conducted at 0.1 weight % powder suspensions that were subjected to a period of ultrasonication. The shift of the peaks can be potentially explained as a measure of the primary scale aggregate plus several extraneous 'links' in the network. For powder 3, there appears to be a shift to a lower peak value from one wash cycle to three wash cycles yet a shift to a higher peak value at five wash cycles. This is in contrast to Powder 5 which exhibited a steady shift to a lower peak value with successive wash cycles.



(a) Powder 3 after 1 wash cycle

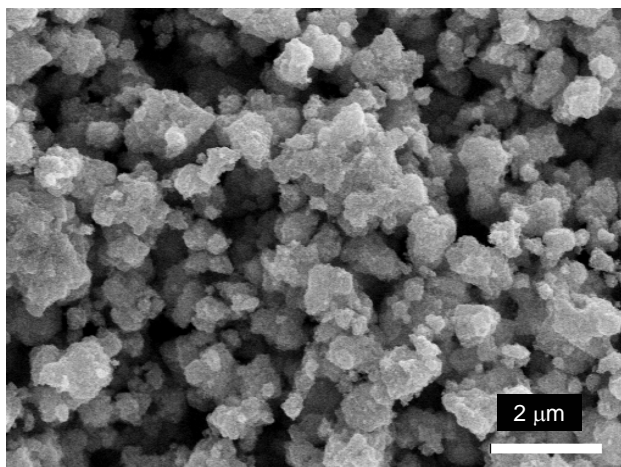


(b) Powder 3 after 3 wash cycles

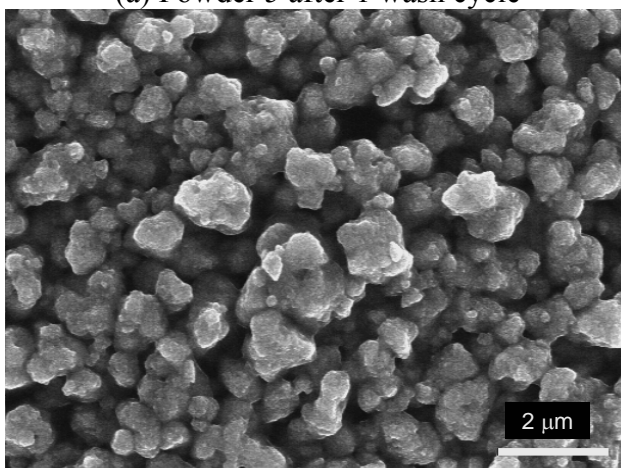


(c) Powder 3 after 5 wash cycles

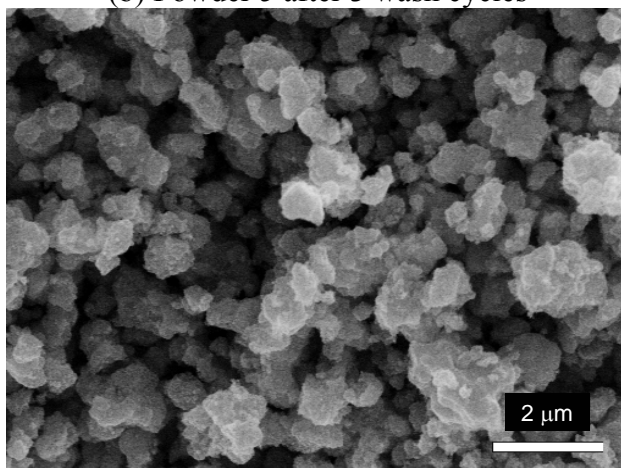
Figure V.3 Powder 3 washing micrographs



(a) Powder 5 after 1 wash cycle



(b) Powder 5 after 3 wash cycles



(c) Powder 5 after 5 wash cycles

Figure V.4 Powder 5 washing micrographs

Sulfate and pH levels in the wash supernatants are tracked in Figure V.7 and V.8 respectively. As initially speculated, the supernatant sulfate level with successive wash

cycles does appear to decrease relative to the amount initially measured in the first wash cycle. As would be expected, decreasing amounts of sulfate removed with successive washes results in subsequent increases in the supernatant pH. Of particular note is the absence of sulfate data above 3 washes for Powder 3. For wash cycles beyond this, it was not possible to obtain a clear supernatant under the washing conditions used. A cloudy white supernatant was produced. Upon investigation via drying a sample of this supernatant, a drastically different microstructure from the ones seen above for the powder was produced (see Figure V.9).

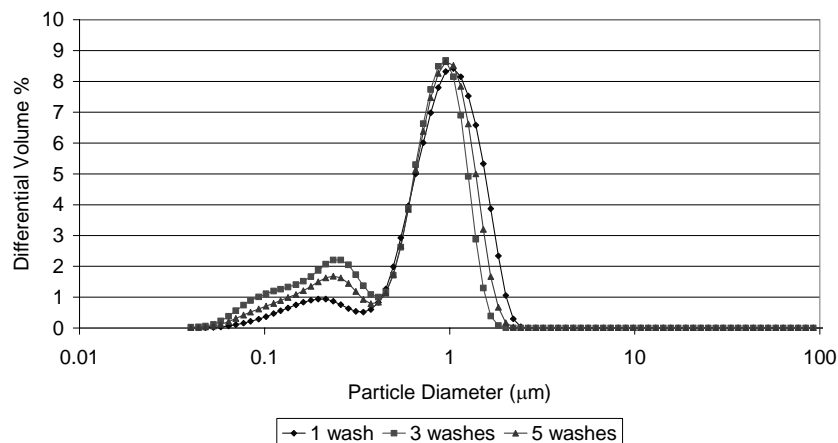


Figure V.5 Particle size distributions of Powder 3 slurries during washing

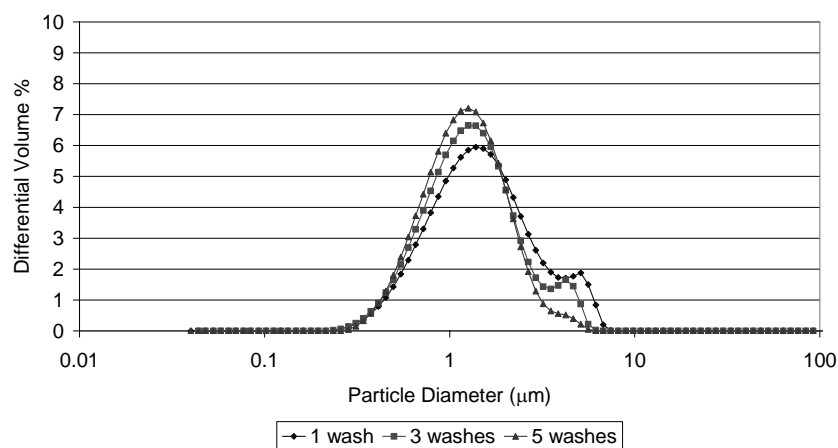


Figure V.6 Particle size distributions of Powder 5 slurries during washing

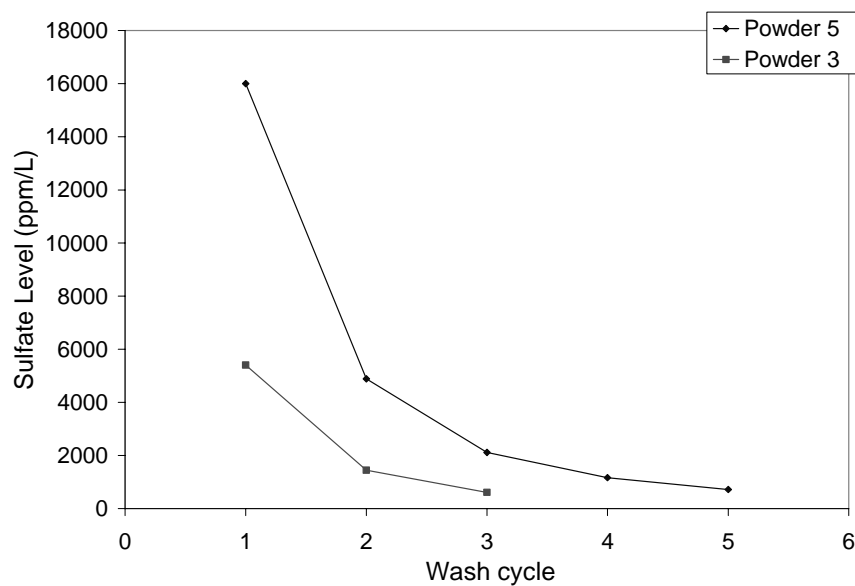


Figure V.7 Sulfate level measured in the supernatant as a function of wash cycle iteration

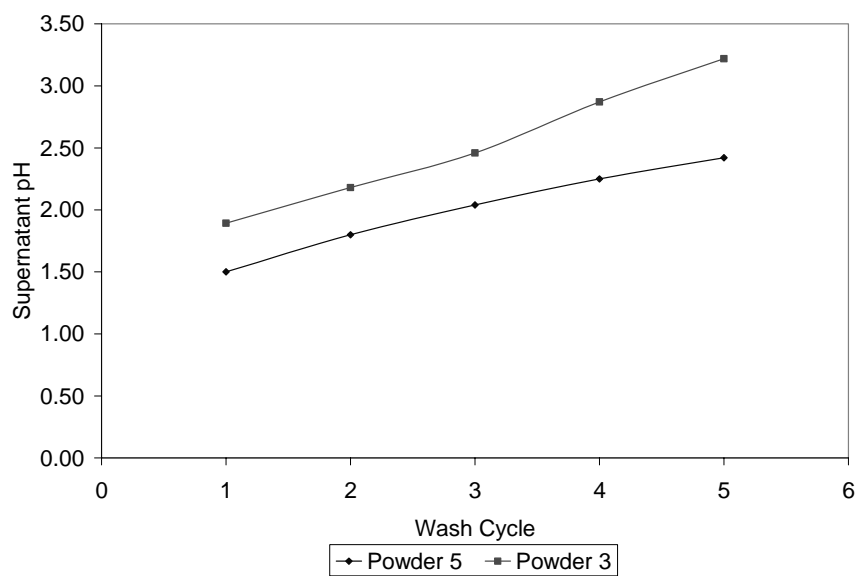


Figure V.8 Supernatant pH measured as a function of wash cycle iteration

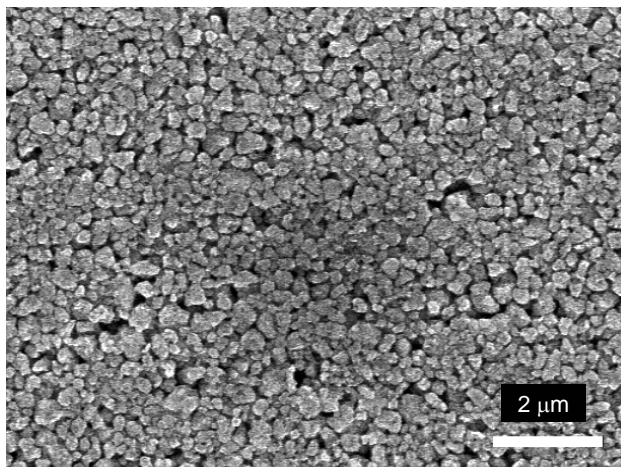


Figure V.9 Micrograph of particles in the dried turbid supernatant showing a reduction in primary aggregate size

The microstructure seen here appears to be primary scale aggregates that have been significantly reduced in size as a result of sulfate removal. This suggests that up to a critical level of washing in the system, the sulfate that is removed is primarily soluble surface sulfate. Beyond this surface sulfate level, additional washing appears to reduce the size of the primary scale aggregate to approximately 200 nm, suggesting that the role of sulfate ions is that of a bridging agent between primary particles; removal beyond a critical level in low sulfate powders appears to partially remove the bridging mechanism and cause fragmentation of the aggregate.

The present centrifugation conditions appear to be sufficient to cause sedimentation of the 1 μm units but not for the newfound approximately 200 nm units. This suggests that the primary aggregate can be attacked by a chemical means in addition to endeavors to physically rupture it. This suggests two possibilities that initial sulfate removal via washing in deionized water leads to a removal of soluble sulfate initially but eventually results in removal of intercrystalline sulfate. This also suggests that caustic additives would be highly detrimental to the viability of this material as a catalyst

support because further sulfate removal may result in smaller pores that produce a greater backpressure due to gas-flow resistance.

The powders' physical and chemical attributes have been assessed and while relatively little difference has been seen in the aggregate size at different scales for different powders, the different scales themselves correspond to particular size ranges. The greatest variations that have been observed in this process is the soluble sulfate level and specific surface area which are not thought to be necessarily independent. It is reasonable to conclude that the accompaniment of higher surface area powders exhibiting a higher sulfate level is caused by the presence of a greater number of surface sites containing unreacted soluble sulfate unconverted to titania from titanyl sulfate. The sulfate encountered by the powders in suspension appears to be soluble sulfate until a critically low level has been removed. However, it is difficult to predict and quantify this critical amount of sulfate since it is difficult to accurately quantify the total sulfate present in the system prior to washing and furthermore it is difficult to differentiate how it is divided into either surface soluble sulfate or intercrystalline sulfate. The washing sulfate may be interpreted and converted to estimate an amount of sulfate removed relative to the initial amount of powder washed; however, of greater significance is the relative difference observed in the sulfate levels between powders 1, 2, and 3 and powders 4, 5 and 6.

V.2 Determination of Aggregate Scale Yield Strength

V.2.1 Dynamic Stress Rheometry

Stress-controlled rheometry can be used to determine the state of a system as a function of two variables: the oscillatory frequency and the oscillatory stress applied. The oscillatory shear stress in particular can be useful in determining the nature of the system as a function of increasing applied stress. Upon reaching a sufficiently high particulate solid concentration, the powder particles span the fluid medium producing the network structure described in Section II.6.3.2. Upon achievement of a network structure, at a critical oscillatory stress value, the particle-particle contacts will be ruptured, and the system will be reduced from a linear elastic solid-like structure to free-flowing hydraulic units. This critical oscillatory stress value is described earlier in Equation II.51. The typical means of determining yield stress has been via elementary viscometry used to measure viscosity and attribute flow models to a system. In such a method, the shear stress is measured with shear strain rate as the independent variable. Upon fitting an appropriate rheological model to the system, the data is summarily extrapolated to ‘zero shear strain rate’ whereupon the y-intercept is characterized as the yield stress. According to Cheng⁸⁹, this is particularly pertinent to Bingham plastics and generally fluids “with a shear rate that depends on excess shear stress ($\tau - \tau_y$)”. It is further conceded by Cheng that this technique is necessary because of “the impossibility to measure the shear stress actually at zero shear rate” using viscometry⁸⁹.

In oscillatory stress rheometry, two moduli are monitored as a function of an applied stress amplitude. The ‘elastic modulus’, G' , monitors the strain of the suspension in phase with the applied oscillatory stress. Oscillations that are ‘in-phase’ cause a corresponding oscillation in the networked particulate structure and subsequently produce small strains. Strains which begin to rupture the particulate network result in strains

which are out of phase with the applied stress wave. This is achieved through use of a TA Instruments AR-1000 rheometer with an optical encoder capable of recording very small angular displacements (as small as 1 μ rad). The larger of the two competing moduli will be indicative of the nature of the suspension structure. Typically viscoelastic measurements of this sort can be performed as a function of either varying frequency or amplitude (i.e. oscillatory stress). In order to appropriately simulate extrusion conditions, stress sweeps were performed. It is anticipated that at lower oscillatory stress values, elastic solid-like behavior will dominate the system while at higher oscillatory stresses, viscous fluid-like behavior will dominate with a transition between these states occurring at some intermediary stress value whereupon a viscoelastic measurement plot would show a crossover point between G' and G'' .

Moreover, oscillation rheometry can be related to simpler rheological measurements for the sake of correlation and equivalence. Citing work by Doriswamy et al., Mas and Magnin⁹⁰ provide the following equation:

$$\eta^* (\gamma_m \omega) = \eta \dot{\gamma} \quad \text{V.1}$$

This was summarily renamed by Krieger to be the “Rutgers-Delaware” relation. Here ‘ γ_m ’ is the amplitude of the strain wave, ‘ ω ’ is the angular frequency of oscillation, and the terms on the right-hand side of the equation are the steady-state rheology terms discussed in Equation II.17. The term η^* is the complex viscosity and is given by:

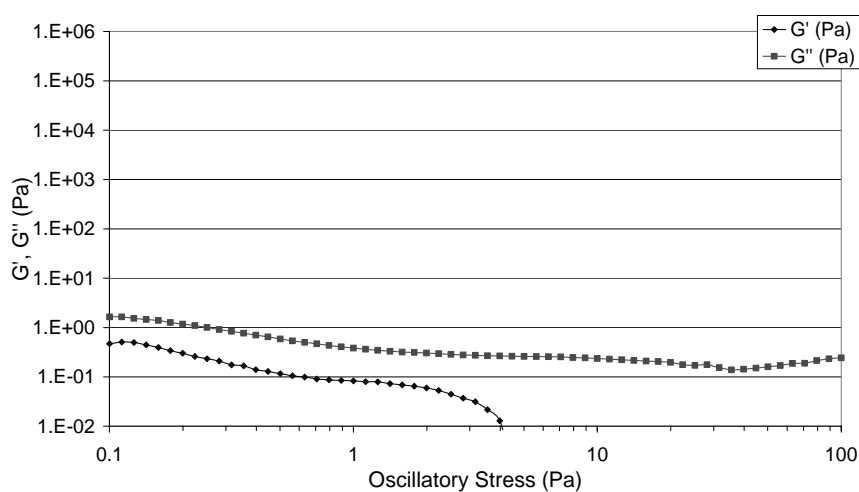
$$\eta^* = \frac{G'}{\omega} + i \frac{G''}{\omega} \quad \text{V.2}$$

Here ‘ i ’ is the imaginary number. The 1.0 Hz oscillation frequency utilized in this work becomes convenient for future manipulation of oscillation rheology data into steady-state rheology data or computation of hydrodynamic stresses as necessary. The

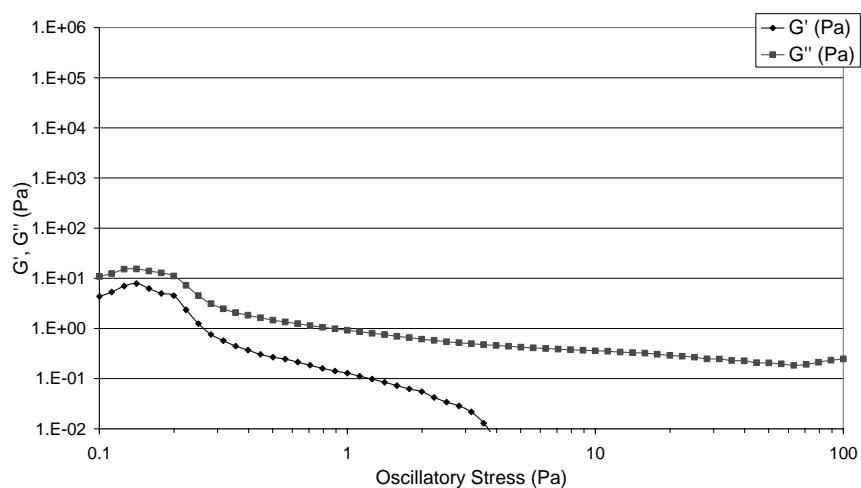
discussion provided here for these data, however, will retain consistency with oscillation rheometry variables.

V.2.1.1 Optimal Solids Concentration

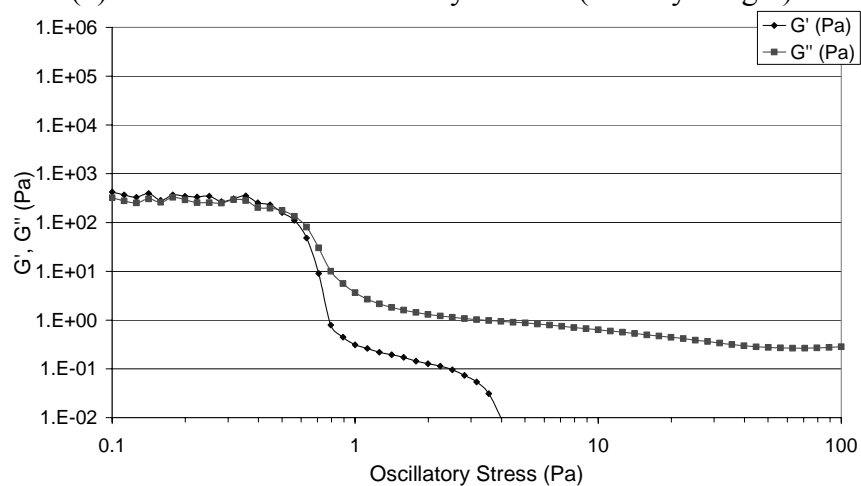
To establish a common solids loading on which to evaluate this transition, two powders were selected for trial runs of increasing solids loading until each had exhibited a sufficient linear elastic regime prior to yield. Since the yield strength and magnitude of G' (in-phase or elastic modulus) are correlated, sufficient elasticity was selected as the point where all suspensions exhibited yield points above 1.0 Pa of oscillatory stress. Furthermore, since it is hypothesized that the biggest differences will be observed between powders of high sulfate content and low sulfate content (based on the work of Rand and Fries⁵³ on KNO_3 indifferent electrolytes in nanosized alumina), the solids loading buildups were carried out on one low sulfate powder (Powder 2) and one high sulfate powder (Powder 4). The results of the investigation are presented as Figure V.10 and Figure V.11 (Powders 2 and 4 respectively).



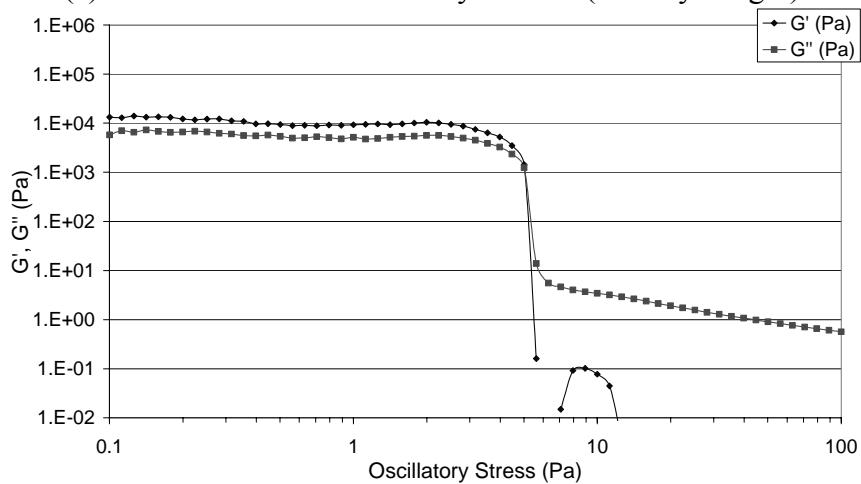
(a) Powder 2 at 2.3% solids by volume (5% by weight)



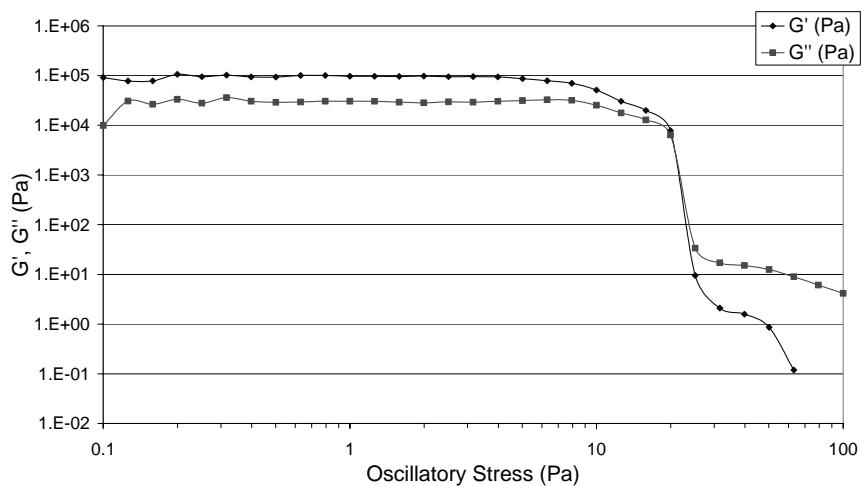
(b) Powder 2 at 6.6% solids by volume (15% by weight)



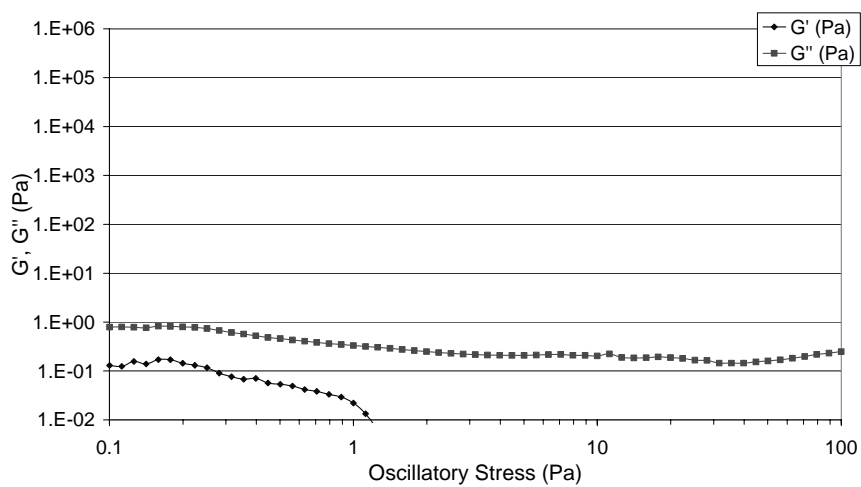
(c) Powder 2 at 10.6% solids by volume (25% by weight)



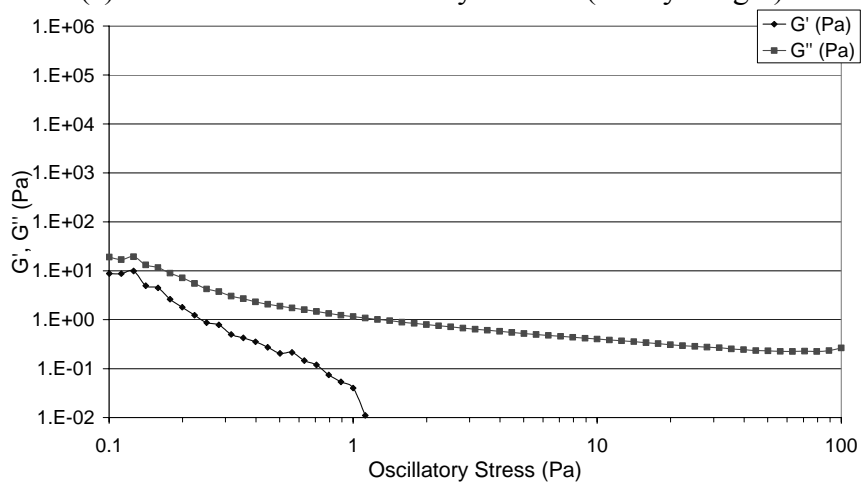
(d) Powder 2 at 14.2% solids by volume (35% by weight)



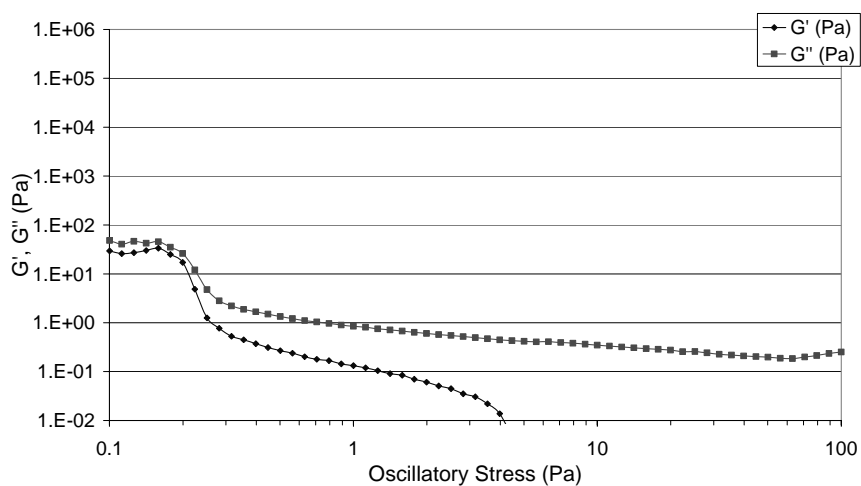
(e) Powder 2 at 17.6% solids by volume (45% by weight)
Figure V.10 Powder 2 solids loading buildups



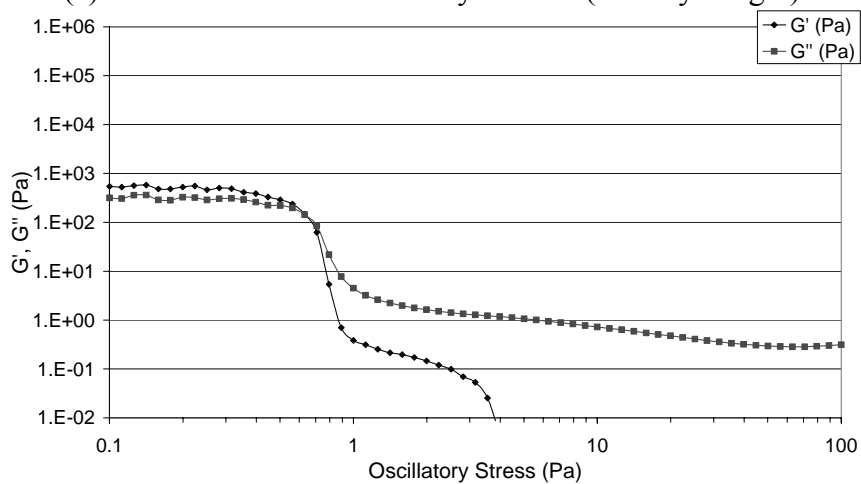
(a) Powder 4 at 2.3% solids by volume (5% by weight)



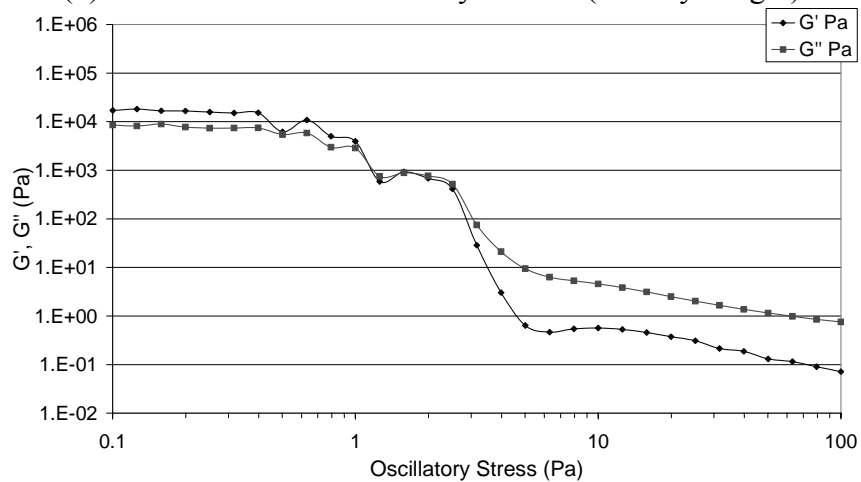
(b) Powder 4 at 6.6% solids by volume (15% by weight)



(c) Powder 4 at 10.6% solids by volume (25% by weight)



(d) Powder 4 at 14.2% solids by volume (35% by weight)



(e) Powder 4 at 17.6% solids by volume (45% by weight)

Figure V.11 Powder 4 solids loading buildups

Comparing Figures V.10(a) and V.11(a), it can be seen that 2.3 volume % solids produces a structure where the G'' value dominates the system, indicating that the system is at too low a solids concentration to establish an elastic network. The near-flat value of G'' indicates a high level of fluidity that is unaltered by any apparent yield stress.

At 6.6 volume % for corresponding Figure (b), both systems appear to begin establishing some degree of linear elasticity as evidenced by the slight increase in both G' and G'' at low oscillatory stress values. However the G'' value is still dominant for the entire range as seen by a repetition of the near-flat values of G'' at higher stress pulse values indicating a similar degree of fluidity in the suspension. At 10.6 volume %, both systems appear to have begun establishing linear elastic regimes. G'' appears to still be prevalent at low oscillatory stress values, and the fluid elasticity is still very low. Additionally, powder settling effects were observed for each system at 10.6% suggesting that despite the apparent onset of elastic behavior, this particular solids concentration would represent a poor measure of powder properties due to insufficient solids loading to inhibit settling. At 14.2% the settling effects were partly mitigated by the increased solids concentration yet were still present. Moreover, each system appears to have represented the increase in elasticity with solids loading by the continual increase in G' with solids concentration, corroborating the use of G' as a measure of suspension elasticity. At 14.2% the observed crossover between G' and G'' does not appear to occur for both systems simultaneously above 1.0 Pa.

The prevalence of G'' at higher oscillatory stress values again results in a saturation value between 1.0 and 0.1 Pa for (a), (b), (c) and (d) suggesting a state of full fluidity is achieved for G'' values in this range. It is also possible that with settling

effects potentially obscuring the measurability of powder properties at this concentration and with the stress values being ramped as a function of increasing time as well, the G'' values observed at this concentration where settling effects occur may be indicative of the fluidity of the solvent (here deionized water) with a lack of significant measurable contribution to fluid properties from the powder. Moreover, the measurement of G' values below 0.01 in these figures indicates that the degree of elasticity retained at higher stress values is either insignificant or is immeasurably low for the instrument. Ultimately, the solids loading curves appear to indicate that 17.6% by volume is the optimal common solids concentration to evaluate the transition from linear elastic solid to viscous fluid behavior and settling effects appear to be insignificant.

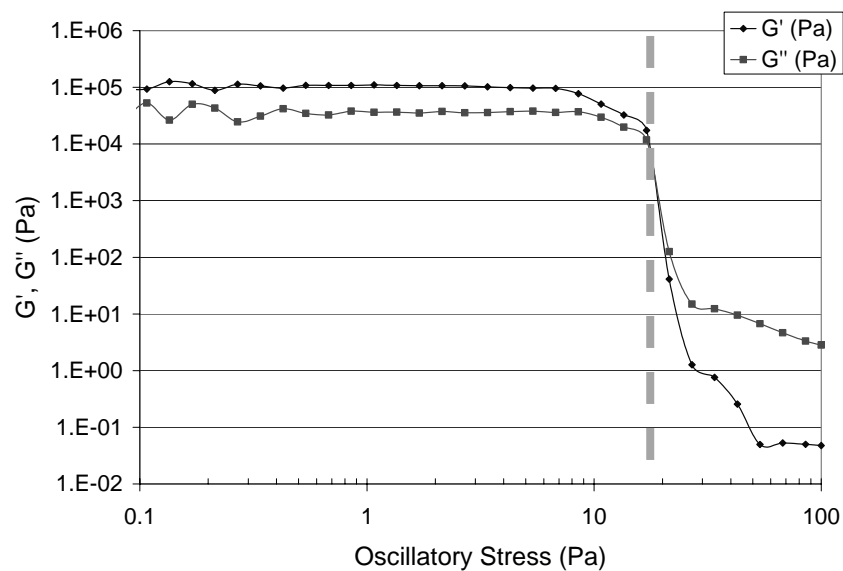
Figures V.10 and V.11 can be viewed as a kinetic study of a suspension developing elasticity with increased interparticle contact. The observable trend from Figures (a) – (e) for the two powders is the apparent interrelation between elasticity and the stresses causing a decay in the moduli of the system to solvent or steady-state values. This would appear to indicate that the strength of the network interaction in the system is largely dependent on the degree of interconnectivity suggesting the physical networking of components is responsible for the elastic and viscous behavior observed.

V.2.1.2 Variation of Yield Stresses and Linear Elastic Storage Modulus

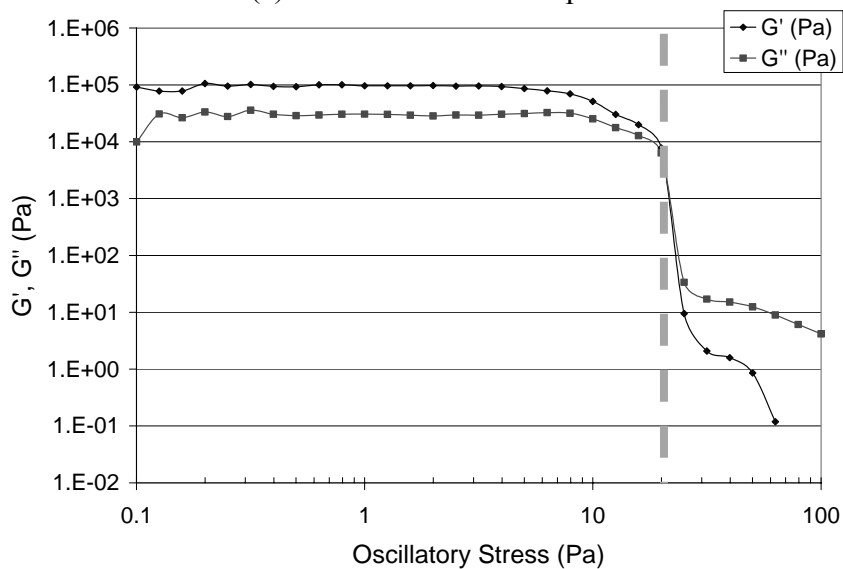
Stress rheometry of the individual powders is presented in Figure V.12(a)-(f). Each graph was assessed to determine the viscoelastic yield stress and the magnitude of G' in the ‘flat’ linear elastic regime (this is referred to by de Vincente et al.⁹¹ as G'_{VLR} for ‘viscoelastic linear region’; there does not appear to be a standard nomenclature for this

and is defined by convenience). These results are summarized in Table V.2. The suspension yield stress was determined as the aforementioned ‘crossover’ point between G' and G'' . This is a contentious point as other common rheological techniques suggest a method of inferring a ‘yield stress’ from data acquired (if it is at all believed to exist)⁸⁹. By contrast, the term referred to here as ‘yield stress’ determined from the stress sweep is more commonly referred to as the limit of linearity. The yield stress for this investigation is defined explicitly as the stress value corresponding to a transition from elastic solid-like behavior to viscous fluid behavior. Since the measure of these states is believed to be reflected by measurement of G' and G'' , the crossover point of these two variables is argued to signify this transition.

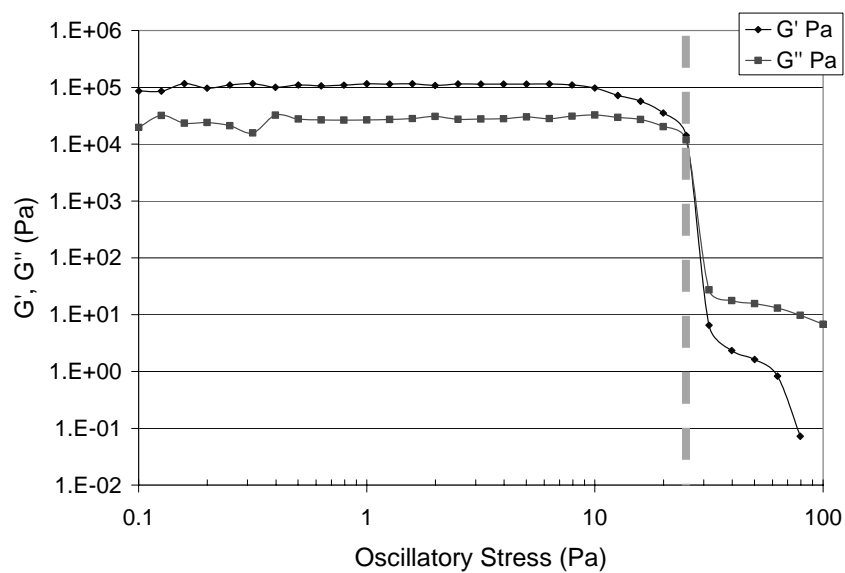
The average elastic modulus in the linear elastic regime was taken as the average value of G' for all stresses prior. Powders 1, 2, and 3 all exhibit a relatively high value for the elastic modulus in the region of the curve where G' dominates; conversely powders 4, 5 and 6 exhibit significantly lower values of both the yield stress and the average G' value in the linear elastic regime. Per Equation II.51, the yield stress observed for the rupture of a networked particulate suspension exhibits a linear relationship with the binding energy, E_a , of network constituents suggesting that with all other parameters, including solids concentration, being equal, the principal difference seen in the powder suspensions is a strong gradient in the binding energy of network constituents. Further investigation via Equation II.52 shows this term to be dependent on the number of ‘links’ as well as the binding energy per link⁵⁰.



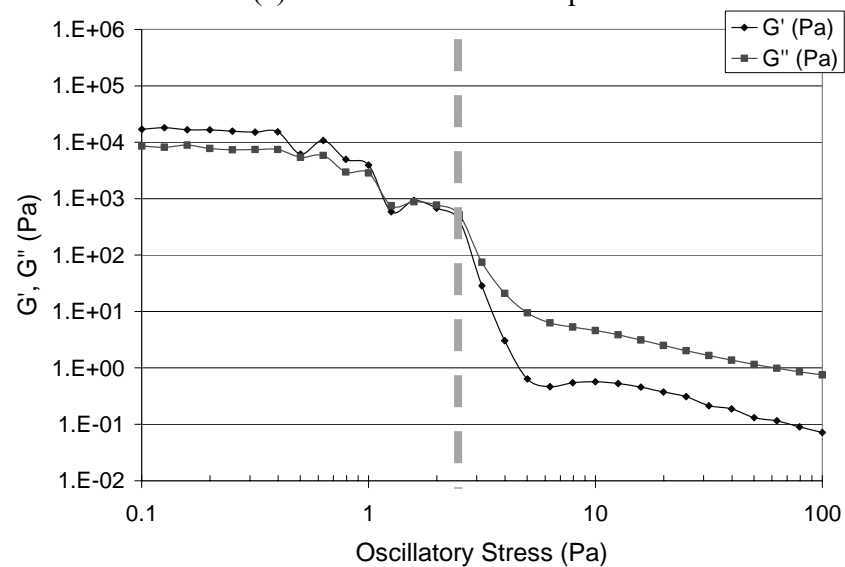
(a) Powder 1 stress sweep



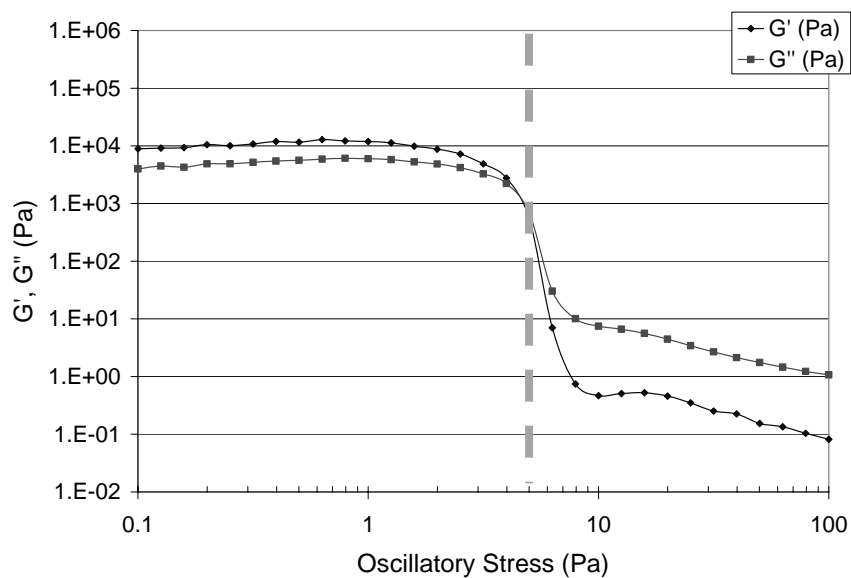
(b) Powder 2 stress sweep



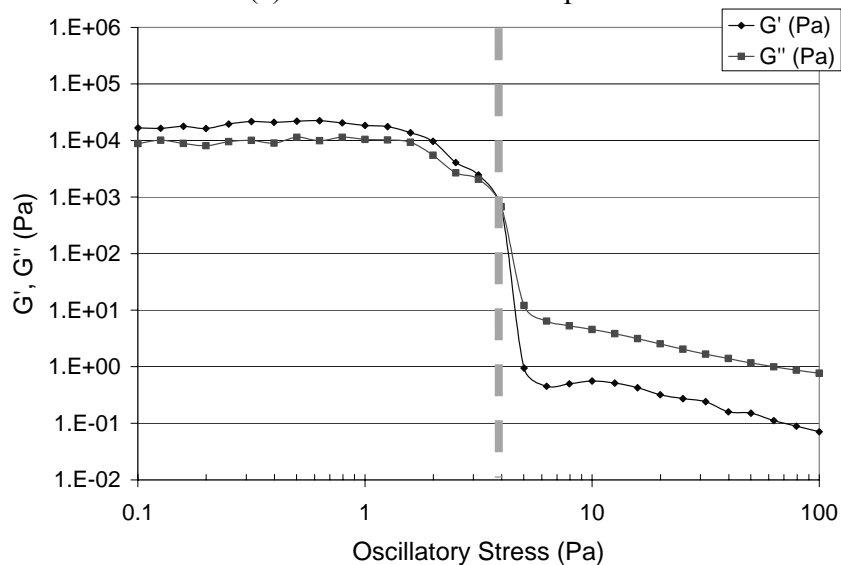
(c) Powder 3 stress sweep



(d) Powder 4 stress sweep



(e) Powder 5 stress sweep



(f) Powder 6 stress sweep

Figure V.12 Stress-controlled rheometry measurements at 45% by weight for the various powders (Dashed line indicates yield stress)

Powder	Suspension Yield Stress (Pa)	Linear Elastic G' (Pa)
1	17	35924
2	20	94474
3	25	111118
4	3	16363
5	6	10647
6	4	19227

Table V.2 A summary of measurements obtained via stress-rheometry

Initially it had been convenient to assess a system undergoing non-Newtonian effects via the Krieger-Dougherty or Einstein equations provided the systems were comprised of non-interacting spherical units. The strong dependence of sulfate on elasticity and yield stresses observed in these systems strongly suggests varying levels of interaction leading to a dismissal of their equations for this scenario. In investigations by Rand and Fries as summarized earlier, it was argued that the concentration of indifferent electrolytes affected the elasticity of a suspension because the size of the ‘effective particle’ (i.e. the diameter formed by the particle and its corresponding electrical double layer thickness) was affected. Specifically they found that an increased amount KNO_3 indifferent electrolyte in suspensions of nanometric alumina reduced the value of G' . A suggested illustration is provided in Figure V.13 while a comparison in this system is plotted in Figure V.14. In consideration of this, re-examination of Equation II.51 suggests that differences could be more attributable to the term, a , in the equation. This can subsequently be rewritten as:

$$\tau_B \propto a^{-3} \quad \text{V.3}$$

Initially it appears that the arguments of Rand and Fries contradict arguments presented in the network model as the former contend that the dependence of yield stress on particle size (taken from Rand and Fries’ arguments to mean ‘effective particle size’) is actually direct and not inversely cubed as suggested by the latter. This means that a greater effective particle size actually increases the bulk yield stress because of the greater amount networking introduced into the suspension. This can be resolved with the arguments of the network model by arguing that the increased effective particle size for

low sulfate suspensions appears to affect the E_a term not necessarily by affecting ε_a but rather by increasing n_L , the number of links. A larger effective particle size produces a greater probability of particle-particle contacts through an increased volume fraction, since the greater effective size results in a larger effective volume. This further serves as a secondary means of resolving the apparent contradiction by arguing that the term, ϕ , may not be effectively constant for all samples. It appears that the network model requires this modification to be fully applicable for this system as the models introduced by Rand and Fries are more consistent with the high levels of soluble ionic content present in the system^{50,53}.

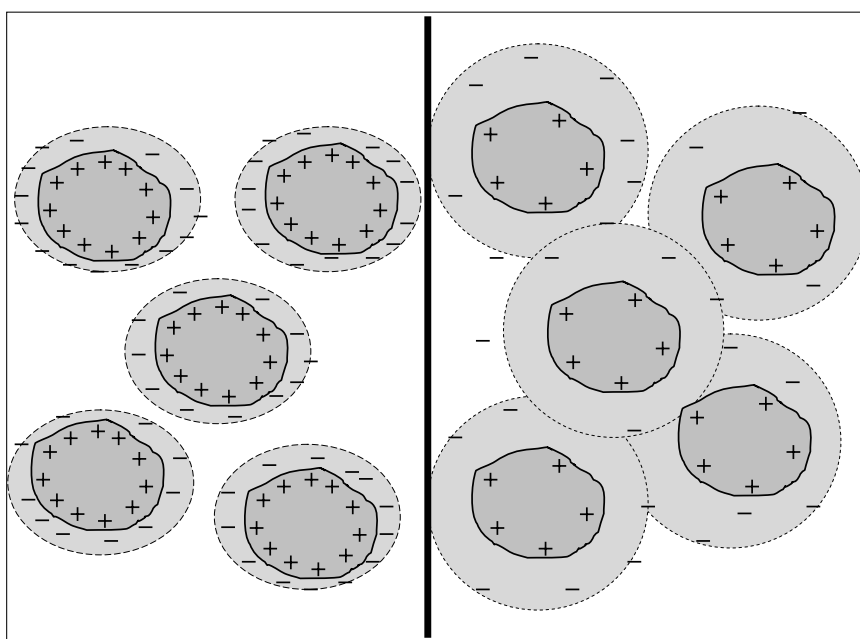


Figure V.13 Illustration of the reduced networking between powders of greater (left) soluble ion content and greater networking due to lower soluble ion (right) content caused by broader double layer interaction

Further corroborating this argument is the difference in the width of the ‘aggregate breakdown’ regime. All six powders initially exhibit a certain degree of ‘bowing’ in the values of G' and G'' as seen by the initial decrease in the moduli prior to the crossover point. This suggests the onset of unrecoverable strain in the system or

strain caused by initial yielding of the weaker aggregates. This suggests a distribution in aggregate strength, but it is difficult to distinguish on this criterion alone since the six powders appear to equally exhibit this trait in their stress-rheometry curves. Another possibility is that the oscillatory shear stress applied on the system is high enough to cause a sufficiently large strain in the system whereupon the 3 second gap between applied stress pulses is insufficient to recover the elasticity in the system. Specifically with regards to the yield regime, it is notable that lower sulfate powders all appear to exhibit a more discrete yield regime whereas the higher sulfate powders exhibit a broad yield regime. This corroborates the lower sulfate powders' exhibiting a greater degree of interconnectivity and elasticity; by contrast it is possible that the mitigated degree of 'effective crowding' in the higher sulfate powder suspensions suggests more random interparticle interactions.

The overall suggestion of Figures V.7-V.12 is that titania powders of lower sulfate content would be undesirable candidate feedstock powders for extrusion since it appears that the powders exhibit a higher yield stress; this would warrant a greater concentration of additives which would diminish throughput by lengthening the process times to compensate for burnout of the increased additive content. Rheological measurements are complex because they are highly susceptible to factors influencing the overall fluidity of the suspension such as temperature or electrokinetic parameters. In investigations of the strength of interactions within secondary and higher order aggregation stages, rheology appears to be useful in indicating the difference in physical networking between what appear to be 1 μm units at oscillatory shear stresses ranging from 3.0 to 27.0 Pa. The stresses utilized appear to cause a rupture in networking of

higher order aggregate constituents. Van de Ven and Hunter³⁰ have postulated that the act of rupturing a floc initially entails imparting elastic energy into the system to stretch the bonding between network constituents by a distance of ‘tenths of nanometers. It is possible that this ‘stretching’ is observable in the stress sweeps as the ‘unrecoverable strain’ observed in Figures V.7-V.12. Another possibility may include the stretching and reshaping of the aggregate volume to accommodate subsequent fracture by reordering the aggregates as a series of doublets to be ruptured. Van de Ven and Hunter further suggest possibilities of fluid movement within the porous disordered aggregate structure which may also account for the onset of strain.

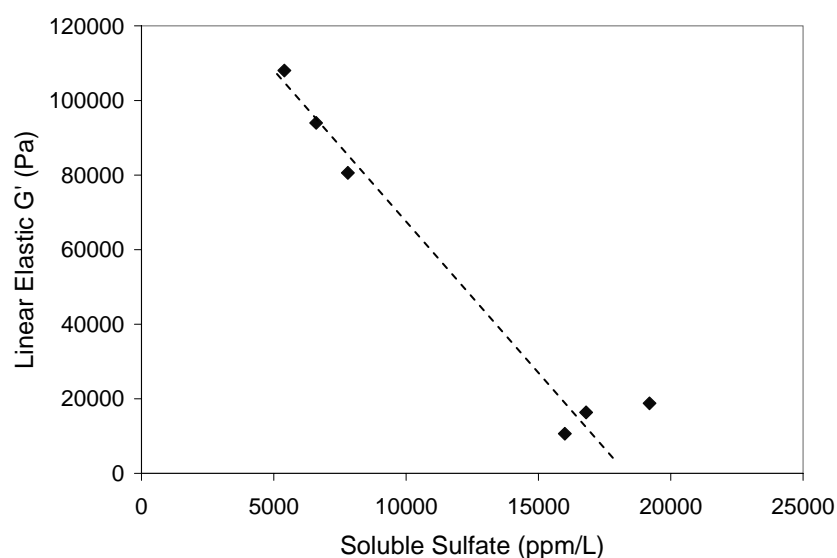


Figure V.14 Comparison of Suspension Storage Modulus (G') Prior to Yield with Soluble Sulfate Level of the Powder

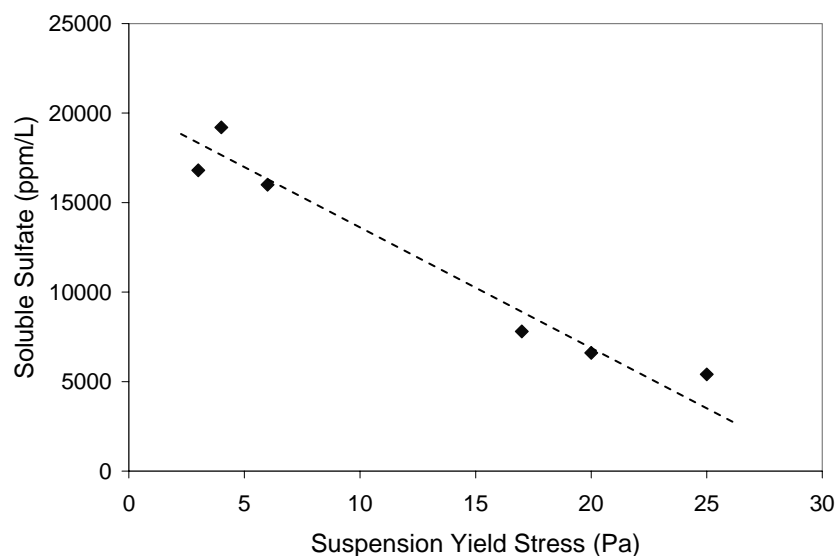


Figure V.15 Comparison of Suspension Yield Stress (τ_Y) with Soluble Sulfate Level of the Powder

Figure V.15 plots the yield stress of the powder suspensions against their respective soluble sulfate levels. It appears that the soluble sulfate is serving as this system's corresponding indifferent electrolyte and altering the size of the effective particle. Furthermore, it can be argued that for the high sulfate powders, powders 4, 5, and 6, it follows those systems of weak overall elasticity as seen via their corresponding G' values in the linear elastic regimes will require a lower stress for fracture the network into its free-flowing constituents.

Another consideration must be suspension in rheological measurements must be pH. In evaluating a magnetorheological fluid of cobalt ferrite, de Vincente et al.⁹¹ found the isoelectric point of the fluid to occur at a pH of 6.2. Evaluation of the fluid via oscillatory rheometry at a pH of 3, 6.2 and 8.6 to reflect different surface properties and surface potentials found that the stress sweep performed at the isoelectric point yielded the largest overall G' values. Their results are attributed to the removal of electrostatic repulsion forces at the isoelectric point resulting in rapid coagulation occurring. With the

strong variation in sulfate observed in the titania system investigated, a potential concern may be the influence of the sulfate on pH and ultimately as a means of obscuring the rheometry. However, based on Figure V.8, in spite of the strong sulfate variations of Figure V.7, the soluble sulfate level in the first wash cycle (which is argued to be closely reflective of the sulfate gradient encountered in the various suspensions via stress sweeps) the pH does not appear to exhibit equally similarly strong gradients by remaining between 1.5 and 2. This could be a potential concern if the reported isoelectric point of anatase fell within this range; however, Patton and Reed report the isoelectric point of anatase to be approximately 6, suggesting that the suspension pH is sufficiently removed from the IEP whereupon extraneous aggregation and coagulation effects can be considered negligible^{38,39}.

The reduction of these systems to free-flowing units from highly aggregated systems is typically deduced or inferred and rarely visually observed. In an attempt to visually distinguish these states, samples of the suspension both in the linear elastic regime (prior to yield) and immediately upon yield were withdrawn via the aforementioned technique and immediately immersed in liquid nitrogen. In order to verify that the time between withdrawing the sample and freezing it was sufficient to retain its free-flowing structure, time sweeps were performed on Powders 1 and 6 to determine the buildup of elasticity after a pre-shearing strain was induced. These results are provided in Figures V.16 and V.17. The pre-shearing strain is intended to mimic the strain encountered once the limit of linear viscoelasticity is exceeded.

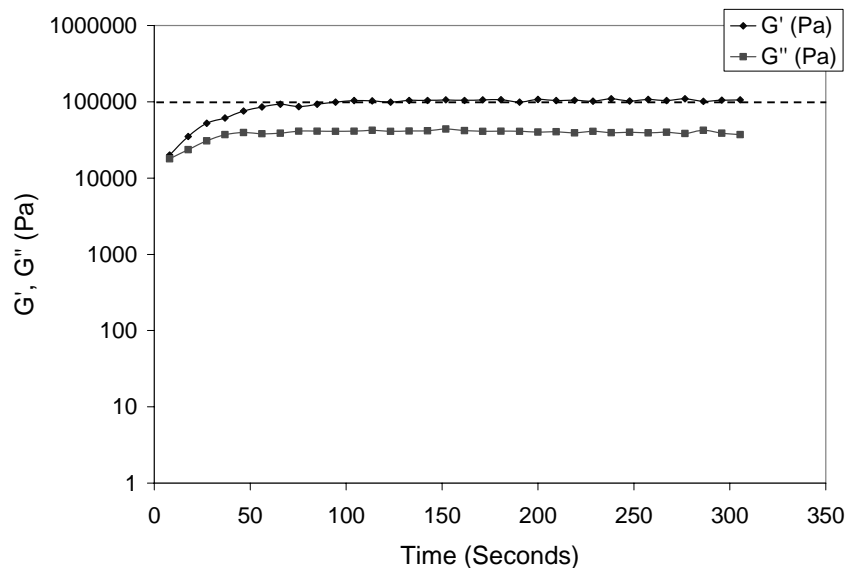


Figure V.16 Time sweep for 45 weight % suspension of Powder 1 at 3-second pulses of an oscillatory stress value of 5.0 Pa.

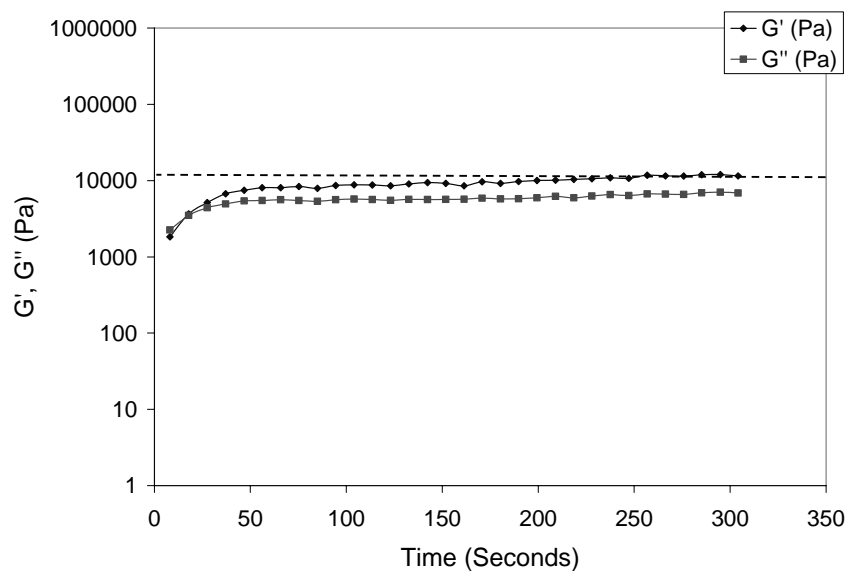
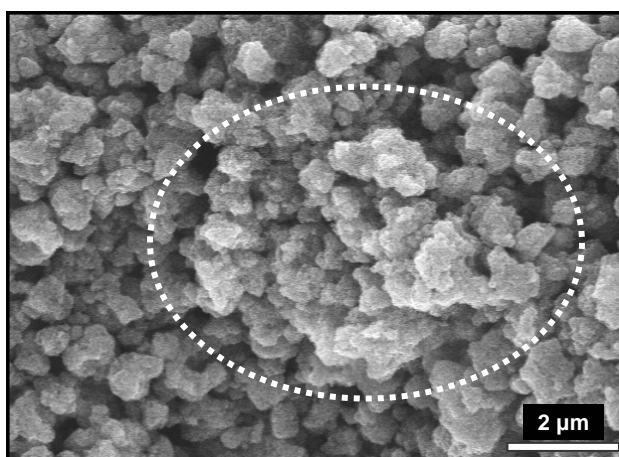


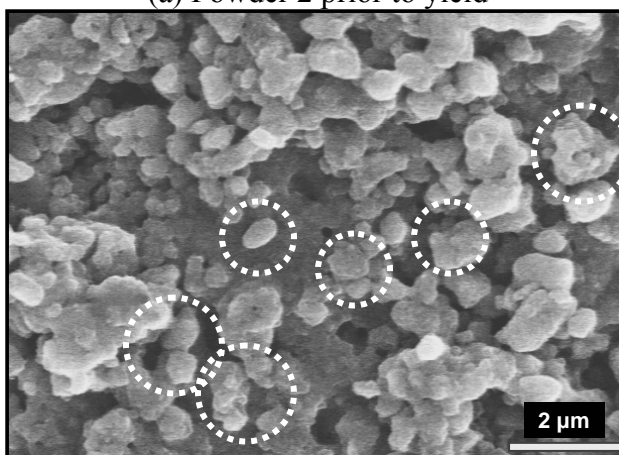
Figure V.17 Time sweep for 45 weight % suspension of Powder 6 at 3-second pulses of an oscillatory stress value of 3.0 Pa.

The dashed lines show the steady-state value of G' in the linear elastic regime as previously measured. The emergence of G' to a greater value than G'' indicates that the system has regained its elastic behavior after being pre-sheared at an angular velocity of 10 radians/sec. This appears to be true for both powders, which suggests that for both

high and low sulfate powder systems a significant amount of the elasticity is regained. Moreover, both systems appear to show that the time required for elasticity to be regained is of the order of tens of seconds whereas the suspensions were frozen within several seconds of being withdrawn from the suspension. With the time-buildup verifying the state of the system at both events upon withdrawal, this technique was utilized to evaluate Powders 2 and 4. Micrographs of these suspensions are shown in Figures V.18 (a) and (b) and V.19 (a) and (b) respectively.

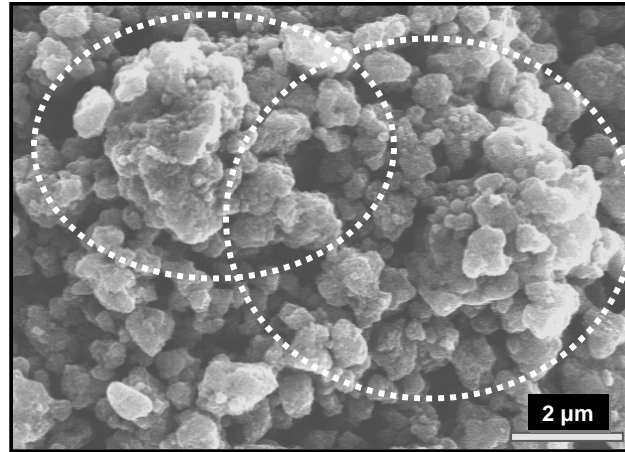


(a) Powder 2 prior to yield

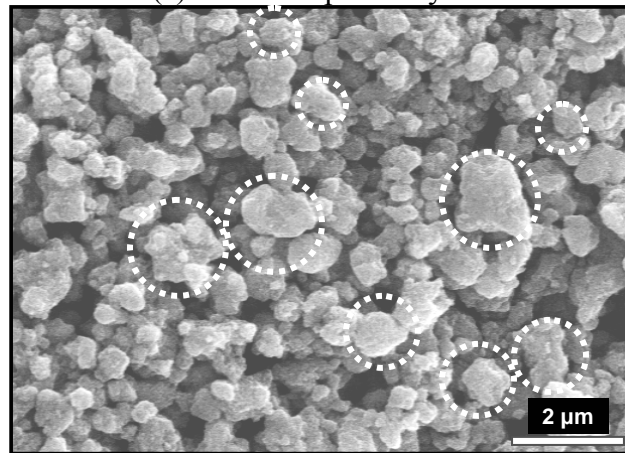


(b) Powder 2 upon yield

Figure V.18 Powder 2 at different stages of the stress sweep



(a) Powder 4 prior to yield



(b) Powder 4 upon yield

Figure V.19 Powder 4 at different stages of the stress sweep

The micrographs in Figures V.18(a) and V.19(a) appear to show a densely aggregated structure prior to yield. This is seen by a large amount of what appear to be particle-particle contacts clustered into a dense assemblage. This structure seems to exhibit what can potentially be described as a network comprised what have earlier been described as secondary scale aggregates. This structure appears to correspond to the network structure described earlier.

By contrast Figures V.18(b) and V.19(b) appear to show a greater amount of individual free-flowing units approximately 1 μm in diameter. There appears to be a reduced amount of particle-particle contacts and a greater presence of individual units.

The suggestion based on these micrographs is that stress-controlled rheometry results in the rupture of the network structure of the particulate suspension per initial speculation. However, the following additional micrographs in Figure V.20 bear consideration for the suspension upon yield.

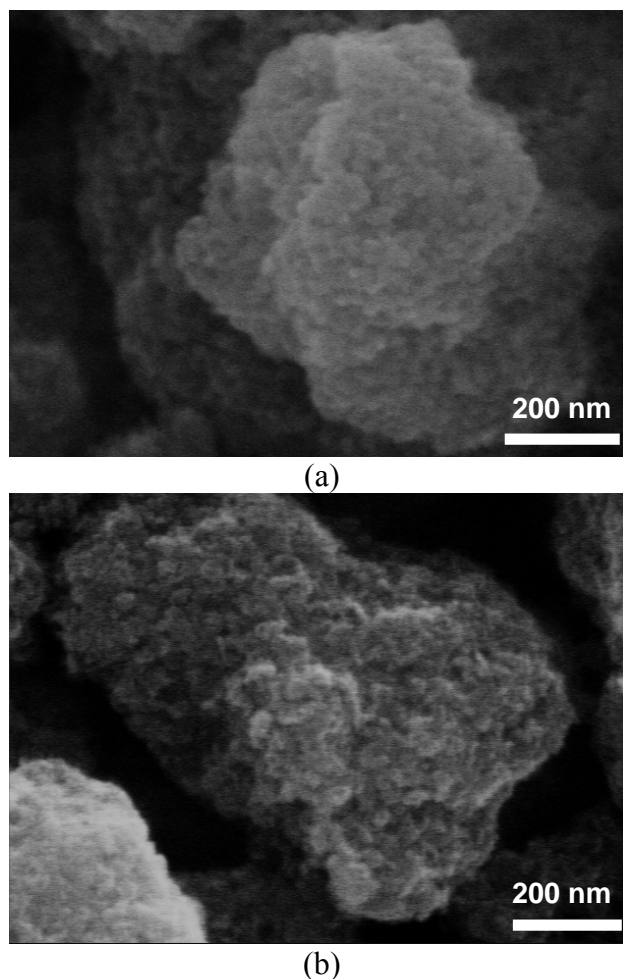


Figure V.20 The suspension sample upon yield for (a) Powder 2 (b) Powder 4

These micrographs appear to indicate that the primary scale aggregates in the system are still intact, suggesting that the network is spanned not by the fundamental primary particles but rather by primary aggregates. The subsequent rupturing of the network ruptures bridging between these aggregates but does not appear to affect the bridging between primary particles. With the micrographs showing intact 1 μm network

constituents rearranged it appears that the ‘links’ between particles appear to be ruptured at this observed yield stress. This indicates that the nanosized titania investigated correspond to the “weak-link” regime described by Wu and Morbidielli upon viscoelastic yield indicating a value of α closer to 1.0 for these suspensions. As such, it is suggested that the overall elasticity of an extrusion paste is predominantly controlled by the elasticity of the inter-aggregate links.

It would appear as though the ‘yield stress’ as measured via oscillatory rheometry is the stress required to rupture doublets on ‘links’ in the network through imparting specific hydrodynamic stresses on the fluid causing the constituents of the network to dissociate into units small to flow as a function of the applied stress. It appears a reduction to intact primary scale aggregates is a sufficient condition to cause fluid flow.

V.2.2 Compaction Curves

Powder compaction was performed on each of the powder samples to establish upper limit boundary conditions for stability of the aggregate. Compaction curves for each of the six powders are shown in Figure V.21-V.26. Compaction of each powder sample yields densities of approximately 60% theoretical density based on computations from on-line monitoring of powder compaction. In all instances of compaction it can be seen that the pressure utilized is sufficient to produce what appears to be a transition between Stage I and Stage II of the typical compaction curve. There appears to be no transition to Stage III evident suggesting that 750 MPa is insufficient pressure to produce rearrangement of the primary particles believed to occur in Stage III. It is possible that the system’s primary particles possess a sufficiently high strength to withstand

deformation at this pressure. It is also possible that the granule rearrangement has not been fully optimized to proceed to the next stage of compaction. However, the pressure utilized appears to be sufficient to see a transition to Stage II and subsequently to fragment the aggregates^{64,72,73,74,75,76,77}.

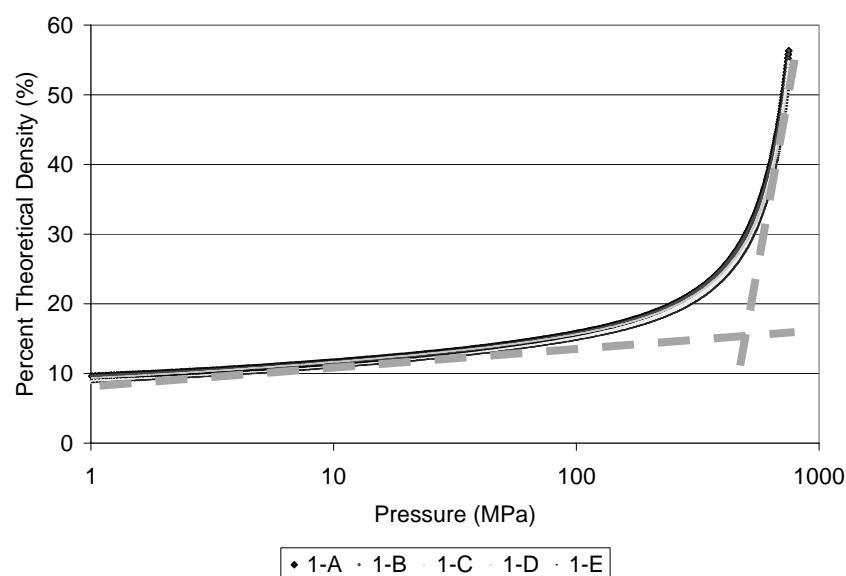


Figure V.21 Compaction curves generated for Powder 1

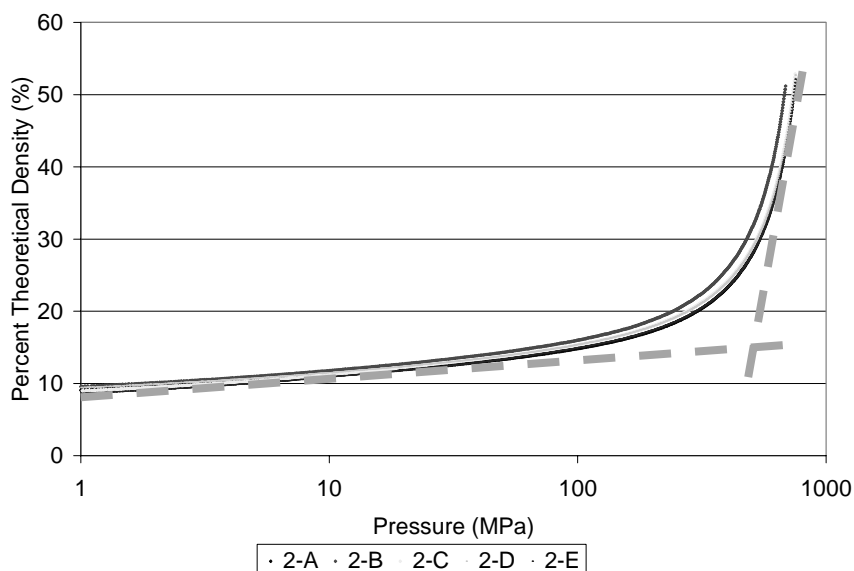


Figure V.22 Compaction curves generated for Powder 2

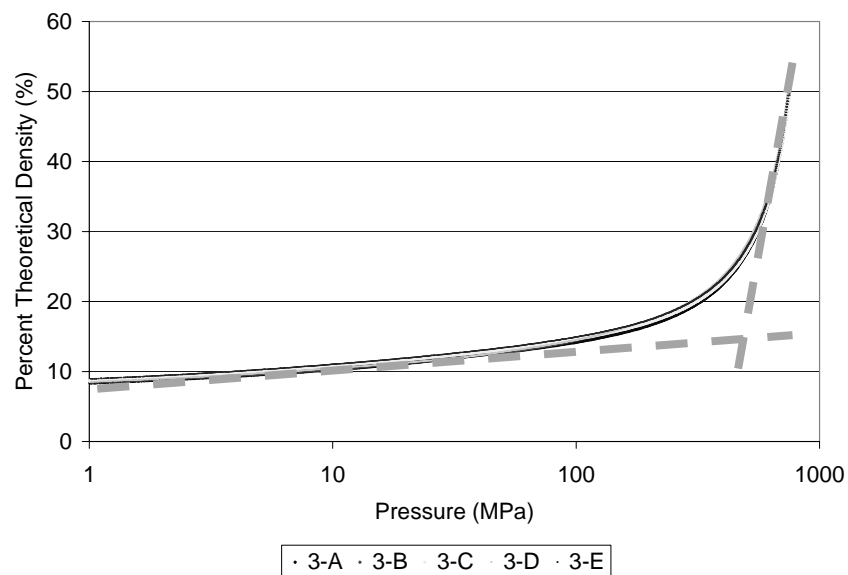


Figure V.23 Compaction curves generated for Powder 3

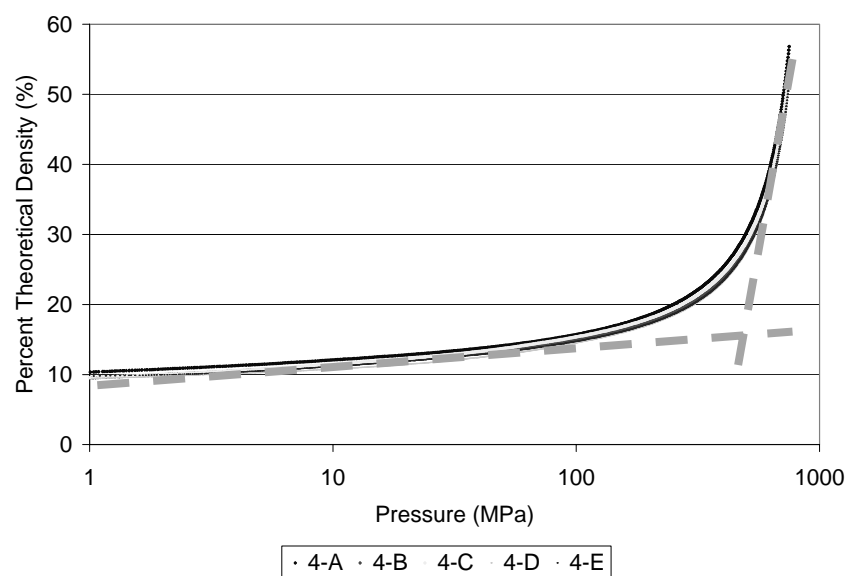


Figure V.24 Compaction curves generated for Powder 4

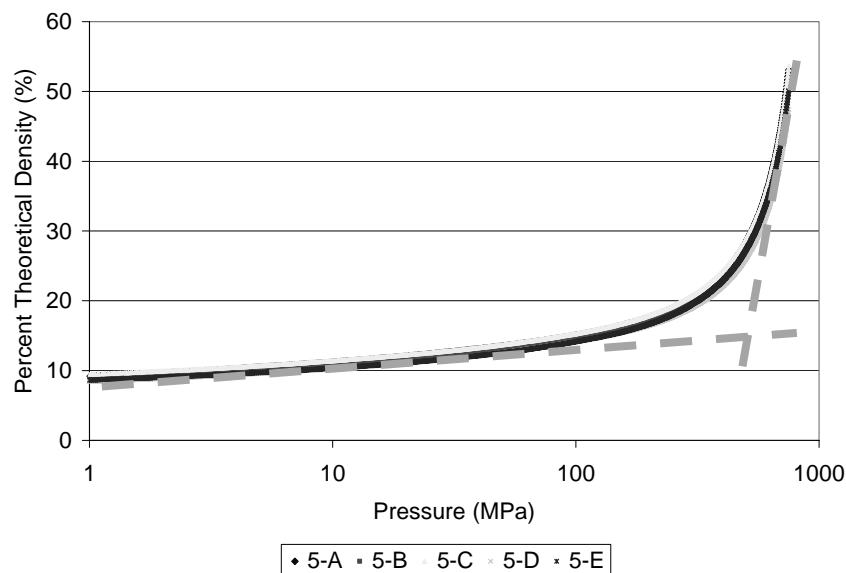


Figure V.25 Compaction curves generated for Powder 5

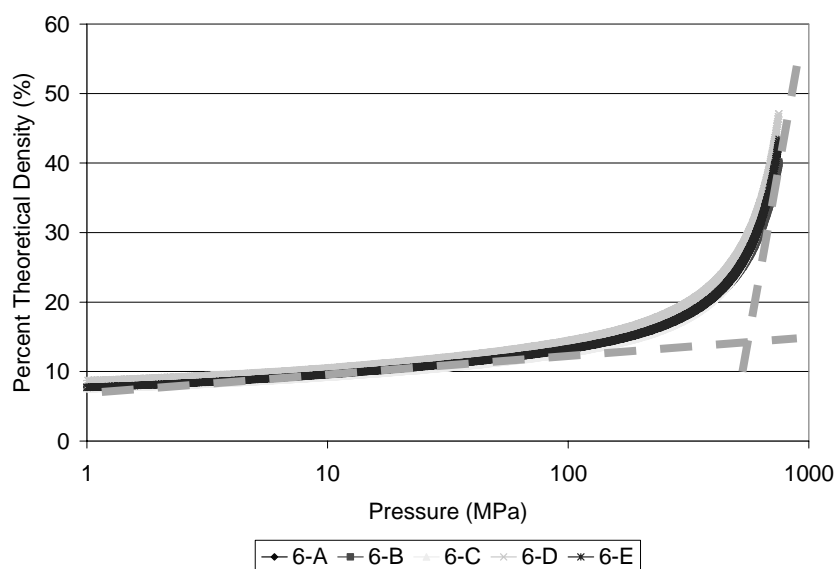
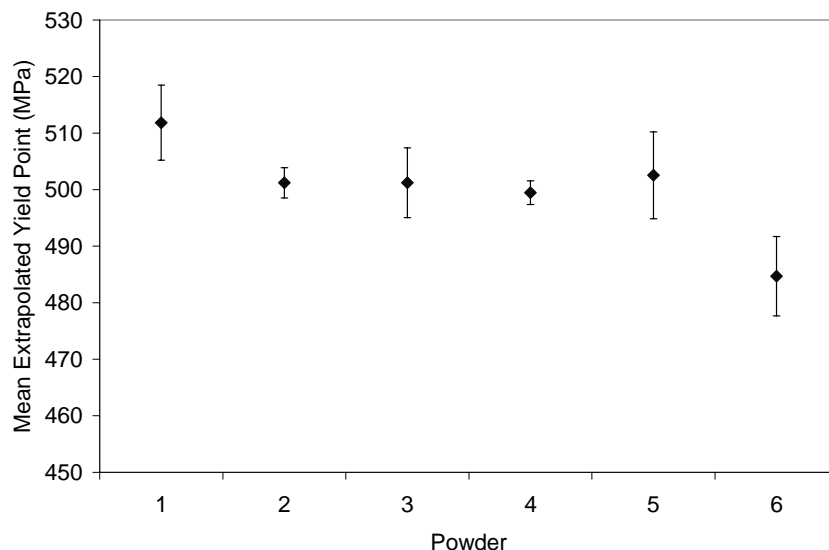


Figure V.26 Compaction curves generated for Powder 6

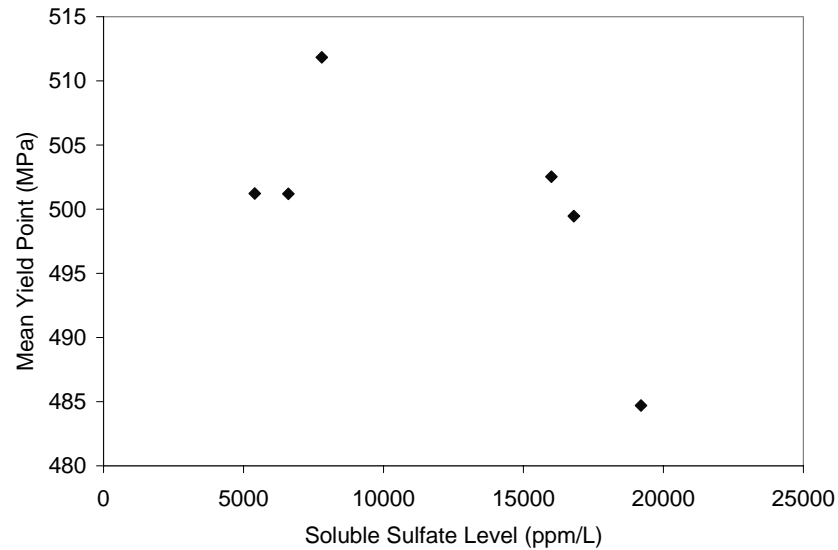
Calculations of the average extrapolated yield point for each powder are plotted in Figure V.27a) ± 1 standard deviation and tabulated in Table V.3. Figure V.27b) plots the extrapolated yield points against powder sulfate level. The plots of the average yield point exhibit distinct average yield points including what appear to be distinct ranges of yield points for the powder investigated. It can be argued that there is a tendency for the

higher sulfate powders to exhibit lower calculated yield points as seen in Figure V.27b), but the width of the distribution in Figure V.27a) appears to weaken this claim. It is possible that, much like earlier arguments of Kallay and Zalac²⁹ or Rand and Fries⁵³, the presence of a polar solvent medium is necessary to exploit the variation in soluble ionic species. The dry compaction process does not show as dramatic a disparity as a function of the powder variant investigated.

Another possibility is that the sulfate variation among the different powders is significant only at orders of aggregation higher than the scale being investigated. Considering the washing studies documented earlier where washing of Powder 3 eventually resulted in a reduction of the overall size of primary scale aggregates. It was suggested that washing at that level was a removal of intercrystalline sulfate level among 20-40 nm particles. The soluble sulfate level present on the surface of the 1 μm primary scale aggregates is accessible via rheological techniques as soluble sulfate. The variation of sulfate within this effective unit does not appear to affect the strength of the bridging between 20-40 nm particles as strongly as the bridges between the 1 μm units.



(a) Extrapolated Yield Points via Compaction for each Powder. Error bars denote 1 standard deviation



(b) Extrapolated Yield Points plotted against Sulfate Level

Figure V.27 Extrapolated Yield Points via Compaction plotted independently and against Sulfate Level

	Sample	Calculated $\ln(\sigma)$	$\sigma_{\text{aggregate}}$ (MPa)		Sample	Calculated $\ln(\sigma)$	$\sigma_{\text{aggregate}}$ (MPa)
Powder 1	1-A	20.04	506.53	Powder 4	4-A	20.03	502.25
	1-B	20.05	511.32		4-B	20.03	501.09
	1-C	20.07	521.33		4-C	20.03	497.99
	1-D	20.05	508.16		4-D	20.03	497.50
	1-E	20.06	513.78		4-E	20.03	498.44
	Average	20.05	511.84		Average	20.03	499.46
	SD	0.011	6.64		SD	0.00	2.09
Powder 2	2-A	20.04	502.60	Powder 5	5-A	20.05	511.42
	2-B	20.03	500.29		5-B	20.04	506.89
	2-C	20.03	499.99		5-C	20.04	505.37
	2-D	20.03	498.09		5-D	20.02	494.82
	2-E	20.04	505.02		5-E	20.02	494.17
	Average	20.03	501.20		Average	20.04	502.53
	SD	0.01	2.67		SD	0.02	7.67
Powder 3	3-A	20.04	507.04	Powder 6	6-A	20.00	486.04
	3-B	20.02	494.87		6-B	19.98	476.18
	3-C	20.03	500.39		6-C	20.02	493.19
	3-D	20.02	495.71		6-D	20.00	483.37
	3-E	20.05	508.05		6-E	20.01	490.83
	Average	20.03	501.21		Average	20.00	484.69
	SD	0.01	6.16		SD	0.01	7.03

Table V.3 Calculated Yield Points in Compaction

The compaction results appear to indicate aggregate breakdown as evidenced by the transition from Stage I to Stage II compaction at pressures higher than those utilized in the rheological techniques described previously which retained the primary aggregate structure. It appears that boundary conditions can be established for secondary and higher order aggregates at 3.0-27.0 Pa and primary scale aggregates at approximately 500 MPa. This implies that knowledge of these processing boundary conditions provides information regarding the size of the unit under flow or the shear conditions necessary to preserve specific aggregate iterations.

V.3 Impact on Packing Characteristics of Various Shear Conditions

V.3.1 Tape Casting

Tape casting was utilized as a means of evaluating the state of the powder system under a controlled and applied shear through a specified casting velocity. Additionally, tape casting offered a means of comparison with stress-controlled rheometry by utilizing the same solids loading without inclusion of additives. In this manner, two different casting velocities can simulate two different states of strain on the system. In order to achieve this objective two casting velocities were employed: 0.85 cm/sec and 9.09 cm/sec. It was hypothesized that evaluation at casting velocities one order of magnitude apart would subject the system to strongly different shear profiles.

Prior to casting, modeling of the shear profile under the doctor blade was sought. A commercial Finite Element Modeling (FEM) package was utilized in a similar manner

to Nycz⁴¹ whereupon the input variables for simulation were the doctor blade height, the casting velocity and the rheological model of the system employed along with fit constants. In order to derive the latter for the system, the powders were tested via viscometry from shear strain rates ranging from 1 to 300 sec⁻¹. The viscometry for the powders is shown in Figure V.28. All powders appear to obey a power-law rheological fit. Fit parameters were determined via linear regression. A summary of these is presented in Table V.4.

The correlation coefficients all show a strong fit of the data to an equation of the form:

$$\eta = A\dot{\gamma}^{n-1}$$

All suspensions exhibit an n value that is below 1, suggesting a shear thinning behavior with increasing shear strain rate. The strongest gradients in the variables obtained in linear regression appears to come from the pre-exponential variable, A . Based on these input variables, simulations were performed on the samples exhibiting the strongest gradients in this variable, here powder 3 and powder 6 respectively. The results of the simulations are presented in Figures V.29-V.32.

Powder	A	$n-1$	R^2
1	35.784	0.1007	0.9989
2	39.311	0.1070	0.9993
3	42.228	0.1317	0.9996
4	9.319	0.1315	0.9961
5	12.431	0.1261	0.9969
6	8.271	0.1478	0.9960

Table V.4 A summary of the fit constants for power-law rheology used for the various powders

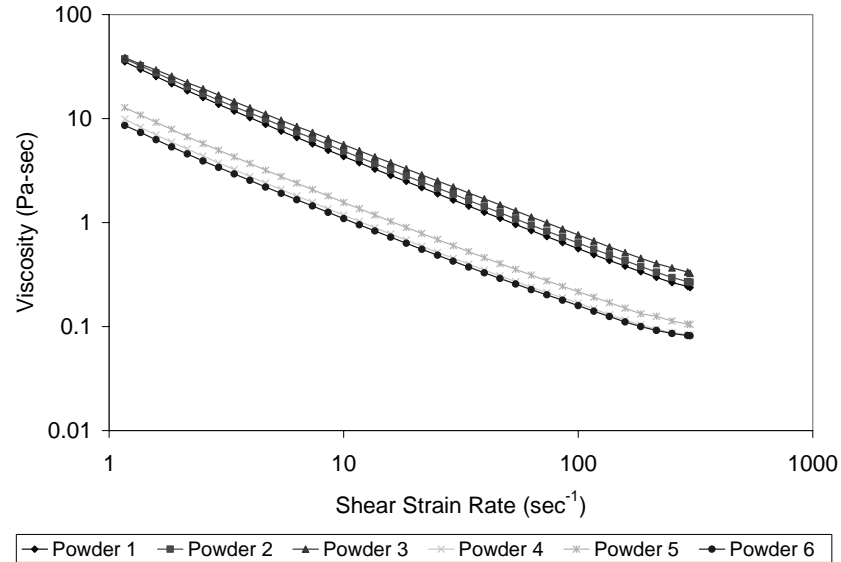


Figure V.28 Viscometry of the various powder suspensions

FEM simulations do not appear to indicate a significant difference in the shear profile undergone by each powder at a fixed velocity suggesting that the difference in rheological parameters are not large enough to merit different profiles. For differing velocities, however, there are drastically different shear profiles exhibited. As seen in Figure V.33, the microstructures seen in tape casting appear to indicate the presence of the same approximately 1 μm units rearranged under flow in tape casting corroborating the argument that under flow, a 17.6 volume % suspension of the powders appears to be reduced to its primary scale aggregates. The shear conditions utilized are insufficient to rupture the primary scale aggregates.

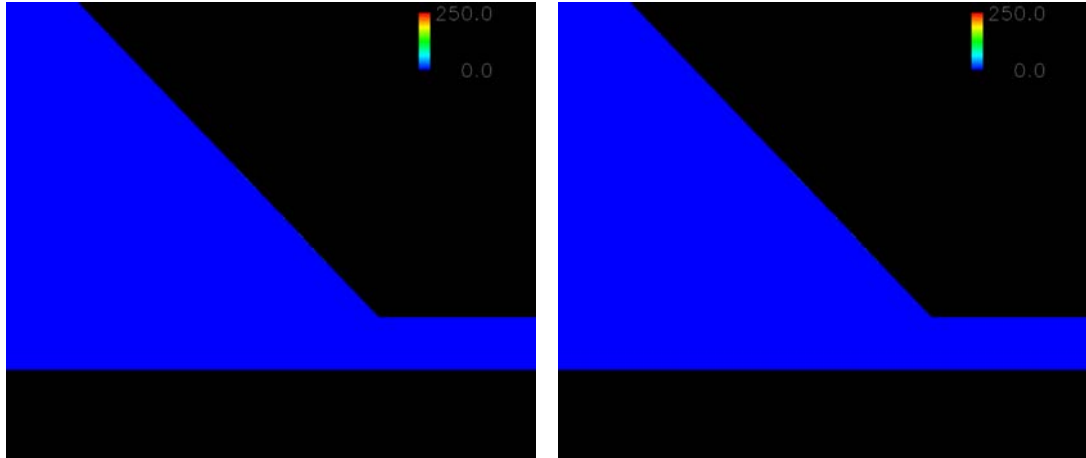


Figure V.29 (left) Shear profile of Powder 3 for 250 μm blade gap and casting velocity of 0.85 cm/sec

Figure V.30 (right) Shear profile of Powder 6 for 250 μm blade gap and casting velocity of 0.85 cm/sec

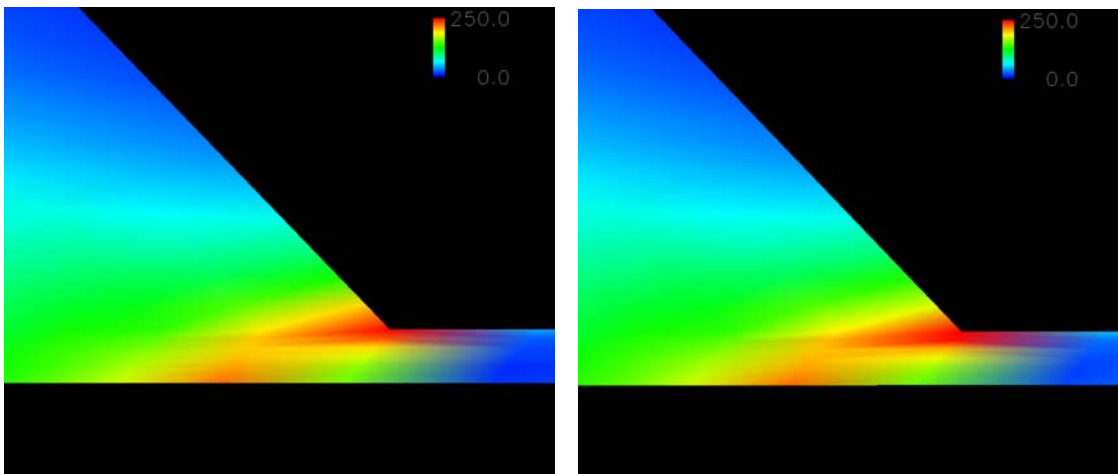
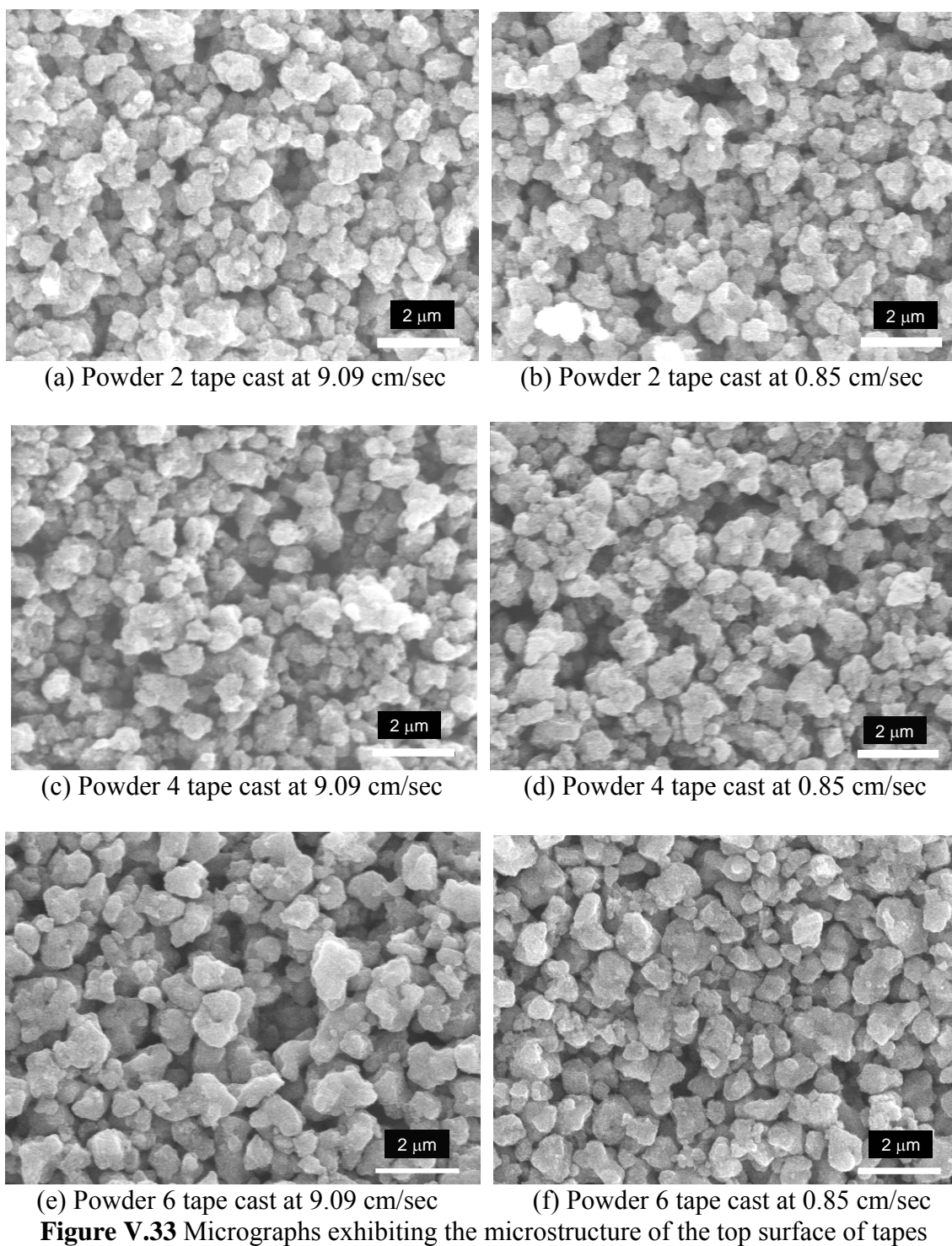


Figure V.31 (left) Shear profile of Powder 3 for 250 μm blade gap and casting velocity of 9.09 cm/sec

Figure V.32 (right) Shear profile of Powder 6 for 250 μm blade gap and casting velocity of 9.09 cm/sec



In spite of the variations exhibited between the simulation profiles of the two casting velocities two things are apparent from these results. Firstly it appears that even though the low velocity simulation indicates insignificant levels of shear relative to the

high velocity cast simulation, the ‘insignificant’ conditions are sufficient to rupture secondary and higher order aggregates. Secondly, the strong differences in the shear profiles between different casting velocities are not sufficient to indicate a qualitative difference in the resultant microstructure. If tape casting is to be utilized as an approximation to the conditions of extrusion for investigating microstructures, it appears that the pore interstices produced from this solids loading and under these casting conditions are a function of the approximately 1 μm -sized flowing intact primary scale aggregates.

V.3.2 Mercury Porosimetry

Mercury porosimetry is a technique utilized to measure pore size via manipulation of the Washburn Equation:

$$\Delta P * r = -2\gamma \cos \theta \quad \text{V.4}$$

Here ‘ ΔP ’ is the pressure gradient to force a liquid of a surface tension, ‘ γ ’, with a contact angle ‘ θ ’ to intrude into a capillary of radius r . Mercury porosimetry uses a high pressure fluid while taking into account ambient temperature so as to substitute tabulated values of θ and γ while applying a specific pressure, ΔP . The volume intruded for a specific pressure applied is correlated to the corresponding pore size in the material⁹².

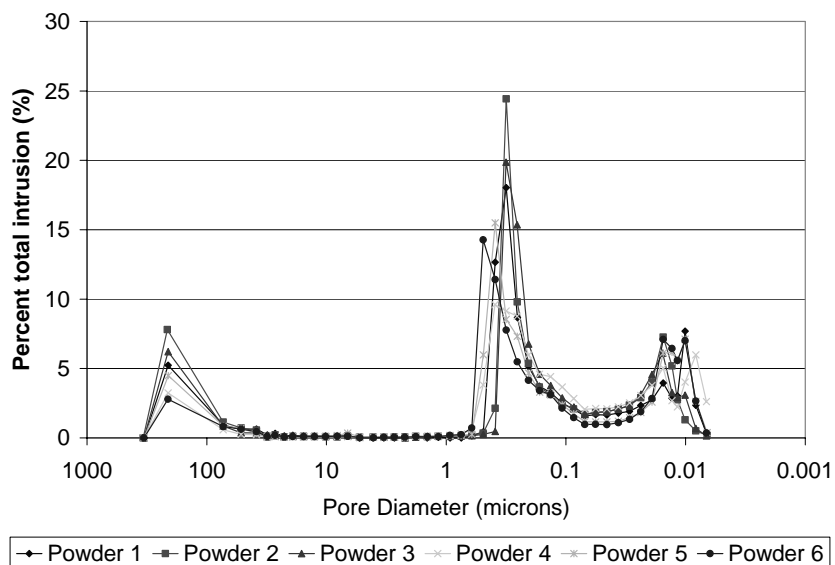


Figure V.34 Mercury porosimetry of tapes cast at 0.85 cm/sec

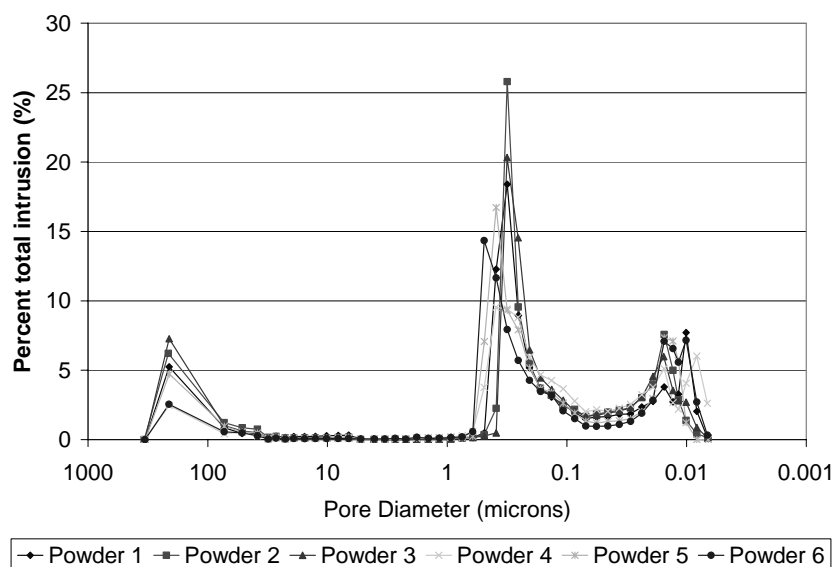


Figure V.35 Mercury porosimetry of tapes cast at 9.09 cm/sec

Figures V.34 and V.35 show results of mercury porosimetry performed on tape cast pieces of low and high velocity respectively. These plots indicate that there does not appear to be a significant amount of aggregate breakdown attained with increasing the shear strain rate of a system by 1 order of magnitude. The porosimetry on the tapes indicates that there are three peaks produced, corresponding to three diameters commonly

exhibited in the tapes of the powders. The first peak, for a pore diameter of 212 μm , corresponds to residual pores not fully eliminated via shear; the peak is believed to be misleadingly significant since the size of the pore diameter results in a significant volume of mercury intrusion in spite of a relatively low number of pores exhibiting this size.

The second major peak (and commonly the largest peak for tapes of low and high velocity for each of the six powders investigated) corresponds to a submicron pore diameter. The occurrence of this peak value ranges from pore diameters of 0.32 to 0.49 μm depending on the powder investigated. Varying casting velocities do not appear to affect the location of this peak for each of the individual powders. In particle packing, a relationship can be derived between the size of the interstices and the size of the particles assuming a roughly monomodal distribution. For spherical particles, typically this ratio varies between 0.22 for a tetrahedral configuration and 0.51 for cubic arrangements⁷⁹. Since the particle size is typically known, this technique is used to correlate the ratio measured to determine the particular packing model that a system corresponds to.

In this instance, however, the model is being used to confirm that the flowing unit in this process corroborates to a specific aggregation stage. From previous reporting, it has been established that the primary scale aggregates are approximately 1 μm in size; if that is the flowing unit, the interstices resultant in a green body will range from 0.22 to 0.51 μm in diameter. The peak diameters measured from mercury porosimetry suggest that the major flowing unit in tape casting is the preserved primary scale aggregate since the major peaks fall within the aforementioned range. plots of mercury intrusion vs. pore diameter. Moreover, it is notable that for Powders 4, 5 and 6, this peak occurs at 491, 390 and 390 nm respectively. Given the similarity in the d_{50} values observed for these

powders in Table V.1, in spite of the strong variations in powder surface area it can be argued that these three powders will exhibit rougher surface characteristics and subsequently will exhibit a lower packing efficiency. Subsequently, since packing efficiency is related to the size ratio between the interstices and particles, it can be argued that the greater degree of aggregation of these three powders produces a more fractal and irregular surface to the particle. This may explain why the powders result in a lower packing efficiency resulting in larger interstices resultant from rearrangement of the 1 μm unit for these powders.

A third peak is observed for pore diameters within the nanosized regime. This regime in some instances features multiple broad peaks suggesting a more disorganized assemblage at this length scale. It is speculated that these peaks reflect the loose assemblage of primary particles within a primary scale aggregate (referred to alternately as intraparticle porosity). The presence of these loosely defined peaks at this length scale suggests that tape casting does not attack the primary scale aggregates and the intraparticle porosity inherent in the powders upon synthesis is preserved.

By comparison, the pressed pellets have typically been inferred to attack primary scale aggregation given their use typically to measure granule strength in powder compaction. Figure V.36 plots the programs of the pressed pieces. Initially, the pellets also appear to exhibit a large peak at approximately 210 μm which is again believed to be an artifact of the lack of cohesive strength in the sample produced by the lack of a binder. However, the predominant difference seen in the pellet intrusion is the absence of the major submicron peak seen in the tapes. A minor peak is seen to occur at approximately 6 μm for the pellets which may correspond to interstices between tertiary and higher

order aggregation stages. Incremental intrusion, however, results in one other significant peak, which occurs in the nanosized pore diameter range.

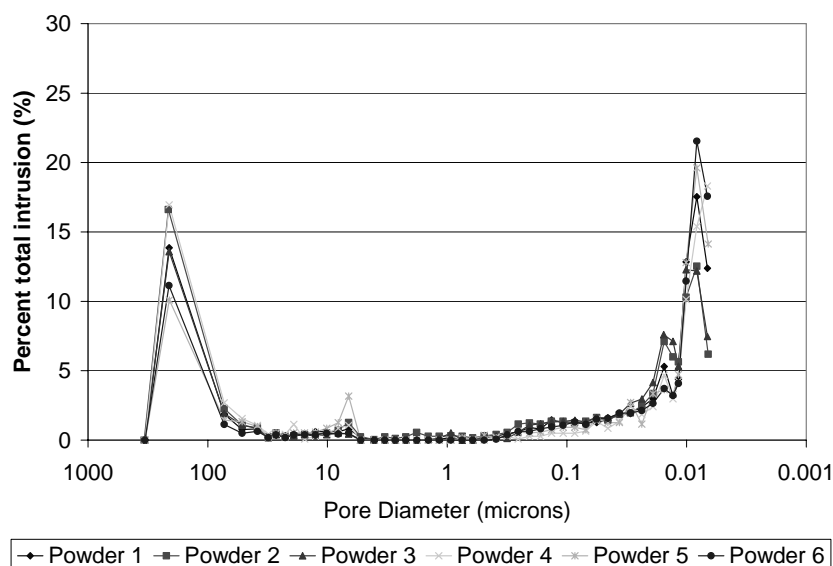


Figure V.36 Mercury porosimetry of pellets pressed to 750 MPa

In the nanosized range there appear to be two distinct peaks which may correspond to two distinct states of aggregation. One peak is seen to occur between 10 and 20 nm, suggesting that some remnants of the intraparticle porosity are retained. However, a larger peak is seen commonly below 10 nm in all pellets. Compaction curves appeared to indicate a yield point at approximately 500 MPa during compaction to 750 MPa suggesting that the pellets were pressed to Stage II of compaction, where the primary particles begin to fill the interstices between the ruptured granules. The presence of a larger peak below 10 nm suggests that the individual 20-40 nm nanocrystallites are filling the voids caused by packing of the 1 μm primary scale aggregates. Moreover, it is suggested that the presence of a peak below 10 nm corresponds to a denser packing of the individual primary particles, confirming the inferences drawn previously in compaction curves.

It can be argued that, for each of Figures V.34-36 that assumptions regarding monosized units may explain the results observed. It can be seen from as early as Figure V.1 that it can be questioned how effectively it can be assumed that the monosized approximation holds for these systems. This may explain the overall width seen in the pore distributions believed to correspond to primary scale aggregates. Moreover, it can be argued that even if the spherical monosized assumption is reasonable with this system it is likely that the non-spherical nature of the aggregates and the primary particles make the random close packed model to be the more appropriate model for consideration. However, because of the nature of the random close packed model no specific interstice to particle ratio can be acquired.

To resolve this, it is argued that since the random close packed model yields a packing efficiency that is intermediary with respect to the aforementioned cubic and tetrahedral models (64%), it can be inferred that while there is an expected distribution of pore sizes resulting from coordination of units of a specific size, these pore sizes will also be intermediary with respect to the ratios of the cubic and tetrahedral models. In consideration, the pore sizes observed via mercury porosimetry for those corresponding to sizes attributed to primary scale aggregate reordering fall within the expected values.

It should be noted for the purpose of this investigation that the particle packing models rely on assumptions of an approximately spherical configuration or packing configurations based on particles exhibiting similar aspect ratios to spheres. Based on qualitative observations via SEM the particles do not appear to exhibit specific anisotropy for a particular length scale (if exhibiting any specific shape at all) so it is believed to be reasonable to use the spherical models. Particles of high anisotropy may pack in

configurations whereupon the ratio of the particle size to the resultant interstices upon alignment may be significantly smaller, as seen in Figure V.37. Reed specifically contends that angular particles or particles exhibiting anisotropy of this nature will randomly occupy 50-60% of the volume⁷⁹.

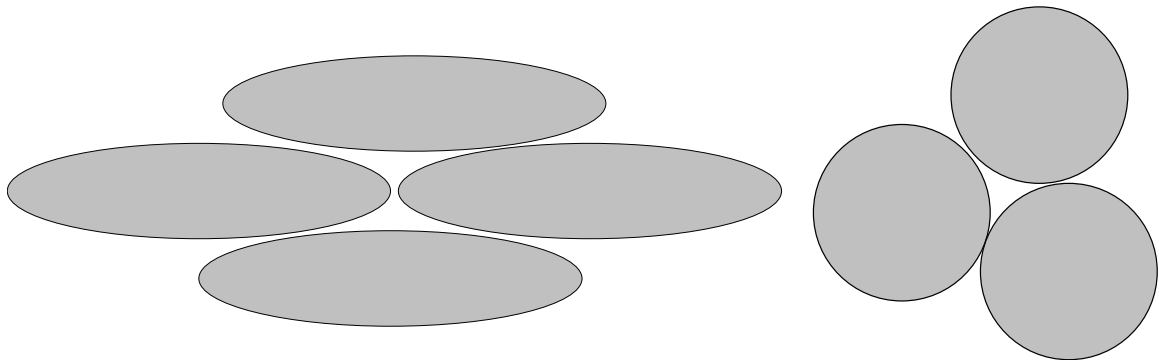


Figure V.37 2-dimensional comparison of the interstices produces between particles of high aspect ratio (left) and smooth spheres.

VI. Conclusions

VI.1 Particle Characterization

It was established that sulfate-processed titania powders of high specific surface area possesses a high soluble sulfate level. This residual sulfate level does not appear to affect the physical size of the aggregates at any iteration as reflected by the results of scanning electron microscopy until a critical level of sulfate has been removed from the system. The greater sulfate level seen at powders of higher specific surface area suggests that the origin of the sulfate is in surface sites speculated to originate from residual titanyl sulfate during synthesis. Little variation is seen among the powders particle size distribution as seen by unanimous log-normal distributions as well as relatively small variations in the median particle diameter. It also appears that the primary particle sizes do not vary.

The variations in ESD calculated to estimate the primary particle size are relatively minor and mainly serve to be reflective of the order of magnitude for the primary particle size, which is commonly on the order of tens of nanometers. The variation in AAN in combination with the relative similarity in particle size serves as a qualitative indication of the fractal nature of the primary aggregate surface for the higher surface area powders. Multiple aggregation iterations are also observed commonly for each of the six powders. This allows one to conclude that contributions to differences in rheology, such as extrudability, will be based on parameters beyond merely physical characteristics of the starting powder.

VI.2 Strength of Aggregation Stages

Boundary conditions were established for strengths of what appear to be three different aggregate iterations. Tertiary and higher order aggregation stages appear to be randomly assembled and incidental in formation and subsequently appear to be broken apart at handling shear stresses below 1 Pa. Secondary aggregation stages appear to be eliminated via techniques such as oscillatory stress-rheometry for measured oscillatory shear stresses between 3 and 25 Pa. The sulfate level among powders does appear to influence the viscoelastic yield stress required to facilitate fluid flow in stress sweeps along with the linear elastic storage modulus. This indicates that the degree of elasticity and the extrudability of the starting powder are highly influenced by starting powder characteristics.

The sulfate, established to be soluble sulfate via spectrophotometry, appears to serve as an indifferent electrolyte in the viscoelastic suspension. The presence of a greater amount of indifferent electrolyte results in a smaller electrical double layer thickness subsequently reducing the degree of double layer overlap with other powder particles and reducing the degree of networking in the suspension. This implies that for extrusion of NO_x catalysts based on titanias of lower sulfate content, a greater amount of additive would be required to compensate for an anticipated higher bulk yield and/or steady-state extrusion pressure.

Compaction curves appear to indicate that the strength of primary scale aggregates range from 484 MPa to 511 MPa suggesting these as (albeit impractical) boundary extrusion conditions to preserve primary scale aggregates as support carriers for an active SCR catalyst.

VI.3 Impact on Bulk Porosity of Varying Shear Conditions

Bulk forming via tape casting appeared to preserve primary scale aggregates as seen qualitatively via scanning electron micrographs. This appears to be corroborated by mercury porosimetry indicating the presence of submicron peaks ranging from 200-500 nm which suggest interstices formed from approximately 1 μm units via particle packing models for spherical particles. Mercury porosimetry of the compacted pellets appeared to corroborate the rupture of primary scale aggregates based on the absence of the aforementioned submicron peak. Additionally, the nanosized peaks additionally exhibited in tape casting appear to have shifted to smaller sizes for compacted samples which indicate rearrangement of primary particles upon rupture of the primary scale aggregate.

VII. Suggestions for Future Work

In the preparation of a high performance NO_x catalyst, it is highly necessary to optimize the flowability of a material by understanding the local effects occurring in the breakdown and subsequent reformation of the hydraulic unit. A possible continuation of the study can be focused on the time dependent recovery of a system as a function of applied shear stress.

The nature of this time dependent recovery is essential in understanding the kinetics of the formation of aggregate structures, especially when considering that the reformation of a ruptured unit may be non-trivial with regards to its as-synthesized structure. An understanding of the nature of these structures, particularly in recovery from shear breakdown, can allow for optimization of a stable aggregated carrier of a catalyst. This will facilitate production into a bulk shape in order to obtain the best use of its fundamental physical properties required to facilitate diffusion, specifically the porosity of the as-formed bulk shape.

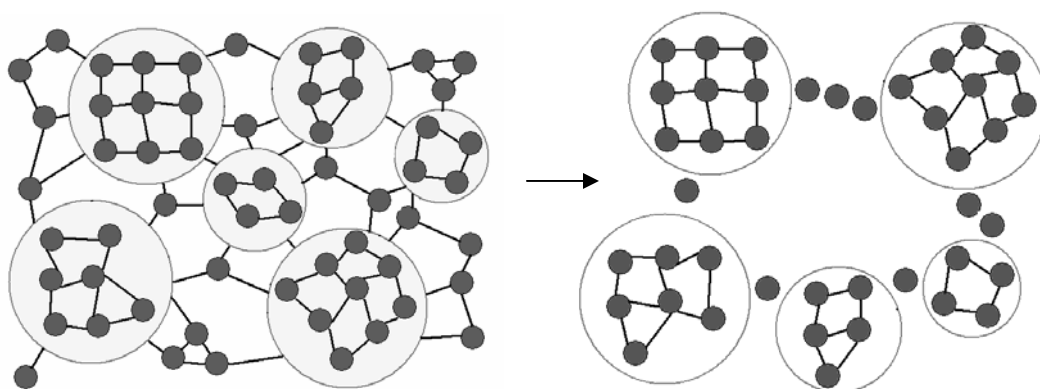


Figure VII.1 Quick network recovery resulting in open assemblages

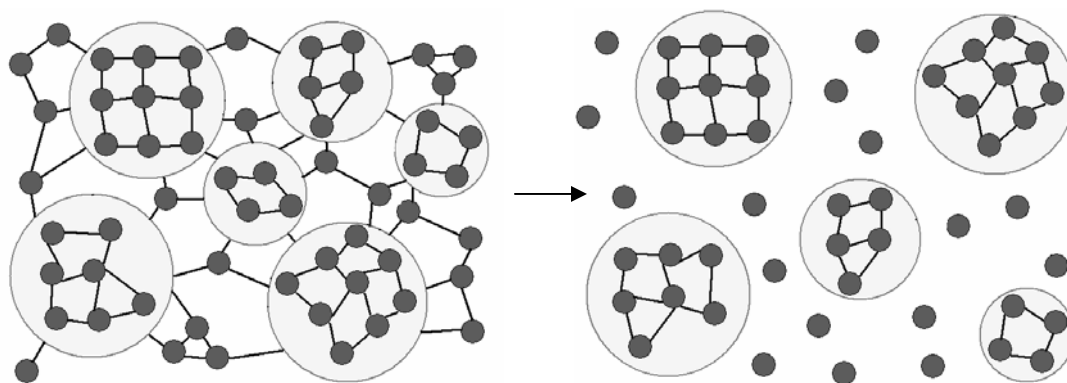


Figure VII.2 Slower network recovery resulting in more ordered assemblages

An additional possibility for pursuit in this investigation is aggregates comprised of primary particles of high aspect ratio to investigate the relationship between the primary particle size and the resultant interstices upon realignment. This particular investigation was fortunate to benefit from the three aggregation iterations exhibiting an ill-defined particle shape in all three dimensions. This subsequently mitigated considerations of preferential alignment upon aggregate breakdown. For some other catalysts, such as diesel particulate traps, an acicular ‘needle-like’ structure may be employed to increase the surface to volume ratio. Aggregates of this structure may breakdown and align to create a different ratio of flowing unit size to particle interstice size.

Further investigations may also consider the effect of altering pore structure via primary aggregate breakdown on the catalytic properties such as diffusion. When considering diffusion on an atomic level it is defined as the motion of atoms into adjacent sites in a lattice, be it interstitial relative to the structure or to a vacancy. Diffusion typically is an activated process with the atoms having to overcome an energy barrier to facilitate this motion. This expression for self-diffusivity is typically given by:

$$D = D_0 \exp\left(-\frac{E}{k_B T}\right) \quad \text{VII.1}$$

Here, ' D ' is the self-diffusivity of an atom or ion or a measure of the ease and frequency with which that atom or ion jumps around in a crystal lattice in the absence of external forces. ' D_0 ' is a pre-exponential term, ' k_B ' is Boltzmann's constant, ' T ' is the temperature of the system and ' E ' is the activation energy for diffusion⁹³.

The rate of motion of atoms of a chemical species, A , can be expressed as Fick's first law:

$$J_A = -D_A \frac{dC_A}{dz} \quad \text{VII.2}$$

Here, ' J_A ' is the flux of species ' A ', (i.e. the number of moles of species A diffusing per unit area per unit time), ' C_A ' is the concentration of species A , ' D_A ' is the diffusion coefficient of A and ' z ' is the diffusion length⁹³

Typically when scaled beyond the atomic level to matter transport, the flow of gaseous species through a pore can be considered in terms of a diffusion process. For such procedures, the term D_A for gases can vary with the gas temperature, T , as $T^{1.5}$ and with the gas pressure, p , as p^{-1} . Froment⁹⁴ argues that this is because of intermolecular collisions during flow through a pore. However, when the pore dimension is smaller than the mean free path of the diffusing species the diffusion mechanism shifts to the collision of molecular species with the pore wall. This so-called Knudsen diffusivity requires a separate diffusion coefficient dependence, D_{KA} , given by:

$$D_{KA} = \frac{4}{3} r \left(\frac{2}{\pi} \frac{RT}{M_A} \right)^{1/2} \quad \text{VII.3}$$

Here, ' r ' is the pore radius, and ' M_A ' is the molecular weight of species A . It should be noted that a distinction be made between the size of the individual units of the diffusing species and the mean free path of the species through the pore. The gaseous units are still in fact small with respect to the diameter of the pore⁹⁴.

In catalyst honeycombs however, the diffusion of gaseous species through pores is complicated by the nature of the pores in a solid material. Subsequently, the flux of species A can be rewritten in Equation II.2 can be rewritten as:

$$J_A = -D_e \frac{dC_A}{dz} \quad \text{VII.4}$$

Here ' D_e ' is the effective diffusivity of species A . The effective diffusivity incorporates parameters of the material through which the gaseous species diffuses. This diffusivity is related to the D_A term found in Equation II.2 by:

$$D_e = \frac{\varepsilon_s}{\tau} D_A \quad \text{VII.5}$$

Here ' ε_s ' is the internal void fraction of the solid and ' τ ' is the pore tortuosity. Substituting back into the Equation II.4 yields:

$$J_A = -\varepsilon_s D_A \frac{dC_A}{\tau dz} \quad \text{VII.6}$$

Further complications with diffusion arise when from the occurrence of chemical reactions at the pore walls with surface species. The diffusion equation is subsequently rewritten by Froment for a slab of thickness, L , as:

$$D_e \frac{d^2 C_s}{dz^2} - k_v \rho_s C_s = 0 \quad \text{VII.7}$$

Here, ' C_s ' is the concentration of surface active component A , ' k_v ' is the reaction rate coefficient based on pellet volume, ' ρ_s ' is the density of the catalyst while ' z ' is the

diffusion length. The second order differential equation can be solved to yield the concentration of reactants at a coordinate, x , relative to the surface concentration of component A , ' C_s^s ' by:

$$\frac{C_s(z)}{C_s^s} = \frac{\cosh\left(x\sqrt{\frac{k_v}{D_e}}\right)}{\cosh(\phi)} \quad \text{VII.8}$$

Here, ' ϕ ' is the Thiele modulus and is given by:

$$\phi = L\sqrt{\frac{k_v}{D_e}} \quad \text{VII.9}$$

However, in considering heterogeneous catalyst materials, diffusion and the chemical reaction begin to compete whereupon a separate reaction rate can be identified incorporating the diffusion resistance that is distinguishable from the true reaction rate, ' r_{true} '. This new observed reaction rate, ' r_{obs} ', is given by:

$$r_{obs} = \eta \cdot r_{true} \quad \text{VII.10}$$

Here ' η ' is the effectiveness factor and defined as the ratio of the reaction rate with pore diffusion resistance to the reaction rate with surface conditions and is given by:

$$\eta = \frac{\tanh \phi}{\phi} \quad \text{VII.11}$$

However, as the value of ϕ becomes larger:

$$\eta \approx \frac{1}{\phi} \quad \text{VII.12}$$

For an n^{th} order irreversible reaction, the ϕ term can subsequently be rewritten as:

$$\phi = \frac{V_p}{S_x} \sqrt{\frac{n+1}{2} \frac{k_v (C_s^s)^{n-1}}{D_e}} \quad \text{VII.13}$$

Where $n > -1$ and:

$$L \equiv \frac{V_p}{S_x} \quad \text{VII.14}$$

Here, ' V_p ' is the volume of the pellet and ' S_x ' is the external surface area of the pellet. The observed reaction rate from Equation II.10 can now be rewritten as:

$$r_{obs} = \frac{r_{true}}{\frac{V_p}{S_x} \sqrt{\frac{n+1}{2} \frac{k_v (C_s^s)^{n-1}}{D_e}}} \quad \text{VII.15}$$

This establishes that in reactor kinetics for catalytic processes such as NO_x catalysis, both diffusion and chemical reaction kinetics play a significant role and warrant consideration. The rate constants for the observed and true reaction, ' $k_{v,obs}$ ' and ' k_v ' respectively, are similarly given by:

$$k_{v,obs} = \eta \cdot k_v \quad \text{VII.16}$$

Now substituting in the associated activation energies along with Equation II.13 yields:

$$k_{v,obs} = \frac{S_x}{V_p} \sqrt{\frac{2}{n+1} \left[A_D \exp\left(-\frac{E_D}{RT}\right) \right] \left[A_A \exp\left(-\frac{E_A}{RT}\right) \right]} \quad \text{VII.17}$$

Here, ' E_D ' and ' E_A ' are the activation energies for diffusion and for the true reaction respectively while ' A_D ' and ' A_A ' are their respective pre-exponential terms. The observed activation energy for the reaction, ' E_{obs} ', is subsequently given by:

$$E_{obs} = \frac{E_A + E_D}{2} \quad \text{VII.18}$$

For cases where $E_A \gg E_D$:

$$E_{obs} \approx \frac{E_A}{2} \quad \text{VII.19}$$

The argument presented is that for a reaction process as would be observed in a catalyst honeycomb monolith the porosity influences the observed reaction kinetics because of the participation of diffusion in the observed reaction. Alteration of the inherent pore structure would seem to affect the observed reaction kinetics because of altering the diffusion component⁹⁴.

VIII. References

1. "NO_x: How Nitrogen Oxides Affect the Way We Live and Breathe" EPA-456/F-98-005 September 1998
2. US DOE Topical Report No. 9 July 1997, "Control of Nitrogen Oxide Emissions"
3. Y. Ozawa, K. Urashima, "Recent Development Trends in Catalyst Technologies for Reducing Nitrogen Oxide Emissions," *Science and Technology Trends* Quarterly Review No. 19 (April 2006)
4. R.M. Heck "Catalytic abatement of nitrogen oxides-stationary applications" *Catalysis Today* **53** (1999) 519-523
5. D. Olszewska "Ammonia and water sorption properties of the mineral layered nanomaterials used as the catalysts for NO_x removal from exhaust gases" *Catalysis Today* **114** (2006) 326-332
6. S.N. Orlik, "Contemporary Problems in the Selective Catalytic Reduction of Nitrogen Oxides (NO_x)" *Theoretical and Experimental Chemistry*, **37**, No. 3, (2001)
7. T. Gryzbek, "Layered clays as SCR de-NO_x catalysts" *Catalysis Today* **119** (2007) pp.125-132
8. P. Forzatti, D. Ballardini and L. Sighicelli, "Preparation and characterization of extruded monolithic ceramic catalysts" *Catalysis Today*, **41** [1-3], 28 May 1998, pp. 87-94
9. M.V. Twigg, "Roles of catalytic oxidation in control of vehicle exhaust emissions," *Catalysis Today* **117** pp. 407-418 (2006)
10. F. Laurent, C.J. Pope, H. Mahzoul, L. Delfosse, P. Gilot, "Modeling of NO_x adsorption over NO_x adsorbers," *Chemical Engineering Sci.* **58** pp. 1793-1803 (2003)
11. M.A. Schwartz, "Pigments: Titania, Iron Oxides and Other Minerals" *Concise Encyclopedia of Mineral Resources*, p. 263 edited by D.D. Carr and N. Herz (Pergamon Press Inc., Elmsford NY, 1989)
12. "Titanium Compounds, Organic," *Kirk-Othmer Encyclopedia of Chemical Technology*, (John Wiley and Sons Inc., New York, NY, 2001)
13. T.E. Garner Jr., "Titanium Resources" *Concise Encyclopedia of Mineral Resources*, pp. 366-368 edited by D.D. Carr and N. Herz (Pergamon Press Inc., Elmsford NY, 1989)
14. A. Fahmi, C. Minot, B. Silvi, M. Causá, "Theoretical analysis of the structures of titanium dioxide crystals," *Phys. Rev. B* **47**, 11717 - 11724 (1993)
15. A. A. Bolzan, C. Fong, B. J. Kennedy and C. J. Howard, "Structural Studies of Rutile-Type Metal Dioxides," *Acta Cryst. B* **53**, pp. 373-380 (1997)
16. Reed, J.S., *Principles of Ceramic Processing*, 2nd ed. (John Wiley & Sons Inc., New York, NY, 1995) p. 44
17. J. Anderson, "Papermaking" *Industrial Minerals and Their Uses: A handbook and formulary*, edited by Ciullo, P.A. (Noyes Publications, Westwood NJ 1996)
18. G.F. Kriechbaum, P. Kleinschmit, "Superfine Oxide Powders – Flame Hydrolysis and Hydrothermal Synthesis," *Angew. Chem. Int. Ed Engl. Adv. Mater.* **28** [10] (1989) pp. 1416-1423

19. S. Vemury, S.E. Pratsinis, "Dopants in Flame Synthesis of Titania," *J. Am. Ceram. Soc.* **78** [11] pp. 2984-92 (1995)
20. S-J Kim, E.G. Lee, S.D. Park, C.J. Jeon, Y.H. Cho, C.K. Rhee, W.W. Kim, "Photocatalytic Effects of Rutile Phase TiO₂ Ultrafine Powder with High Specific Surface Area Obtained by a Homogeneous Precipitation Process at Low Temperatures," *Journal of Sol-Gel Science and Technology* **22** pp. 63-74 (2001)
21. A. Mills, R. H. Davies, and D. Worsley, "Water Purification by Semiconductor Photocatalysis," *Chem. Soc. Rev.*, 1993, **22**, pp. 417 - 425
22. Nanomaterials: Synthesis, Properties and Applications, Edited by A.S. Edelstein and R.C. Cammarata, (Institute of Physics Publishers, Philadelphia PA, 1998)
23. V. A. Hackley, "Guide to the Nomenclature of Particle Dispersion Technology", *NIST Special Publication 945*
24. Shanefield, D.J., Organic Additives and Ceramic Processing: Second Edition, (Kluwer Academic Publishers, Boston MA, 1996)
25. R. David, F. Espitalier, A. Cameirao, L. Rouleau, "Developments in the understanding and modelling of agglomeration of suspended crystals in crystallization from solutions," *KONA Powder and Particle*, **21**, 40-53 (2003)
26. R. G. Horn, "Surface Forces and Their Action in Ceramic Materials", *J. Am. Ceram. Soc.*, **73** [5] 1117-1135 (1990)
27. Hunter, R.J., Introduction to Modern Colloid Science, (Oxford University Press, 1993)
28. B.W. Ninham, "On Progress in Forces Since DLVO Theory," *Advances in Colloid and Interface Sci.* **83** pp. 1-17 (1999)
29. N. Kallay, S. Zalac, "Stability of Nanodispersions: A model for Kinetics of Aggregation of Nanoparticles", *J. of Coll. and Interface Sci.* **253** 70-76 (2002)
30. T. G. M. Van de Ven and R. J. Hunter, "The Energy Dissipation in Sheared Coagulated Sols", *Rheol. Acta*, **16**, 534-43 (1977)
31. Mandelbrot, B., The Fractal Geometry of Nature (W.H. Freeman and Company, New York, NY, 1983)
32. C.M. Sorensen, G. C. Roberts, "The Prefactor of Fractal Aggregates", *Journal of Colloid and Interface Science*, **186**, 447-452 (1997)
33. D. H. de Boer, M. Stone, L.M.J. Levesque, "Fractal dimensions of individual flocs and floc population in streams", *Hydrol. Process.* **14**, 653-667 (2000)
34. J.L. LaRosa, J. D. Cawley, "Fractal Dimension of Alumina Aggregates Grown in Two Dimensions", *J. Am. Ceram. Soc.* **75** [7] (1992)
35. S. Tang, J.M. Preece, C.M. McFarlane, Z. Zhang "Fractal Morphology and Breakage of DLCA and RLCA Aggregates," *J. of Coll. and Interface Sci.* **221** pp. 114-123 (2000)
36. C. Galassi, E. Rastelli, R. Lapasin "Time Dependent Properties of Ceramic Suspensions" Ceramic Transactions Vol. 54, Science Technology and Applications of Colloidal Suspensions, (American Ceramic Society Westerville, OH, 1995) pp. 3-21
37. Macosko C.W., Rheology: Measurements, Principles and Applications (VCH Publishers, New York NY, 1994)
38. Patton, T.C., Paint Flow and Pigment Dispersion (Wiley-Interscience Publishers, New York NY, 1964)

39. Reed, J.S., Principles of Ceramic Processing, 2nd ed. (John Wiley & Sons Inc., New York, NY, 1995) pp. 280-287
40. F.H. Busse, "Visualizing the Dynamics of the Onset of Turbulence," *Science* **305** pp. 1574-1575 (10th Sept. 2004)
41. S.M. Nycz, "Controlling Particle Orientation During Forming" PhD. Dissertation, Rutgers University, Piscataway, NJ, 2006
42. Brodkey R.S., The Phenomena of Fluid Motions, p. 292 (Addison-Wesley Publishing Company, Reading MA, 1967)
43. T. Hemphill, W. Campos, A. Pilehvari, "Yield-power law more accurately predicts mud rheology," *Oil and Gas Journal* **91** No. 34 pp. 45-50
44. R. Pitchumani, V.M. Karbhari, "Generalized Fluid Flow Model for Ceramic Tape Casting," *J. Am. Ceram. Soc.* **78** [9] pp. 2497-2503 (1995)
45. Benbow, J., Bridgwater J., Paste Flow and Extrusion (Clarendon Press, Oxford UK, 1993)
46. A.N. Alexandrou, G. Florides, G. Georgiou, "Compression of Materials with Yield Stresses," 5th GRACM International Congress on Computational Mechanics
47. I.M. Krieger, T.J. Dougherty "A model for Non-Newtonian Flow in Suspensions of Rigid Spheres" *Transactions of the Society of Rheology III*, pp. 137-152 (1959)
48. M. Mooney, "The viscosity of a concentrated suspension of spherical particles," *J. Coll. Sci* **6** pp. 162-170 (1951)
49. J. F. Douglas, E.J. Garboczi, "Intrinsic Viscosity and the Polarizability of Particles Having a Wide Range of Shapes," *Advances in Chemical Physics*, Vol. XCI, pp. 85-153 (1995)
50. T.F. Thadros, *Rheology of Unstable Systems*, Industrial Rheology Lecture Notes (The Center for Professional Advancement, 1994)
51. H. Wu, M. Morbidelli, "A Model Relating Structure of Colloidal Gels to Their Elastic Properties," *Langmuir*, **17**, pp. 1030-1036 (2001)
52. F.F. Lange, "Shape Forming of Ceramic Powders By Manipulating the Interparticle Pair Potential," *Chemical Engineering Science*, 56 pp. 3011-3020 (2001)
53. B. Rand, R. Fries "Viscoelasticity of nano-alumina dispersions," Ceramic Transactions Vol. 54, Science Technology and Commercialization of Powder Synthesis and Shape Forming, (American Ceramic Society Westerville, OH, 1996) pp.165-172
54. Mistler R.E., Twiname E.R., Tape Casting: Theory and Practice, (The American Ceramic Society, Westerville OH, 2000)
55. G.N. Howatt, R.G. Breckenridge, J.M. Brownlow, "Fabrication of Thin Ceramic Sheets for Capacitors," *J. Am. Ceram. Soc.* **30** [8] pp. 237-242 (2006)
56. H. Loest, R. Lipp, E. Mitsoulis, "Numerical Flow Simulation of Viscoplastic Slurries and Design Criteria for a Tape Casting Unit," *J. Am. Ceram. Soc.* **77** [1] pp. 254-262 (1994)
57. H. Watanabe, T. Kimura, T. Yamaguchi "Particle Orientation during Tape Casting in the Fabrication of Grain-Oriented Bismuth Titanate," *J. Am. Ceram. Soc.* **72** [2] pp. 289-293 (1989)

58. M. Schmidt, H. Munstedt, M. Svec, A. Roosen, T. Betz, F. Koppe, "Local Flow Behavior of Ceramic Slurries in Tape Casting, as Investigated by Laser-Doppler Velocimetry," *J. Am. Ceram. Soc.* **85** [2] pp. 314-320 (2002)
59. P.M. Raj, W.R. Cannon, "Anisotropic Shrinkage in Tape Cast Alumina: Role of Processing Parameters and Particle Shape," *J. Am. Ceram. Soc.* **82** [10] pp. 2619-25 (1999)
60. J. Patwardhan, W.R. Cannon, "Factors Influencing Anisotropic Sintering Shrinkage in Tape Cast Alumina: Effect of Processing Variables," *J. Am. Ceram. Soc.* **89** [10] pp. 3019-3026 (2006)
61. H.J. Kim, M.J.M. Krane, K.P. Trumble, K.J. Bowman, "Analytical Fluid Flow Models for Tape Casting" *J. Am. Ceram. Soc.* **89** [9] pp. 2769-2775 (2006)
62. Y.T. Chou, Y.T. Ko, M.F. Yan, "Fluid Flow Model for Ceramic Tape Casting," *J. Am. Ceram. Soc.* **70** [10] pp. C280-C282 (1987)
63. McEntire, B.J., "Dry Pressing," Engineering Materials Handbook Vol. 4: Ceramics and Glasses, (ASM, 1991)
64. Reed, J.S., Principles of Ceramic Processing, 2nd ed. (John Wiley & Sons Inc., New York, NY, 1995) pp. 418-429
65. S.J. Lukasiewicz, "Spray-Drying Ceramic Powders," *J. Am. Ceram. Soc.* **72** [4] pp. 617-24 (1989)
66. S. Balasubramanian, D.J. Shanefield, D.E Niesz, "Effect of Internal Lubricants on Defects in Compacts Made from Spray-Dried Powders," *J. Am. Ceram. Soc.* **85** [1] pp. 134-38 (2002)
67. S. Balasubramanian, D.J. Shanefield, D.E Niesz, "Effect of Externally Applied Plasticizer on Compaction Behavior of Spray-Dried Powders," *J. Am. Ceram. Soc.* **85** [1] pp. 134-38 (2002)
68. R.A. DiMilia, J.S. Reed, "Stress Transmission During the Compaction of a Spray-Dried Alumina Powder in a Steel Die," *J. Am. Ceram. Soc.* **66** [9] pp. 667-672 (1983)
69. S.J. Glass, K.G. Ewsuk and F.M. Mahoney, "Ceramic Powder Compaction"; pp. 3-18 in Ceramic Transactions, Vol. 70, *Ceramic Manufacturing Practices and Technology*. Edited by T.K. Gupta, B. Hiremath and K.M. Nair. American Ceramic Society, Westerville, Ohio, 1996
70. Kennard, F., "Cold Isostatic Pressing," Engineering Materials Handbook Vol. 4: Ceramics and Glasses, (ASM, 1991)
71. Larker, H. T., "Hot Isostatic Pressing," Engineering Materials Handbook Vol. 4: Ceramics and Glasses, (ASM, 1991)
72. R.G. Frey, J.W. Halloran, "Compaction Behavior of Spray-Dried Alumina," *J. Am. Ceram. Soc.* **67** [3] pp. 199-203 (1984)
73. C.M. Kong, J. L. Lannutti, "Localized Densification during the Compaction of Alumina Granules: The Stage I-II Transition," *J. Am. Ceram. Soc.* **83** [4] pp. 685-90 (2000)
74. R.L.K. Matsumoto, "Generation of Powder Compaction Response Diagrams," *J. Am. Ceram. Soc.* **69** [10] pp. C246-247 (1986)
75. D.E. Niesz, R.B. Bennett and M.J. Snyder, "Strength Characterization of Powder Aggregates," *Am. Ceram. Soc. Bull.*, **51** [9], 1972 p.677

76. R.L.K. Matsumoto, "Analysis of Powder Compaction Using a Compaction Rate Diagram," *J. Am. Ceram. Soc.* **73** [2] pp. 465-468 (1990)
77. P.R. Mort, R.Sabia, D.E. Niesz, R.E. Riman "Automated generation and analysis of powder compaction diagrams" *Powder Technology* **79** 111-119 (1994)
78. L.E. Reynolds, "Effect of Molecular Weight on Sodium Salts of Fatty Acids as Lubricants" M.S. Thesis, Rutgers University, Piscataway, NJ, 2005
79. Reed, J.S., Principles of Ceramic Processing, 2nd ed. (John Wiley & Sons Inc., New York, NY, 1995) p. 218-227
80. A.E.R. Westman and H.R. Hugill, "The Packing of Particles," *J. Am Ceram. Soc.*, **13** pp.767-779 (1930)
81. H.E. White, S.F. Walton, "Particle Packing and Particle Shape," *J. Am Ceram. Soc.*, **20** pp. 155-166 (1937)
82. R.K. McGearry, "Mechanical Packing of Spherical Particles," *J. Am. Ceram. Soc.*, **44** pp. 513-522 (1961)
83. A. Donev, I. Cisse, D. Sachs, E. A. Variano, F. H. Stillinger, R. Connelly, S. Torquato, P. M. Chaikin, "Improving the Density of Jammed Disordered Packings Using Ellipsoids," *Science*, **303** (13 February 2004)
84. J. Zheng, P.F. Johnson and J.S. Reed, "Improved Equation of the Continuous Particle Size Distribution for Dense Packing," *J. Am. Ceram. Soc.*, **73** [5] pp. 1392-1398 (1990)
85. K. Karlsson, L. Spring, "Packing of Irregular Particles," *Journal of Materials Science*, **5** pp. 340-344 (1970)
86. M. Kobayashi & M. Hagi, " V_2O_5 - WO_3 /TiO₂-SiO₂-SO₄²⁻ catalysts: Influence of active components and supports on activities in the selective catalytic reduction of NO by NH₃ and in the oxidation of SO₂," *Applied Catalysis B*, vol. 64, p. 104, (2006)
87. S.M. Augustine, J. Schultz, R. McIntyre, "The morphology component in DeNO_x catalyst activity," *Catalysis Today* **112** 180-183 (2006)
88. *Personal Communication*, D.E. Niesz 2007
89. D.C-H. Cheng, "Yield Stress: A time-dependent property and how to measure it," *Rheol. Acta* **25** (1986) pp. 542-554
90. R. Mas, A. Magnin, "Experimental Validation of Steady Shear and Dynamic Viscosity Relation for Yield Stress Fluids," *Rheol Acta* **36** (1997) pp. 49-55
91. J. de Vicente, J.D.G. Duran *, A.V. Delgado, "Electrokinetic and viscoelastic properties of magnetorheological suspensions of cobalt ferrite," *Colloids and Surfaces A: Physicochemical and Engineering Aspects* **195** (2001) pp. 181-188
92. Lowell, S., Shields, J.E., Powder Surface Area and Porosity 2nd Ed., (Chapman and Hall Ltd., London, 1984)
93. Barsoum, M.W., Fundamentals of Ceramics, (McGraw-Hill Inc., New York, NY 1997)
94. Froment, G.F. & Bischoff, K.B., Chemical Reactor Analysis and Design, (John Wiley & Sons, New York, NY, 1979), pp. 178-185

IX. Curriculum Vita

Navin Venugopal

- 1979 Born August 29 in Lagos Nigeria
- 1997 High School Diploma, Bergenfield High School, Bergenfield, NJ
- 2001 Summer Intern, The Dow Chemical Company, Midland MI
- 2002 Bachelor of Science, Ceramic Engineering, Rutgers University, New Brunswick NJ
- 2002 M.J. Matthewson, C.R. Kurkjian, C.D. Haines, N. Venugopal
 “Temperature dependence of strength and fatigue of fused silica fiber in the range of 77 to 473 K” Proceedings of the SPIE Vol. 4940 (2003)
- 2002-2007 Research Assistant, Department of Ceramic and Materials Engineering, Rutgers University, New Brunswick, NJ
- 2005 N. Venugopal, R.A. Haber, S.M. Augustine and R.D. Skala, "High shear casting of nanoparticulate TiO₂", Ceramic Transactions Volume 172 - Ceramic Nanomaterials and Nanotechnologies IV, Edited by Richard M. Laine, Michael Hu and Songwei Lu; pp, 95-106
- 2006 N. Venugopal, R.A. Haber, “Yield Strength of Nanoparticulate Titania Via Compaction” (In press)
- 2007 D. Maiorano, N. Venugopal, R.A. Haber, “Effect of Soluble Sulfate removal on the Rheological behavior of nanoparticulate TiO₂” (In press)
- 2007 N. Venugopal, R.A. Haber, D. Maiorano, “Effects of Starting Powder Characteristics on Bulk Assembly of Titania” (In press)
- 2007 N. Venugopal, R.A. Haber, “Structure of aggregated nanoscale TiO₂ at varying viscoelastic stages” (In press)
- 2008 Doctor of Philosophy, Ceramic and Materials Engineering, Rutgers University, New Brunswick, NJ
- 2007 Senior Engineer, The Dow Chemical Company, Midland MI